Forschungszentrum Jülich
in der Helmholtz-Gemeinschaft

Institute of Bio- and Nanosystems (IBN)
Bioelectronics (IBN-2)

Characterization of the Cell-Sensor Contact with Total Internal Reflection Fluorescence Microscopy

Sascha Engelhardt

Jül-4255

Characterization of the Cell-Sensor Contact with Total Internal Reflection Fluorescence Microscopy

Sascha Engelhardt

Berichte des Forschungszentrums Jülich ; 4255
ISSN 0944-2952
Institute of Bio- and Nanosystems (IBN)
Bioelectronics (IBN-2) Jül-4255

The complete volume is freely available on the Internet on the Jülicher Open Access Server (JUWEL) at http://www.fz-juelich.de/zb/juwel

Zu beziehen durch: Forschungszentrum Jülich GmbH · Zentralbibliothek, Verlag
D-52425 Jülich · Bundesrepublik Deutschland
☎ 02461/61-5220 · Telefax: 02461/61-6103 · e-mail: zb-publikation@fz-juelich.de

Contents

1 Introduction

Electrically active cells are specialized cells, responsible for a vast variety of functions. Among others, information processing in the central nervous system, motor functions of organs and muscles, and sensory input recognition in highly complex organs like the eye or the ear are based on evolutionary optimized networks of electrically active cells. A deeper understanding of their basic properties may lead to a better insight into memory formation in the brain or diseases of the nervous system like Parkinson's disease.

One possible method to analyze electric properties of cells is the Patch-Clamp Technique [Hamill et al., 1981; Neher and Sakmann, 1976]. A patch-pipette with a diameter of several micrometers is used to open the cell membrane at a specific point to form an electric connection to the cell. Although huge progress in understanding of electrically cells was achieved with this method, it comes with two main limitations. Since every cell has to be contacted by a separate patch pipette, the number of cells that can be analyzed simultaneously is limited by spatial restrictions. Furthermore, the patch pipette inflicts irreversible damage to the cell membrane, which leads to an exchange of intra- and extracellular liquids, as well as to the death of the cell after typically a few hours. These limitations make it difficult to analyze huge neuronal networks, or to do longterm measurements, both of which are important for the understanding of central brain functions like memory formation.

As an alternative to the Patch-Clamp Technique, electrical sensing devices, such as Multi-Electrode-Arrays [Gross et al., 1985; Jimbo et al., 1993; Pancrazio et al., 1998; Pine, 1980; Stett et al., 2000; Thomas et al., 1972] or Field Effect Transistors [Bergveld et al., 1976; Fromherz et al., 1991] were introduced. These devices use the change in

potential generated by the cell in the extracellular electrolyte to detect electrical activity of cells. The sensitivity of those sensing devices strongly depends on the distance between cell and device. Cells do not adhere homogeneously on interfaces. Depending on the cell type, a cell can show very small distances (focal contacts, focal adhesion, fibrillar adhesion) and at the same time areas of upwards bulging of the cell membrane. Proteins that connect the cell to the substrate have a certain length, thus creating a distance offset. One possibility to determine the cell-substratum distance is by using frequency spectroscopy of the electrical sensing device itself. Using this method, Weis et al. [1996] gained a mean distance for a neuron grown on a poly-L-lysine coated interface of 22 nm. Although distance determination is possible, only the mean value over the whole cell body can be measured without any characterization of the morphology of the adhesive region of the cell. Another possibility is the use of electron microscopical methods. In our group, Höller [2005] used transmission electron microscopy (TEM) on cuts through HEK293 cells to analyze differences in protein coatings on human embryonic kidney cells. Although this method has a high lateral resolution (approx. 2 nm), the measurements could only be done on fixated cells. Information about absolute distances was lost, and the existence of preparation artifacts could not be ruled out.
Optical microscopy can be used to measure distances on living cells with high lateral resolution (typically 200-400 nm). Three main approaches exist: Fluorescence-Interference-Contrast Microscopy (FLIC), Reflection-Interference-Contrast Microscopy (RICM), and Total-Internal-Reflection-Fluorescence Microscopy (TIRF). FLIC microscopy uses the distance dependency of standing waves intensities on silicon. A structured optical transparent silicon dioxide surface is used to derive the distances based on an optical model [Lambacher and Fromherz, 1996]. Although this method was used to characterize different cell types cultured on a broad range of proteins, the three dimensional structure of the substrate should have an influence on the adhesive properties in comparison to flat surfaces [Andersson et al., 2003]. Normal flat glass coverslips can be used for RICM [Radler and Sackmann, 1993]. This approach uses interference effects from light reflected by the glass and the cell membrane. Here, assumptions need to be made about the refractive indices of the cell membrane, the cytoplasma, and the cleft

between glass and cell.

TIRF microscopy [Axelrod, 1981] utilizes the fast decaying electromagnetic field (evanescent wave) originating from total internal reflection. The imaged region is defined by the evanescent wave and the excitation of fluorescent molecules is restricted to a few hundred nanometers. By this means, only the adhesive region of the cell is illuminated, drastically reducing background signals. The first approaches to measure cell-substratum separation distances used the information of the exponential decay of the evanescent wave for a single angle of incidence [Truskey et al., 1992] to get relative distance values. In order to get absolute values, a range of incident angles was used in Variable-Angle-TIRF (VA-TIRF). This method was used to measure distances in diverse applications in cell biology such as cell-substratum separation distances [Olveczky et al., 1997] or intracellular vesicle transport [Loerke et al., 2000]. All these measurements were performed on specialized TIRF setups, constructed for the purpose of distance measurements.

The objective of this thesis is to analyze the possibility to use a commercially available TIRF microscope to determine cell-substratum distances and to characterize the adhesive region of a living cell.

This thesis is structured in seven chapters. After this introduction, the second chapter describes the fundamentals of electrophysiological measurements of electrically active cells. The third chapter gives an overview of the basic concepts and limitations of optical microscopy and introduces the theory necessary for the characterization of the cell/substratum contact area with TIRF microscopy. The fourth and fifth chapters describe the experimental setup and methods used in this thesis. The results and their discussion are shown in chapter six. And finally, a conclusion and an outlook for future setup enhancement and experiments is presented in chapter seven.

2 Fundamentals

2.1 The Field-Effect-Transistor

The field-effect-transistor (FET) is a three terminal device. A potential applied to the gate contact controls the current flow between source and drain as shown in figure 2.1a. Depending on the drain source voltage, the transistor acts either as a resistor (linear region), or as a voltage-controlled current source (saturated region). The most prominent FET is the metal oxide semiconductor FET (MOSFET) and will be introduced briefly in this section. An important semiconductor for transistors is silicon. Silicon is a semiconductor of the IV. main group. Therefore, it has 4 electrons on the outer electron shell (valence electrons). If an element of the V. main group (e.g. arsenic) is introduced into the silicon crystal, the extra valence electron can be approximated as a free negative charge carrier. This process is called n-doping. Very small concentrations (typically 10^{-5} doping atoms per silicon atom) of V. main group elements elevate the charge carrier density and thereby the conductance, drastically. If an element of the III. main group is introduced, the vacancy of an electron constitutes a positive charge carrier. In this case, the process is called p-doping. Here, only a p-type MOSFET is described because n-type MOSFETs behave in a similar way [Ibach and Lüth, 2002]. In a p-type MOSFET, the regions underneath the source and drain contacts are p-doped whereas the channel and bulk material is n-doped. If a voltage is set between source and drain, one of the p-n-junctions is blocked, and the resulting current is very low. A negative voltage applied between gate and source leads to a drop of the voltage across the gate oxide. This voltage drop leads to a bending of the electric band structure. If the applied voltage is high enough, the bending leads to an inversion of the charge

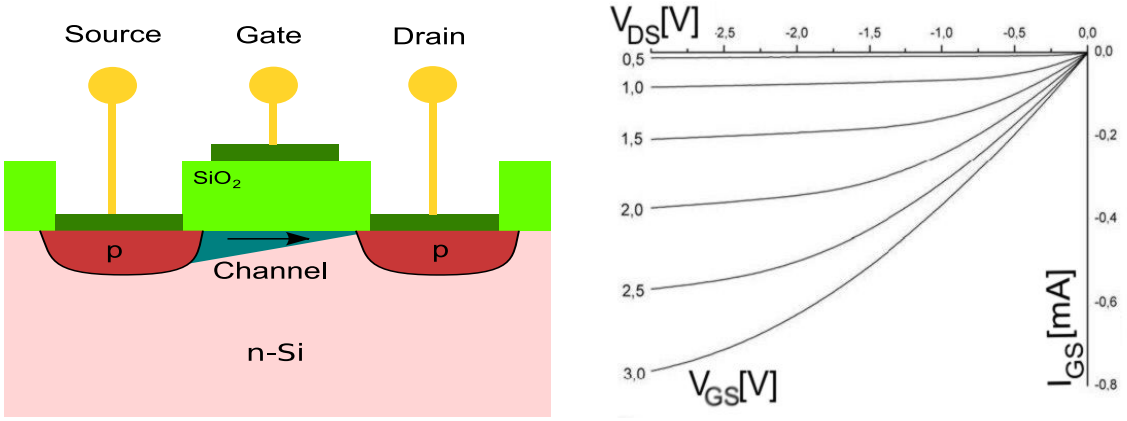

(a) P-FET layout

(b) P-FET characteristic

Figure 2.1: (a) Principle layout of a p-MOSFET. (b) Output characteristic of a p-FET. The current I_{DS} as a function of the voltage V_{DS}. The different curves represent different constant gate voltages V_{GS} (source: Höller [2005]).

carriers in a narrow zone between the n-doped drain and source regions. This inversion area connects the drain and source contact electronically allowing current to flow.

The current I_{DS} between drain and source depends on the drain source voltage V_{DS} (Fig. 2.1b). I_{DS} increases with increasing V_{DS} up to point where saturation is reached. I_{DS} also increases with rising gate voltage V_{GS}. This behavior can now be used to measure an electrical signal emitted by a cell adhered on the gate, which creates a voltage difference ΔV_{GS}. One class of FETs that can be utilized for cell measurements are ion-sensitive field-effect-transistors (ISFET). The source and drain are constructed similarly to a MOSFET, but the gate metal is omitted and an electrolyte solution contacted by a reference electrode is used as gate electrode. The channel is protected by a gate oxide as a barrier layer, which is sensitive to ions. When the ion concentration of the solution changes, the current flow through the transistor will change accordingly. One example of ISFETs is the open-gate-FET [Fromherz et al., 1991; Ingebrandt, 2001; Offenhäusser et al., 1995]. Here, the gate is protected by a thin oxide layer of typically 10 nm SiO_2. The signals can be coupled to the transistor through this dielectric.

2.2 The Electrically Active Cell

2.2.1 The Cell

The cell is the basic unit of life. Generally, all cells can be classified as cells without a nucleus (prokaryotic cells) and cells possessing a nucleus (eucaryotic cells) [1]. All animal cells are eucaryotic cells. The interior of an animal cell consists of a complex system of organelles and molecules enclosed by a cell membrane (Fig 2.2 and 2.3), which serves as protection against environmental influences as well as for controlled exchange of substances between the cell and its surrounding. Around 50% of the cell membrane mass is made of lipid molecules and the remainding 50% consists of proteins and carbohydrates. Most lipid molecules are phospholipids with a polar (hydrophilic) head group and two hydrocarbon (hydrophobic) tails. This structure is called amphiphilic. The amphipatic nature of phospholipids causes them to form structures in water, which minimize the disruption of hydrogen bonding. A lipid bilayer forms spontaneously in aqueous solution, such that the hydrophobic tails are directed towards the center of the membrane and the hydrophilic head groups are directed toward the solution. The lipid bilayer forms the basic structure of the cell membrane. The mosaic structure of the cell membrane is impermeable to ions and big hydrophilic molecules but allows the passage of small or lipophilic molecules. Membrane proteins have sequences of hydrophobic amino acids so that they are inserted into the lipid bilayer by minimizing the hydrogen bonding disruption. The liquid chrystalline structure of the membrane allows the incorporated or attached proteins to diffuse inside the membrane. Transport proteins, enzymes, receptor proteins, cell-cell interaction proteins and cell adhesion proteins for cell-cell or cell-extracellular matrix adhesion are just a few examples for the wide range of different proteins.

[1] A general overview of the cell and cell adhesion can be found in Alberts et al. [2004]

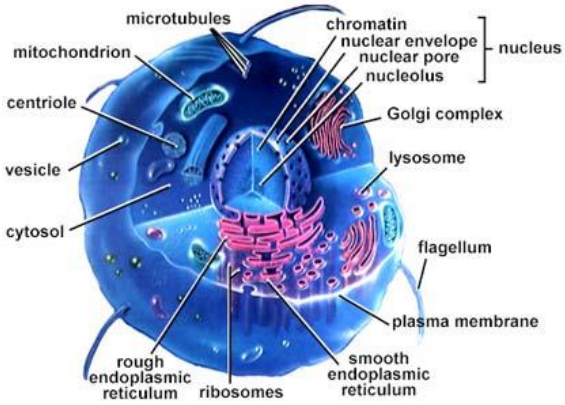

Figure 2.2: An eukaryotic cell is a complex entity with internal membrane enclosed compartments, called organelles, e.g. centrioles, lysosomes, golgi complexes, mitochondria among others. The cell is protected from the environment by the cell membrane (source: [Farabee]).

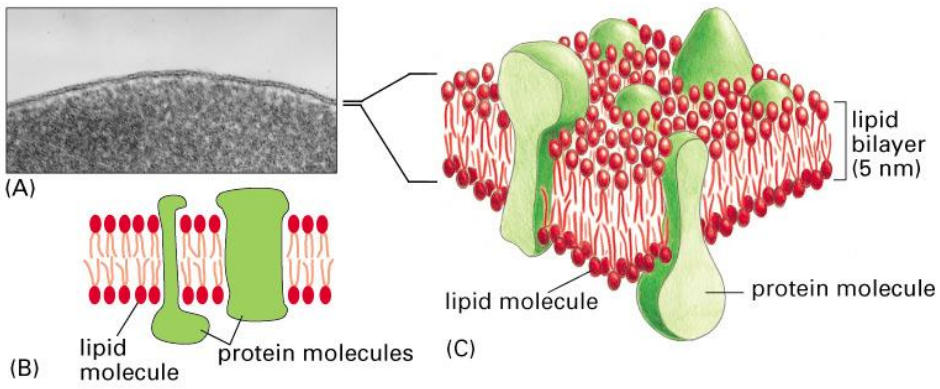

Figure 2.3: Electron microscopical image (A) of the cell membrane. Two- (B) and three-(C) dimensional view on the mosaic structure of the cell membrane (source: [Alberts et al., 2004]).

2.2.2 Electrical Measurements of Electrically Active Cells

The electric activity of cells is mainly governed by the cell membrane and membrane-incorporated transport proteins. Transport proteins can be divided into passive and active transport proteins. Passive transport proteins, e.g. ion channels, facilitate the passage of ions through the membrane in a highly selective way. Active transport proteins need energy to regulate the controlled influx or efflux of specific ions across the membrane. The energy, usually taken from ATP/ADP reactions, is used to move ions against their electrochemical gradient (primary active transport protein). One important function of transport proteins is to generate a concentration gradient for the different ion species between extracellular and intracellular space. The different concentrations generate an interplay of diffusion forces and electrostatic interactions, which finally leads to an equilibrium state where diffusion forces are compensated by an equilibrium potential (the resting potential of the cell). If the membrane is impermeable for ions X, the equilibrium potential V_X can be calculated by the Nernst-Equation:

$$V_X = \frac{RT}{zF} \ln \left(\frac{[X]_{in}}{[X]_{out}} \right) \tag{2.1}$$

where R is the gas constant, T is the temperature, z is the valance of the ions, F is the Faraday constant and $[X]_{in}$, and $[X]_{out}$ are the ion concentrations inside and outside the cell. The most predominant ions involved are sodium, potassium, and chloride ions. The resting potential for these ion can be calculated with given permeabilities P_X by the Goldman equation:

$$V_X = \frac{RT}{F} \ln \left(\frac{P_K[K^+]_{out} + P_{Na}[Na^+]_{out} + P_{Cl}[Cl^-]_{in}}{P_K[K^+]_{in} + P_{Na}[Na^+]_{in} + P_{Cl}[Cl^-]_{out}} \right) \tag{2.2}$$

For electrical active cells like neurons or cardiac myocytes, a disturbance of the resting potential (e.g. an external stimulus) can cause a massive flow of ions through the cell membrane. If the cell is tightly adhered to the surface of a substrate, this

flow leads to an accumulation of ions in the cleft between the cell membrane and the surface. The accumulated ions flow through the cleft between cell and surface to the outer bulk electrolyte. The cleft acts as a resistor with a resistance mainly governed by the cleft height and geometry. The ion current through the cleft causes a voltage drop across the resistance of the electrolyte within the cleft. This voltage drop can be detected by electrical devices, such as FETs, if the cell membrane is directly located above the gate oxide of the FET.

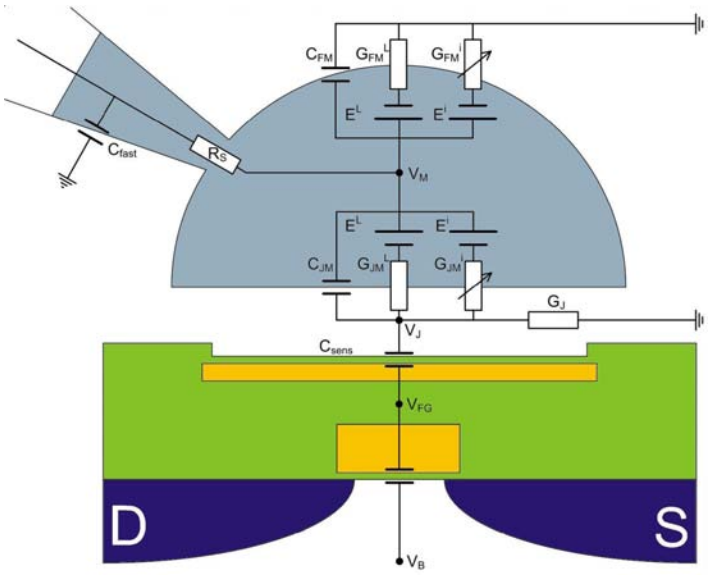

Figure 2.4: Point-contact model of the coupling between a cell and a FET. (source: Meyburg [2005])

The point-contact-model [Regehr et al., 1989] describes the electric coupling between cell and device by means of an equivalent electrical circuit (Fig. 2.4). The electric coupling of a cell with a FET is modeled by a single point represented by the junction voltage V_J. V_J is the voltage drop across the junction resistance R_J, which depends on several factors. The most important factors are the junction's geometry, the distance between cell and device and the electrolyte conductivity. In order to understand the coupling process, it is imperative to acquire detailed knowledge about this junction. The generation of this cell/device junction is governed by the process known as cell adhesion.

2.2.3 Cell Adhesion

Cell adhesion is a complex process where a variety of biological and physical mechanisms lead to a highly specific and versatile cell behavior. Among others, cell adhesion is important for organ and tissue formation in embryos, wound healing, immune system responses, and cancer development. Cell adhesion can occur between cells as well as between cells and the extracellular matrix (ECM). The ECM is a network of macromolecules, consisting mainly of proteins and polysacharides, secreted by the cell into the extracellular space. The ECM forms a supportive structure framework for tissues and provides a means of communication between cells within the tissue.

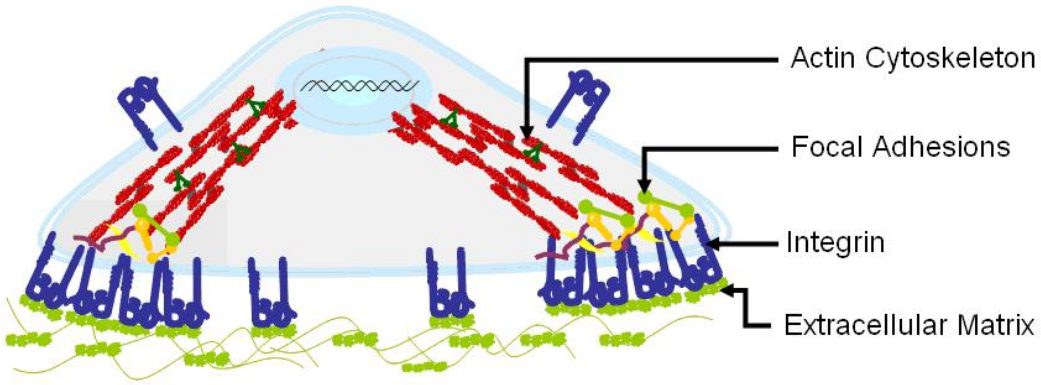

Figure 2.5: Cell adhesion between ECM and cell involves binding of integrin receptor to ECM proteins. The clustering and connection of integrins to the cytoskeleton is called focal adhesion. (source: Michael [2006])

Depending on functionality, cell-cell adhesion forms either tight junctions, gap junctions, or adherens junctions. Tight junctions are built by a dense net of membrane spanning protein strands that mainly serve the purpose of sealing the intercellular space for a flow of ions or other substances. Every protein bundle in a tight junction acts as an independent barrier so the ability to circumvent particle flow grows logarithmically with the number of bundles. Gap junctions are intercellular channels with a diameter of $1.5 - 2$ nm made of transmembrane proteins on each cell and allow free passage of ions and small molecules. Adherens junction are membrane spanning structures, which increase mechanical stability by forming bonds between the cytoskeleton

of the two cells. The cytoskeleton is a dynamic network of proteins inside the cytoplasm of every cell that gives mechanical integrity to the cell and tissue. Three main structures are built by the cytoskeletal proteins. Microtubuli have a hollow cylindrical shape with a diameter of 25 nm, actin filaments a diameter of 7 nm and intermediate filaments a diameter of 10 nm. The mechanical support of the cell is given by the actin- and intermediate filaments.

Cell adhesion between a cell and ECM molecules (ECM ligands), such as laminin, fibronectin and collagen, is a complex process mediated by binding of ECM ligands to transmembrane integrin receptors [Alberts et al., 2004; Zamir, 2001]. Clustering of receptor/ligand complexes leads to a further binding of intracellular adaptor proteins such as vinculin and mechanical strengthening of the connection. These complexes of proteins are termed focal adhesions. Integrins bind with a relatively low affinity to the ligands, allowing association and dissociation of receptor ligand complexes. Signals transmitted from the outside of the cell through focal adhesion complexes (outside-in signaling) also control cell survival, spreading, and proliferation [Hynes, 2002]. Integrin affinity can also be controlled by processes within the cell (inside-out signaling), which indicates the complexity of the adhesive process. The morphological structure of the adhesive area of the cell is controlled by a large amount of factors. From a mechanical point of view, the strongest adhesion is given by an equilibrium concentration of ligands and receptors, governed by the association and dissociation rates and clustering of integrin receptors [Irvine et al., 2002; Lauffenberger and Linderman, 1993]. However, it is not only the complex building integrin receptor that is responsible for adhesion strength and morphology [Sackmann and Bruinsma, 2002; Sackmann and Goennenwein, 2006]. The short range binding forces of the receptor-ligand complexes (approx. 10 nm) compete with medium range repelling forces due to glycocalix proteins (covalently attached oligosacarides to the cell membrane). And, the cell membrane possesses a certain bending elasticity which leads to an equilibrium distribution of repellers and complexes as well.

One way to characterize cell adhesion is by optical microscopy. Cell adhesion molecules and proteins can be labeled with fluorescent markers and then be visualized using flu-

orescent microscopy (Section 3.3). Fluorescence microscopy yields the distribution of adhesion molecules in the cell/substrate contact area and a relative intensity related to the number of molecules. The contrast of fluorescent images of adhesion molecules can be enhanced with TIRF microscopy, as the background fluorescence is reduced. Furthermore, TIRF microscopy offers the possibilty to visualize the adhesive area of a cell without specific labeling of adhesion molecules.

2.3 Cell Types

2.3.1 Neuronal Cells

Neurons fulfill a vast variety of purposes in animals. They have the ability to form connections among each other and communicate via these connections. The connections are formed by synapses between neurites, which are long cellular extentions of the cell. Neurites can be classified in dendrites and axons. The dendrites of a neuron have many branches and are primarly responsible for the electrical, chemical or mechanical input of a neuron. On the other hand, axons consist of only one long branch that carries the information towards other neurons, away from the cell body. Since normal neuronal cells show no cell division, cells are extracted (e.g rat embryo, or cricket) and kept alive in vitro for a certain amount of time.

2.3.2 HEK293

Human embryonic kidney cells (HEK293) are commonly used in biology because they are easy to work with, robust and adhere without the addition of proteins. The cell line of HEK 293 was generated by transformation of cultures of human embryonic kidney cells by the group of Graham in 1977 [Graham et al., 1977]. Cell lines show several advantages to primary cells like rat cortical neurons. They have the ability to cell division and are highly comparable to each other, because they are genetically identical. On advantage of HEK 293 cells is their low number of naturally expressed (endogenic) ion channels. Thus, specific ion channels can be introduced to the cell

line for studies (e.g. bEAG-1 by Frings et al. [1998] or Schönherr et al. [2002]). For this reason HEK293 cells are extensively used in our research group for the electrical characterizations of ion channels and for detailed studies of the electronic cell-sensor contact.

3 Optical Microscopy

A light microscope enables the optical magnification of samples using a system of lenses. For this purpose, the illumination has to be diffused, and the observation has to be in focus. Modern microscopes use a system of conjugated optical planes to fulfill this task. The sharp image of the lamp filament is homogeneous and diffused while illuminating the sample (Köhler illumination). The magnified image forms in two steps. First, the light of the illuminated sample in the specimen plane is collected and magnified by the objective. The objective contains a collecting lens that projects the light to infinity and a tubus lens which magnifies the image. Additionally, the ocular lens magnifies the image. Thus, total magnification is a product of objective and ocular magnification. If the sample of interest is a biological cell, normal bright field images lack the contrast to visualize details. This drawback is due to the fact that the medium surrounding the cell has a refractive index very close to that of the cell. Small changes in illumination circumvent the problem by using different optical properties. A few of these alterations will be discussed in this chapter.

3.1 Dark Field Microscopy

Dark field microscopy is the simplest alteration of bright field imaging. The basic idea of dark field microscopy can be observed in nature every day. The sky on a sunny day has a blue color due to scattering effects of sunlight with atmospheric particles. At night however, the faint light of distant stars and the reflected sunlight of the moon can be seen. So, elimination of direct light can be utilized to enhance image contrast. In dark field microscopy, the elimination of direct light is achieved by using oblique

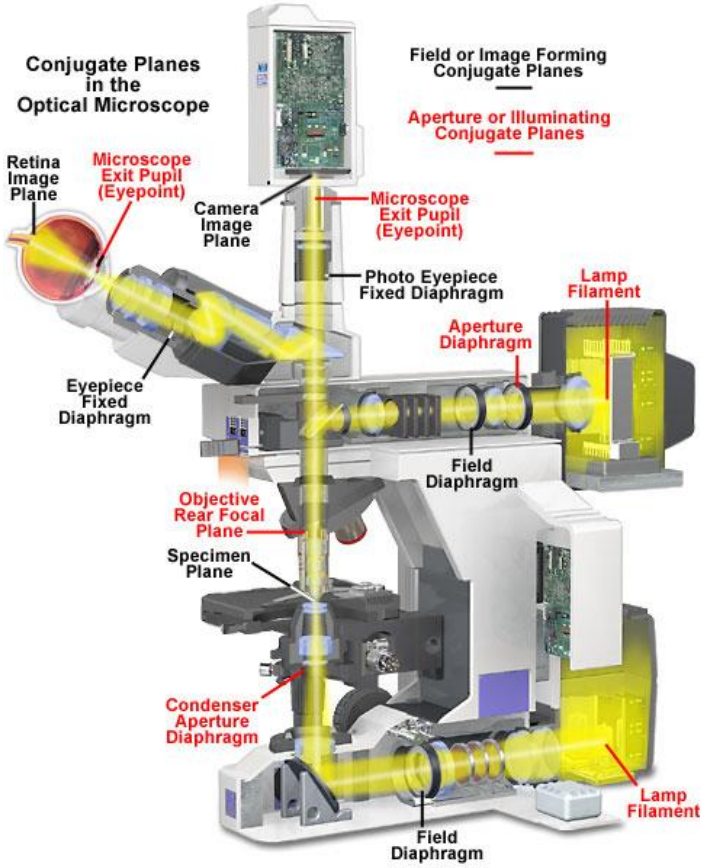

Figure 3.1: The illuminating conjugate plane set consists of the lamp filament, the condenser front focal plane, the objective rear focal plane and the microscope's exit pupil. The image forming conjugate plane consists of the field diaphragm, the specimen plane, the intermediate image plane and the retina of the eye, or the camera image plane (source: [Nikon]).

illumination. A ring shaped aperture in the condenser's front focal plane (condenser annulus) creates a ring shaped beam of light. The light is focused in a manner such that it converges to a point at the optical plane of the specimen. The focused light is directed at a large enough angle with respect to the objective such that the ring shaped direct light can not be captured by the objective lens. Therefore, the only light detected by the objective, is light that was scattered by the specimen. Dark field microscopy enables visualization of high contrast images with refractive index boundaries. On the downside, this method only works with thin samples, because image quality suffers with rising number of scattering effects in thick samples.

3.2 Phase Contrast Microscopy

The concept of oblique illumination is also used in phase contrast microscopy. In addition to dark field microscopy, phase contrast microscopy uses a combination of indirect and direct light to achieve contrast enhancement. The refractive index difference between sample and medium results in different velocities of light waves passing through the sample and the medium. The difference in velocity leads to a phase shift that depends on refractive index difference and thickness of the sample (optical path length). Undeviated and diffracted light collected by the objective is segregated at the rear focal plane by a phase plate and then focused at the intermediate image plane to form the final phase contrast image observed in the eyepieces. The phase plate shifts the phase of the oblique light in a manner such that the undisturbed light can interfere with the light passing the sample. The interference represents the difference in the optical path length, yielding a high contrast image.
The phase contrast microscopy is an excellent method for enhancing contrast in thin biological samples. It enables the visualization of internal cellular components (e.g nuclei, mitochondria, golgi apparatus) using the relatively high refractive index difference of organelles to water. However, refracted light that enters the part of the phase ring dedicated to the undeviated light leads to unwanted disturbances of the image (halo and shade-off effects).

3.3 Fluorescence Microscopy

With the discovery of fluorspar (calcium fluoride) by Sir George Gabriel Stokes in 1852 and the green fluorescent protein GFP in 1961 by Osamu Shimomura [Shimomura et al., 1962], the effect of fluorescence could be used to enhance image quality. Today, fluorescence microscopy is one of the most commonly used imaging techniques in biological science. The basic properties and limitations of fluorescence microscopy will be discussed in this chapter.

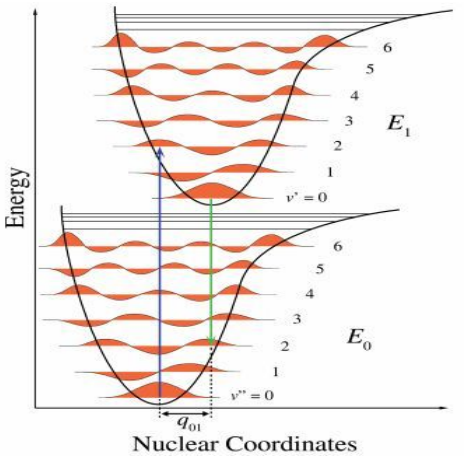

(a)

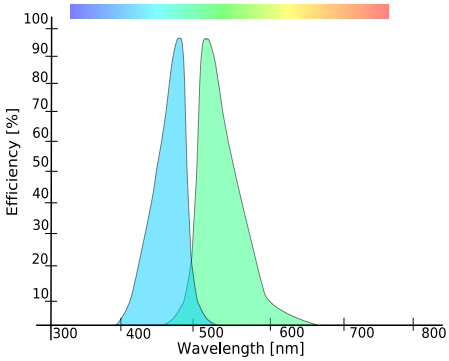

(b)

Figure 3.2: (a) Franck-Condon Diagram for a molecule consisting of two nuclei described by a Morse potential. The y-axis represents the energy bands, denoted ν and on the x-axis the distance between the two nuclei is drawn. After excitation the potential moves to a higher energy and larger distances. (b) Fluorescence-Emission spectrum of Alexa Fluor 488 (excitation peak left - emission peak right). One can see the Stokes shift, originated by vibrational relaxation of electronically excited states (source: [ZEISS]).

3.3.1 Fluorescence Emission and Excitation

Fluorescence belongs to the family of luminescence, which describes the ability of substances to emit light in response to physical, mechanical, or chemical excitation of electron states. The physical process of excitation by light and emission of a photon is called photoluminescence. Fluorescence occurs due to the transition of an electronically excited state to the ground state by emitting a photon.

The basic mechanism of fluorescence is described by the the Frank-Condon principle. It predicts that the transition most likely to happen occurs where the overlap of the wave function of the excited state with the wave function of the ground state is the biggest (Fig. 3.2a). Due to this principle, molecules experience several vibrational relaxations before emitting a photon and the emitted photon is red-shifted (Stokes shift) with regard to the exciting photon (Fig. 3.2b).

Light absorption by a solution of fluorescent molecules (fluorophores) can be described by the Lambert-Beer law. This law states that the absorbed intensity I_{abs} is an exponential function of the incoming monochromatic light with intensity I_0

$$I_{abs} = I_0 \cdot e^{-\epsilon c d} \ , \tag{3.1}$$

where the extinction coefficient of the fluorophore is $\epsilon = \frac{4\pi k}{\lambda}$, the fluorophore concentration is c, the sample thickness is d and the wave vector is k. The emitted fluorescent signal I_{em} depends linearly on the absorbed intensity I_{abs} and the quantum efficiency Φ_{fl} of the fluorophore. For small $\epsilon c d$ the emitted intensity is given by

$$I_{em} = I_{abs} \cdot \Phi_{fl} = (I_0 - I) \cdot \Phi_{fl} = I_0 \cdot \Phi_{fl}(1 - e^{-\epsilon c d}) \approx I_0 \Phi_{fl} C \ , \tag{3.2}$$

where C is a constant.

3.3.2 Resolution Limit

The resolution limit of a light microscope is based on the wave structure of light. Passing through a light microscope, every incident light spot is spread through a certain region to the final projection area, as described by the point spread function. Two adjacent spots can be distinguished if the central maximum of the one point falls on the first tail maximum of the second point (Rayleigh-Criterion). The Abbe Limit originally developed by Ernst Abbe, describes this fact quantitatively. The limit states that a detail with a particular spacing in the specimen is resolved when the numerical aperture (NA) of the objective lens is large enough to capture the first-order diffraction pattern produced by the detail at the wavelength employed. The numerical aperture NA of a lens describes the lens's ability to collect or emit light and is defined as

$$NA = n \cdot \sin\left(\frac{\alpha_{ap}}{2}\right) \tag{3.3}$$

with n being the refractive index of the medium in front of the lens and α_{ap} being the aperture angle of the lens. A common method to enlarge NA is the use of an oil immersion objective (Fig. 3.3b) instead of a dry objective (Fig. 3.3a). For these kind of objectives, oil is placed between the lens and the glass slide of the sample, such that the refractive index matches that of the lens and the glass. The lateral resolution limit

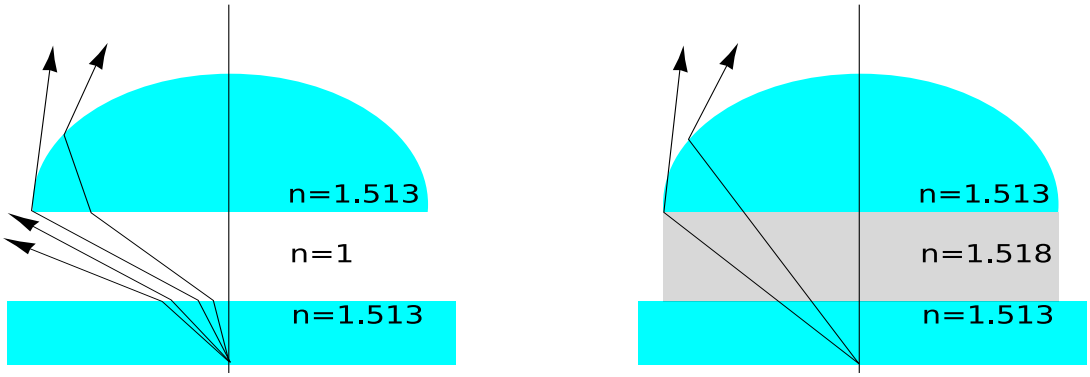

Figure 3.3: (a) Dry setup with an air interface. The obective lacks the ability to collect big angles. (b) Matching the refractive index of the interface with immersion oil allows the use of a broader spectrum of angles, thus enhancing the resolution by increasing the Numerical Aperture.

R_L^{lat} is given by

$$R_L^{lat} = 0.61 \cdot \frac{\lambda}{NA} \ , \tag{3.4}$$

where λ is the wavelength of the light used. Accordingly, the axial resolution limit R_L^{ax} is

$$R_L^{ax} = \frac{2\lambda n}{NA^2} \ . \tag{3.5}$$

According to Nyquist's sampling theorem [Nyquist, 1928], lossless digitalization can only be achieved if the sampling rate is at least twice the maximum frequency response. Thus, at least two pixels are needed to recover the full information in the image and the observer (CCD camera or photoreceptor of the eye) reaches a lateral image resolution of $2 \cdot pixel\ size$. The maximum possible magnification M is now the ratio of the observer resolution over the resolution limit given by the objective.

$$M = \frac{2 \cdot pixel\ size}{R_L^{ax}} \tag{3.6}$$

For this work an objective with a NA of 1.45 and a magnification of 100 as well as a laser with a wavelength of 488 nm is used. Using these parameters results in a

maximum lateral resolution of 205 nm and a maximum axial resolution of 617 nm. The CCD camera has a pixel size of 6.45 μm, yielding a highest possible magnification of about $M = 63$. It could be advantageous to use a higher magnifying objective, in order to avoid Moirèe effects that might arise due to the same order of magnitude between the resolved structures and the sensor matrix. On the other hand, image brightness suffers when using high magnifying lenses. The amount of this "empty magnification" should be considered, and as a basic rule, a magnification of about 500 to 1000 times the numerical aperture is preferable in order to find a compromise between image brightness and Moirée effects. For an objective with a magnification of 100, an eyepiece with a magnification of ten and a numerical aperture of 1.45, the magnification is 690 times the NA.

Several methods exist to circumvent this resolution limit. One way is to use a near field microscope, which uses the highly distance depending near field [Jahanmir et al., 1992]. Another method uses metamaterials or materials, where the imaginary part of the refractive index is negative (e.g. silver), to transport the information contained in the near field to a normal far field objective. This method can then resolve structures down to a size of about 70 nm [Liu et al., 2007; Smolyaninov et al., 2007]. Another very elegant method is the 4-π-STED microscope developed in the group of professor Hell and commercially available from Leica Inc.. This method is based on the use of a confocal laser microscope. A common objective captures part of a half-sphere of the emitted light. The 4-π microscope uses two objectives, which collect the emitted light of the specimen from both sides thus enlarging the effective numerical aperture to maximize the resolution [Hell and Stelzer, 1992]. In a stimulated emission depletion or STED microscope one laser beam is used for normal excitation of a fluorescent molecule while a second laser beam, surrounding the exciting beam like a donut, is used to stimulate relaxation in the molecules. The following saturation effect leaves only a small excitable spot that can be as small as a single molecule [Hell and Wichmann, 1994]. Combining these methods, a better resolution in axial and lateral direction can be achieved. Finally, TIRF microscopy was used to resolve structures smaller than the

resolution limit in axial direction [Burmeister et al., 1994a; Loerke et al., 2002; Olveczky et al., 1997; Truskey et al., 1992]. In this work a TIRF microscope was chosen, because the main goal was to measure the cell/substratum interface with high axial resolution, whereas normal lateral resolution suffices to gain the necessary insights.

3.3.3 Photobleaching in Fluorescence Microscopy

Photobleaching is the irreversible decomposition of fluorescent molecules in the excited state due to diffusion driven interactions with molecular oxygen. The probability of decomposition is a constant value, leading to a reduced fluorophore lifetime described by the intensity of emission, the emission time and the number of cycles experienced by the fluorophore. The number of possible excitation-emission cycles of a typical organic dye lies between 10^5-10^6. Although photobleaching typically hinders most applications, it can be used to measure diffusion of macromolecules [Axelrod et al., 1976]. A focused light beam is used to bleach molecules in an area of interest. New molecules are transported into the area by diffusion or other associated mechanisms and can be monitored as they enter the area of interest.

3.4 Total Internal Reflection Fluorescence Microscopy

TIRF microscopy uses the principle of total internal reflection in which light is reflected but not refracted from a medium boundary and provides a means by which molecules close to the medium boundary can be imaged. Consider two media with refractive indices n_1 and n_2 ($n_1 > n_2$) and $n = n_2/n_1$. A plane wave strikes the interface between the two media with an incident angle θ. The incoming wave is partially reflected and partially transmitted in the form of plane waves. The direction of propagation of the refracted wave, described by the angle θ', can be calculated by Snell's law (Fig.3.4):

$$n_1 \sin(\theta) = n_2 \sin(\theta') \ . \tag{3.7}$$

If θ corresponds to the critical angle θ_C, the outgoing wave propagates along the

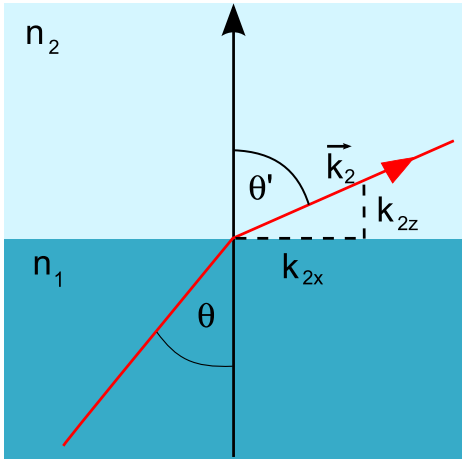

Figure 3.4: At an interface between two media with different refractive indices, the electromagnetic wave is bend towards the optically denser material with a direction described by the wave vector $\vec{k_2}$.

interface ($\sin(\theta') = 1$). The critical angel is given by

$$\theta_C = \arcsin\left(\frac{n_2}{n_1}\right) = \arcsin(n) \ . \tag{3.8}$$

In the case of glass as medium 1 and water as medium 2 ($n_1 = 1.52$ and $n_2 = 1.33$), the critical angle is $\theta_C = 63°$. If the incident angle θ_1 is bigger than the critical angle, all of the wave's energy is internally reflected. For this case, the cosine of the outgoing angle becomes imaginary:

$$\begin{aligned} \cos(\theta') &= \sqrt{1 - \sin^2(\theta')} \\ &= \sqrt{1 - \left(\frac{n_1^2}{n_2^2}\right) \cdot \sin^2(\theta)} \\ &= i\sqrt{\left(\frac{\sin(\theta)}{\sin(\theta_C)}\right)^2 - 1} \end{aligned} \tag{3.9}$$

For further analysis, only the electric part of the electromagnetic wave will be considered because the equations for the magnetic part can be deducted in a similar manner. The electric fields of incoming electromagnetic field $\vec{E_1}$ in the xy-plane and the generated outgoing electric field $\vec{E_2}$ at the time t and the position $\vec{r}$ can be described by the absolute amplitudes $\vec{E_1^0}$, $\vec{E_2^0}$, and their wave vectors $\vec{k_1} = (k_{1x}, 0, k_{1z})$ and $\vec{k_2} = (k_{2x}, 0, k_{2z})$:

$$\vec{E}_1 = \vec{E}_1^0 e^{i(\vec{k}_1\vec{r}-\omega t)} \tag{3.10}$$

$$\vec{E}_2 = \vec{E}_2^0 e^{i(\vec{k}_2\vec{r}-\omega t)} \tag{3.11}$$

For angles bigger than the critical angle, $\vec{E}_2$ can be expressed by equations (3.11) and (3.9) with the wave vector components (Fig.3.4) $k_{2x} = k_2 \sin(\theta')$ and $k_{2z} = k_2 \cos(\theta')$ as

$$\begin{aligned} \vec{E}_2 &= \vec{E}_2^0 \cdot e^{i(k_{2x}x + k_{2z}z - \omega t)} \\ &= \vec{E}_2^0 \cdot e^{i(k_2 x (n1/n2)\sin(\theta) - \omega t)} \cdot e^{\alpha z} \ , \end{aligned} \tag{3.12}$$

where the angle dependent parameter α is

$$\begin{aligned} \alpha &= k_2 \cdot i\sqrt{\left(\frac{\sin(\theta)}{\sin(\theta_C)}\right)^2 - 1} \\ &= \frac{2\pi}{n_2\lambda} \cdot i\sqrt{\left(\frac{\sin(\theta)}{\sin(\theta_C)}\right)^2 - 1} \ . \end{aligned} \tag{3.13}$$

Even in the case of total internal refraction, the electric field in the second medium does not vanish due to the continuity of the Maxwell equations for interfaces of different refractive indices. The resulting electromagnetic wave is called an evanescent wave and is in several experimental applications (surface plasmon resonance, fingerprint recognition, refractometer etc.). The conundrum of a non-zero intensity in the second medium, while having total internal reflection, is solved by the fact that the time averaged energy flux density (described by the Poynting vector) of the electromagnetic field vanishes. The evanescent wave enters the second medium, stays close to the surface and reenters the first medium again. The intensity of the evanescent wave as a function of the z-distance from the interface and the angle of incidence is given by

the absolute value of the Poynting vector. The z-component of the intensity is given by equation (3.14).

$$\begin{aligned} I(z) &= I_0 \cdot e^{-2\alpha z} \\ &= I_0 \cdot e^{-\frac{z}{d_p}} \end{aligned} \tag{3.14}$$

The field decays exponentially with the decaying constant d_p, which is called penetration depth. It defines the distance from the interface where the intensity has decreased to approximately one-third of the original intensity I_0:

$$d_p = \frac{n_2 \lambda}{4\pi} \sqrt{\left(\frac{\sin(\theta)}{\sin(\theta_C)} \right)^2 - 1} \; . \tag{3.15}$$

As can be seen in figure 3.5, the intensity at the interface reaches a maximum with an angle of incidence equal to the critical angle. The intensity reaches about 4 times the intensity of the incoming wave. This effect is called surface enhancement. With these equations, the z-dependency of the evanescent field can be expressed for s- and p-polarized electrical fields respectively as [de Fornel, 2001]

$$\vec{E}_p = E_p^0 \frac{2\cos(\theta) e^{-\frac{z}{d_p}}}{n\cos(\theta) + i\sqrt{\sin^2(\theta) - n^2}} \left[-i\sqrt{\sin^2(\theta) - n^2} \cdot \vec{e_x} + \sin(\theta) \cdot \vec{e}_z \right] \tag{3.16}$$

$$\vec{E}_s = E_s^0 \frac{2\cos(\theta) e^{-\frac{z}{d_p}}}{\cos^2(\theta) + i\sqrt{\sin^2(\theta) - n^2}} \cdot \vec{e}_y \tag{3.17}$$

3.4.1 Fluorescence Emission and Excitation

Fluorescent molecules close to the interface will get excited by the evanescent field. The moment the evanescent field passes the fluorophore, the evanescent field is transformed into a normal propagating field that leads to an excitation of the electron states of the fluorophore. According to the Lambert-Beer law, the emitted fluorescence signal

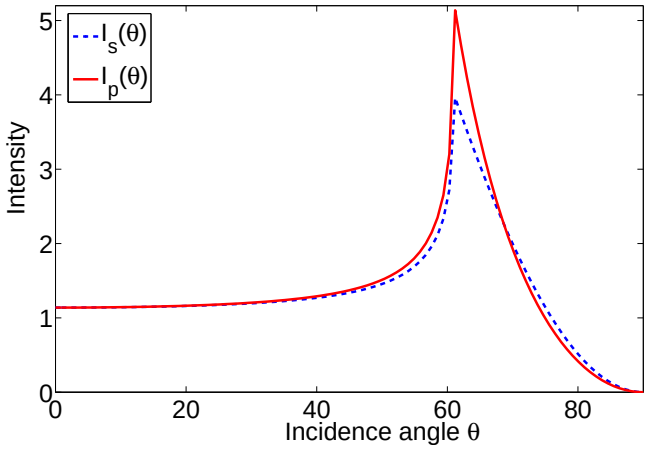

Figure 3.5: Electric field intensity at the interface of the media as a function of the incidence angle θ, for p and s polarisation, respectively. The critical angle for this figure is 61°.

F depends linearly on the absorbed intensity. Inserting equation (3.2) into equation (3.14), the fluorescent signal $F_{x,y}(\theta_1)$ at every xy-position in the sample plane can be expressed by:

$$F_{x,y}(\theta) = I_{x,y}(0,\theta) \cdot \int_0^\infty D_{x,y}(z) e^{-z/d_p(\theta)} dz \tag{3.18}$$

$I_{x,y}(0,\theta)$ is the intensity of the evanescent field at the interface while $D_{x,y}(z)$ is the z-distribution of fluorophores.

3.4.2 Three Dimensional Height Profile

The intensity of the evanescent wave decays exponentially with respect to distance from the glass interface as can be seen in equation (3.18). Thus, the intensity of the fluorescent emission at any angle of incidence bigger than the critical angle contains information about this distance. Burmeister et al. [1994a] generated a theory to use this relationship for a cell with labeled cell membrane. Based on this theory, an equivalent theory for extracellular staining was established to fit the experimental parameters.
For extracellular staining, the fluorophore resides in the cleft between cell and glass

interface. For a given height h_{xy} at every lateral position (x, y), the fluorescent intensity becomes

$$F_{xy} = I_{x,y}(0, \theta) d_p(\theta)(1 - e^{-h_{xy}/d_p(\theta)}) \ . \tag{3.19}$$

The intensity for an infinite fluorophore layer thickness is

$$F^0_{xy} = I_{x,y}(0, \theta) d_p(\theta) \ . \tag{3.20}$$

If these two expression are divided, which would correspond to an image of a cell divided by a reference image without the cell, the height can be calculated as

$$\begin{aligned} \frac{F_{xy}}{F^0_{xy}} &= (1 - e^{-h_{xy}/d_p(\theta)}) \\ h_{xy} &= -d_p(\theta) \ln \left(\frac{F_{xy}}{F^0_{xy}} - 1 \right) \ . \end{aligned} \tag{3.21}$$

Although equation (3.21) would suffice to reconstruct the cell-substratum interface, the experimental setup always introduces an offset into the equations. This offset can be caused by stray light effects, auto-luminescence of internal parts of the microscope, or photobleaching to the cell. In order to address this problem, the amount of information needs to be increased. One possible way is to use several angles of incidence in an approach called Variable-Angle-TIRF (VA-TIRF).

3.4.3 Theory of Variable-Angle-TIRF Microscopy

Equation (3.18) shows that the fluorescent signal depends on the angle of the incident light. The basic idea of Variable-Angle-TIRF (VA-TIRF) is to use this dependency to calculate the actual distance z between the fluorophore and the glass surface. Following a publication by Ölvezcky et al. [Olveczky et al., 1997], a strategy to achieve this

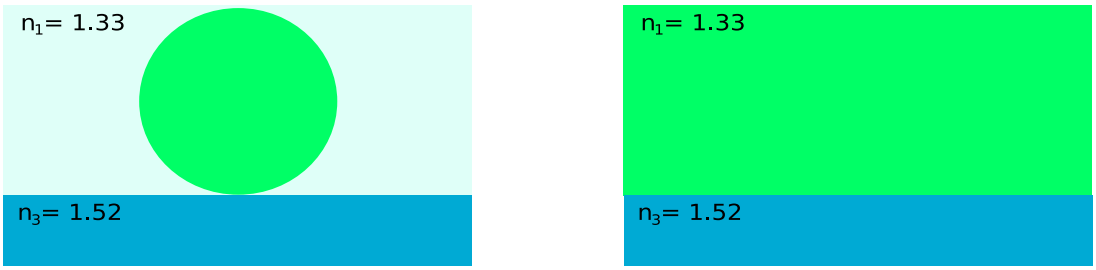

(a) (b)

Figure 3.6: (a) A spherical fluorophore distribution in water on top of a glass substrate. (b) The homogeneous fluorophore distribution serves as reference to eliminate $I_{x,y}(0,\theta)$

objective, first eliminates the unknown angle dependent intensity distribution $I_{x,y}(0,\theta)$ and then uses an analogous model as a guideline for the distance calculations.
In order to explain VA-TIRF, two model systems may be considered. A spherical fluorophore distribution is positioned in a liquid with refractive index $n_1 = 1.33$ on top of a glass surface with refractive index $n_3 = 1.52$ (Fig. 3.6a) and a homogenous distribution with a constant concentration c_{ref} of fluorophores (Fig. 3.6b). The fluorescent signal for the spherical distribution is described by equation (3.18). After integration over z, the signal for the constant distribution becomes

$$F_{x,y}^{ref}(\theta) = I_{x,y}(0,\theta) c_{ref} d(\theta) \ . \tag{3.22}$$

The two equations can be expressed as a function of $p = 1/d(\theta)$:

$$G_{x,y}(p) = \frac{F_{x,y}(\theta)}{F_{x,y}^{ref} \cdot p(\theta)} = \frac{1}{c_{ref}} \int_0^\infty D_{x,y}(z) e^{-zp} dz \tag{3.23}$$

In equation (3.23), $G_{x,y}(p)$ corresponds to the Laplace transformation of the fluorophore distribution $D_{x,y}(z)$. The Laplace transform enables the recovery of the fluorophore distribution values by the inverse Laplace transformation of the measurable parameter $G_{x,y}(p)$. Thereby, the functional form of the Laplace transform can be deducted, thus allowing a direct fit of the data. In general, three cases can be distin-

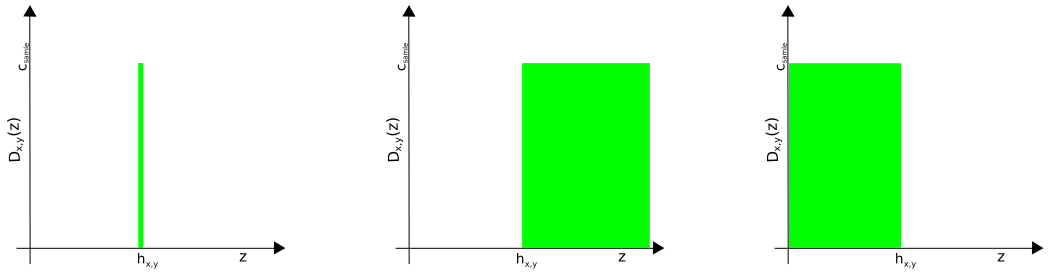

(a) (b) (c)

Figure 3.7: Different fluorophore distributions used as a model for fitting: (a) Staining of the cell's membrane, (b) staining of the cell cytoplasm and (c) staining of the medium surrounding the cell

guished in cell measurements: (i) Staining of the cell membrane, (ii) staining of the cell's interior by staining the cytoplasm, and (iii) staining of the medium surrounding the cell by dissolving a membrane impermeable dye in the medium. In all the cases, the assumption can be made that the field intensity at distances bigger than half the cell diameter is zero. Therfore only half of the sphere has to be considered in the sphere model. With this assumption the fluorophore distribution in the first case becomes a delta function (Fig. 3.7a) $[D_{x,y}(z) = c_{sample} \cdot \delta(z - h_{x,y})]$ with a fluorophore concentration c_{sample} and the distance $h_{x,y}$ between fluorophore and glass surface. The resulting Laplace transform is

$$G_{x,y}(p) = k \cdot e^{-ph_{x,y}} + C \ , \tag{3.24}$$

with k being a global constant describing the quotient of the fluorophore concentrations $\frac{c_{sample}}{c_{ref}}$ and C being an integration constant describing the offset of the measurement. The distribution in the second case (Fig. 3.7a) can be expressed as a shifted step function $[D_{x,y}(z) = 0$ for $z < h_{x,y}$ and $D_{x,y}(z) = c_{sample}$ for $z > h_{x,y}]$ where the corresponding Laplace transform is

$$G_{x,y}(p) = k\frac{1}{p}e^{-ph_{x,y}} + C \ . \tag{3.25}$$

Uniform staining of the medium (Fig. 3.7c) can be described as a top-hat function [$D_{x,y}(z) = c_{sample}$ for $z < h_{x,y}$ and $D_{x,y}(z) = 0$ for $z > h_{x,y}$] with the Laplace transform

$$G_{x,y}(p) = k\left(\frac{1}{p} - \frac{1}{p}e^{-ph_{x,y}}\right) + C \ . \tag{3.26}$$

The procedure of measuring the z-distribution of fluorophores first includes a measurement of the sample and construction of the Laplace transform by dividing with a reference image, consisting of a fluorescent dye dissolved in a liquid. Then, the angle dependent intensity values for every pixel are fitted with the corresponding model function. For further image enhancement, a correction factor must be included to compensate for near-field effects (App. B).

3.4.4 Photobleaching in VA-TIRF

The equations of the last section assume a constant fluorophore distribution over time. Photobleaching changes this constant distribution to a function because of the irreversible destruction of fluorescent molecules. Photobleaching can be described as a first order transition with a rate constant $\gamma I_{x,y}(z)$. Starting for $t = 0$ with a fluorophore concentration $D_{x,y}(z, 0)$, the time dependent concentration $D_{x,y}(z, t)$ can be expressed as [Axelrod et al., 1976]

$$\frac{D_{x,y}(z,t)}{dt} = -\gamma I_{x,y}(z) D_{x,y}(z,t)$$

$$\Rightarrow D_{x,y}(z,t) = D_{x,y}(z,0)\mathrm{e}^{-\gamma I_{x,y}(z)t} \ . \tag{3.27}$$

Since the fluorophore concentration itself depends on the distance z from the interface, the effect of photobleaching has to be considered, or at least minimized, to use the theory of VA-TIRF. Close to an interface with a higher refractive index (see appendix B), the decay does not depend only on the excitation light intensity, but also on near field effects [Hellen and Axelrod, 1987]. The decaying rate of the fluorophores changes due to three different effects. First, the decaying rate is altered because of interferences between the light directly emitted by the fluorophores and reflections by the interface. Second, interactions between the near field of the fluorophore and the optical denser medium can lead to far field radiation. And third, the surface can be an absorbing medium that dissipates energy into heat. The last two effects enlarge the total dissipated power, leading to a further decrease in fluorescent lifetime near the interface.

4 Experimental Setup (VA-TIRF)

4.1 The Microscope

The TIRF microscope used in this work was a system offered by ZEISS (Fig. 4.1). It consisted of an Axiovert 200 M microscope with TIRF equipment (ZEISS, Göttingen, Germany). The Axiovert 200 M is an inverse microscope, allowing simultaneous brightfield and fluorescence imaging. Most of its features can be controlled with a computer and the ZEISS software AxioVision. The microscope is equipped with a condenser for brightfield illumination. The condenser contains three phase rings for phase contrast microscopy. The sample can be put inside an incubation chamber, which was used to control temperature and CO_2 concentration for optimal cell viability.

4.1.1 Illumination

The used setup allowed three different types of illumination in one experiment, brightfield, epi-fluorescence, and TIR-illumination.

4.1.1.1 Brightfield Illumination

Brightfield illumination is done through the microscope's condenser. The light source is a standard tungsten halogen lamp that emits white light.

4.1.1.2 Epi-Illumination

Epi-fluorescence illumination is achieved by a mercury arc lamp. The arc lamp is coupled into the optical train of the microscope using a rear port. The microscope

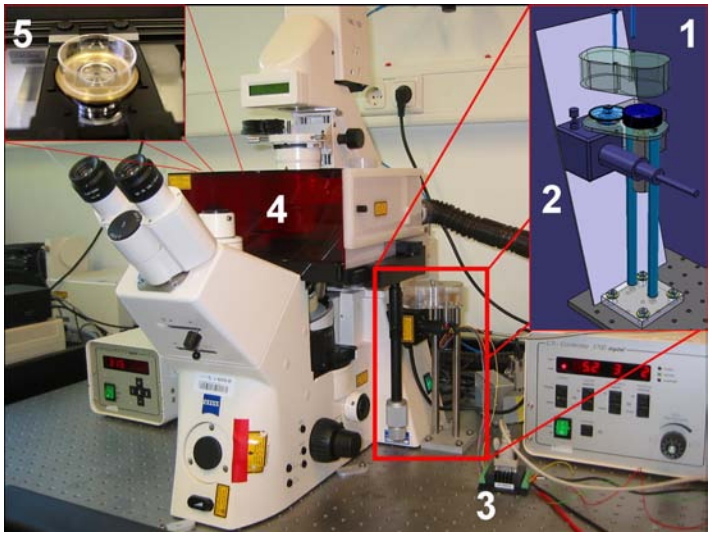

Figure 4.1: The experimental setup for TIRF measurements. A motor (1) was attached to the TIRF-slider (2) and controlled with a motion controller (3). The sample was put into an incubation chamber (4), where temperature and CO_2 concentration could be controlled and resided on a sample support (5).

offers an equivalent back focal plane to that of the objective. For diffused illumination of the sample plane the equivalent back focal plane is used to image the arc lamp.
The mercury arc lamp excites fluorescent molecules with a broad variety of intensities, ranging from the ultraviolet to infrared parts of the spectrum of light. The illumination across this spectrum is not homogeneous due to the mercury, but exhibits several peak intensities for wavelengths like 313 nm, 365 nm, 435 nm, and 546 nm. An optical filter system is used to obtain the wavelength combination of interest (Filter Set 09, ZEISS, Göttingen, Germany). The incoming broad spectrum emitted by the arc lamp is passed through a pair of band filters (in our case an excitation filter of $450-490$ nm and an emission filter of $515-800$ nm). A dichromatic beam splitter [1] that is tilted at a 45° angle with respect to the incoming excitation light is used to couple the incoming light into the objective. The excitation light stimulates fluorescent molecules to emit light. The emitted light is collected by the objective and unwanted wavelengths are

[1] Dichromatic beam splitters use interference effects to separate light of different wavelengths. Several layers of evaporated dielectric substances on the surface of the splitter reflect the light in a way that interference leads to the passage of light with a wavelength under a threshold value and the reflection of light exceeding this threshold. Thus, the principle of dichromatic beam splitters differ from the principle of optical filters, which relie only on the absorption of certain frequency bands.

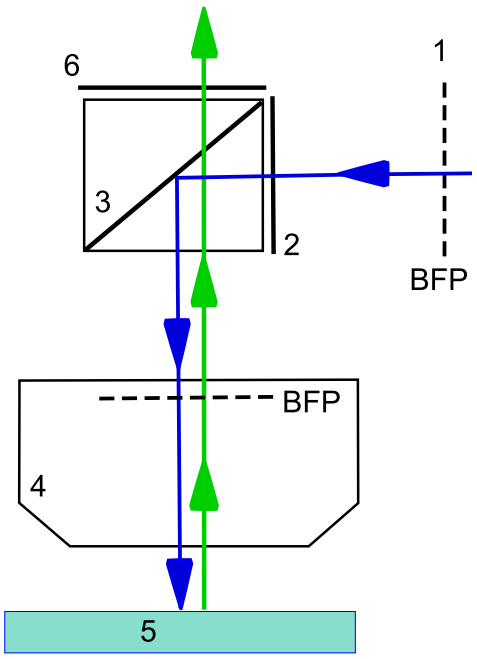

Figure 4.2: Schematic diagram of epi-illumination. The incoming light is focused on the back focal plane (BFP, 1) and all but the desired wavelengths are fitered by an excitation filter (2). The dichroic mirror (3) reflects the incoming light in a way that it is focused on the sample plane (5) through the objective (4). The emitted light is captured by the objective, transmitted through the dichroic mirror (3), and filtered by an emission filter (6).

blocked by another optical filter. Since the emitted light has longer wavelengths, it is reflected by the dichromatic beam splitter and enters the image forming parts of the microscope, creating an image on the imaging device.

4.1.1.3 TIR Illumination

A 100 mW multiline argon ion laser (LGK 7812 ML4, Lasos, Olching, Germany) delivering lines of 456 nm, 488 nm and 514 nm serves as illumination source for TIR illumination. The laser light is s-polarized and is coupled into an element called TIRF slider (Sect. 4.1.3) by an optical fiber. The laser housing contains a shutter device for fast switching of the laser illumination. As for the case of epi-illumination, the laser line of interest was selected using optical filter sets (Filter Set 51/52/53, ZEISS, Göttingen, Germany) with a narrow range of wavelength (excitation ±5 nm / emission ±15 nm).

4.1.2 Objective

The objective used in this work was a 100× plan-Fluar objective with a numerical aperture of 1.45 (α Plan Fluor 100×/1.45 oil, ZEISS, Göttingen, Germany). A system

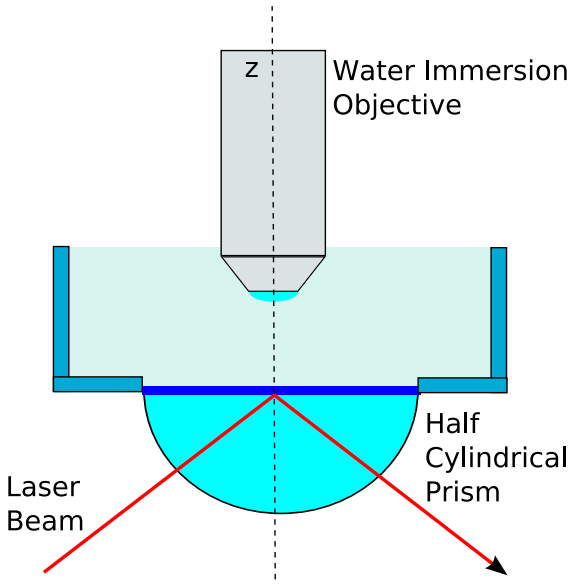

Figure 4.3: A prism based TIRF setup used by Loerke et al. [2000] to measure vesicle diameter and interface distance in living cells. The laser light is coupled to the microscope by means of a hemispherical prism. The created evanescent wave shows a high degree of homogeneity.

of lenses (e.g. lens doublet groups) made of different materials are used to address several optical aberrations [Murphy, 2001]. Fluar objectives, originally made of fluorite, correct for wavelength from 340 to 800 nm. However, these objectives suffer from pronounced field curvature which leads to curved rather than flat projections of the sample. Plan-Fluar objectives use complex lens designs (e.g. more lens doublet groups and lens triplet groups) to correct for field curvature and to yield flat images up to about 23 mm.

4.1.3 The TIRF Slider

TIRF microscopy is realized by oblique laser illumination. Two main approaches exist to create this kind of illumination: illumination through a prism and the prismless through-the-objective technique. In the first approach, a prism is used to create high incident angles of the laser beam (Fig 4.3). Because this method relies on relatively few components, scattering effects that arise at every interface can be kept low.

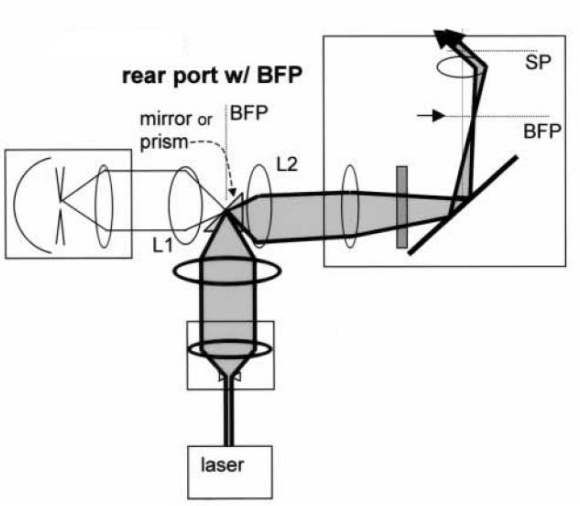

Figure 4.4: The TIRF slider couples the laser light into the optical system of the microscope by using the back focal plane (BFP). A birefringent prism is used in order to illuminate the sample with laser as well as with normal epi-fluorescent light. A screw controls the position of the prism, which changes the angle of incidence (source: Axelrod [2001]).

Angle	d_p [nm]	Deviation of d_p [%]
63°	157.9	14.1
65°	110.34	6.9
67°	90.62	3.6
70°	75.31	1.8

Table 4.1: Deviation of the penetration depth d_p for a variation of the angle of 0.5°

In this work the through-the-objective, or prismless technique [Stout and Axelrod, 1989] was used. The prismless technique is based on the fact that off-axis laser light at the back focal plane of an objective leaves the objective lens under an angle. In order to gain only a narrow spread of angles, it is imperative to focus the laser beam in the back focal plane. The focus was set in this work by observing the spreading of the laser beam at a high distance (i.e. ceiling of the room). The smallest possible spread of the beam gave the smallest possible spread of angles. With an approximate distance of $d = 1.5$ m between the objective and and a smallest possible beam spreading of 3 cm, the angle can be set with an error of $\pm 0.5°$. This added to a total error in penetration depth, which can be found in Tab. 4.1.

Since the objective used in this work was a plan-fluar objective, peripheral beams were also in focus and the angle under which the laser left the objective can be calcu-

lated by the Abbe-condition [Linke, 2004]:

$$\sin\theta = \frac{r}{n f_{obj}} \ , \tag{4.1}$$

where r is the radial distance of the focused laser beam from the back focal plane center, n is the refractive index of the objective's lens and f_{obj} denotes the focal distance of the objective. Equation (4.1) shows that the angle grows with radial distance from the back focal plane axis. In order to reach angles big enough for TIRF microscopy, the highest possible angle has to exceed a threshold given by the critical angle which depends on the refractive indices of the immersion oil and the specimen. Given a refractive index of $n_3 = 1.518$ for the oil and a refractive index of approximately $n_1 = 1.33$ for the specimen (cell with medium), the critical angle is $\theta_C = 61.2°$. The highest possible accessible angle is given by the numerical aperture of the objective. For a numerical aperture of $NA = 1.45$, the maximum angle is $\theta_{max} = 73°$. Inhomogeneities in the sample, like organelles and the cell membrane, possess higher refractive indices (approx. $n_{IH} = 1.37 - 1.4$) which lead to higher TIR angles. TIRF images at angles close to θ_C will show illumination artifacts because inhomogeneities will convert some of the evanescent field into scattered propagating light (Fig. 4.5). This fact set a lower limit for VA-TIRF at angles bigger than approximately 66°. The laser light was coupled to the optical path of the microscope with a fiber and the TIRF slider (ZEISS, Göttingen, Germany) (Fig. 4.4). The TIRF slider introduced the laser light into the rear port of the microscope, normally used by the arc lamp. An equivalent back focal plane for the arc lamp existed in the rear part of the optical path where the arc lamp is normally imaged. This back focal plane was used to focus the laser beam. The radial position of the laser beam can be set with a birefringent [2] prism, which is integrated in the TIRF slider. The prism is controlled with a screw, which was controlled by a motor in our setup (see section 4.1.4).

[2] Birefringence is the ability of optical anisotrope materials to decompose a beam of light in an ordinary and an extraordinary part.

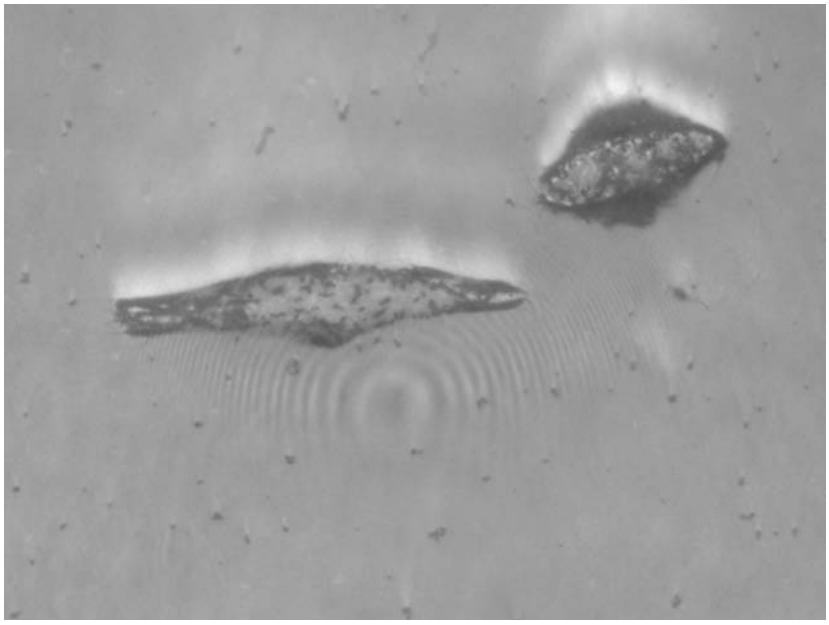

Figure 4.5: TIRF image of the footprint of two HEK cells. For the image, the extracellular medium was stained with Alexa Fluor 488. The image was normalized by a reference image. The interference artifacts in the middle, are due to the laser illumination. The bright shadows starting from the upper part of the cells, are due to the higher refractive index of the cell membrane, converting the evanescent field into a normal propagating wave.

One advantage of a prismless TIRF setup is the good accessibility of the sample. Furthermore it was possible to use TIR-, epi- and brightfield illumination in the same experiment. However, one big disadvantage of this method is that illumination is not only due to the evanescent field. A fraction of the illumination originates from scattering effects inside the objective and parts of the observed fluorescence intensity are due to luminescence of internal elements of the objective [Mattheyses and Axelrod, 2006]. The prismless through-the-objective technique is a perfect tool for biological experiments that use different types of illumination or integrate TIRF into other systems without the necessity to control the parameters of the evanescent field in detail (e.g. Ide and Yanagida [1999]). Prism based TIRF on the other hand is usually less expensive and creates “cleaner” TIRF images, but the choice of objectives and illumination sources is limited [Axelrod, 2001]. All quantitative characterizations of the cell substratum interface reported in literature so far were performed using a prism based

TIRF microscope (e.g. Olveczky et al. [1997], Reichert and Truskey [1990], Burmeister et al. [1994b] and Geggier and Fuhr [1999]). One aim of this work was to examine the possibility of using the through-the-objective TIRF microscopy for this purpose.

4.1.4 The CCD Camera

The CCD camera used to capture images is an essential part of the microscope. All TIRF measurements in this thesis were done with a cooled ZEISS Axiocam MRm (ZEISS, Göttingen, Germany). The camera has to fulfill several prerequisites, regarding pixel size, sensing area, sensitivity, low level of noise, and color depth. The size of the sensor pixels of the camera has to be small, because it partly limits the spatial resolution and determines the highest possible magnification of the system. For the AxioCam MRm the pixel size was 6.45 μm $\times$ 6.45 μm and the numerical aperture was $NA = 1.45$. This combination lead to a highest possible magnification of 63$\times$. The sensor area is the area given by the pixel size and the number of pixels. The number of pixels was 1388 $\times$ 1040, or 1.4 mega pixel. The sensitivity of the camera reached a maximum in the range of 400 nm $-$ 700 nm, which is the region of interest. In order to achieve low-noise images, the camera was cooled by a peltier element. The cooling decreased the appearance of rogue signals detected by the sensor chips. The color depth of the camera was 12 bit, enabling the recognition of 4096 different color values.
The camera is connected to the microscope and to a computer. A TTL output signal was used to control a laser shutter (Uniblitz Shutter, Vincent Associates, Rochester, USA) to set the status of laser illumination. The shutter itself had an trigger output which was used to connect the motor that controls the angle of incidence of the laser beam to the microscope.

4.2 The Motor

In our microscope setup, the angle screw of the TIRF-slider controled the incident angle of the laser beam by moving a birefringent prism. In order to achieve a fully

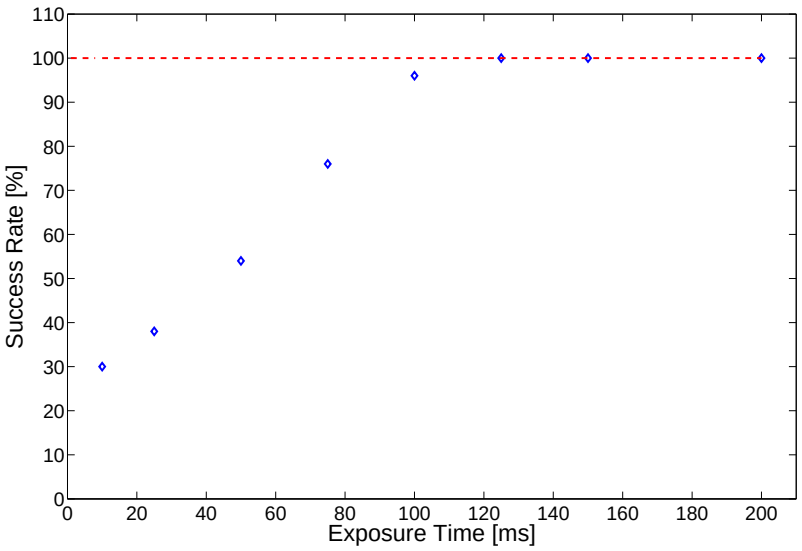

Figure 4.6: The automated change in incident angle by the motor worked without error for camera exposure times exceeding 100 ms. The figure shows the percentage of the successful motor movements after image acquisation in dependency of the exposure time of the camera.

automated and reproducible setting of the angle, the angle screw was connected to a motor. We chose a brushless motor (2036 U 024 B, Dr. Fritz Faulhaber, Schönaich, Germany) equipped with a gearing to improve sensitivity for this purpose. This configuration lead to a resolution of the motor of $10^{-5}\frac{\text{Angle}^\circ}{\text{Motor Step}}$. This high resolution was only limited by the microscope itself, especially by the angle variance arising from the prismless technique.

The motor was controlled by a computer via a Motion Controller (MCBL3006, Dr. Fritz Faulhaber GmbH, Schönaich, Germany). The controller offered a set of string commands that were used in a LabVIEW (National Instruments, USA) program. For fast and automated VA-TIRF microscopy with our setup, communication between the microscope and the motor was required. The computer read out a TTL signal sent by the laser shutter through the Motion Controller. The LabVIEW program used this signal to move the motor to a new position after image acquisition.
In this thesis, a LabVIEW program was designed to fit the parameters of VA-TIRF microscopy. It contained the ability to manually control the motor in order to find the

angle region of interest. Once found, the starting and end point for the measurement could be set, as well as the number of steps that the motor should use to scan the angle region. Furthermore it was possible to use several iterations of the same region of interest, a feature necessary for longterm VA-TIRF measurements.
The main limitation of the program was the need for relatively long exposure times of the camera (Fig. 4.6). A communication without error of the program's subroutines was achieved by using delay times of 100 ms inside the program. For exposure times of the camera smaller than 100 ms, the program was not able to control the motor in a precise way. This limitation could in future be reduced by an improved version of the software. For the measurements in this thesis this was not necessary, because the low intensities produced by the sample and VA-TIRF illumination never allowed exposure times smaller than 150 ms.

4.3 Sample Support

Sample support in VA-TIRF is an essential component in the design of the setup. Because measurements were done with living cells, the sample support had to include a culture dish. In order to focus the sample plane on the interface, the sample had to be located on a glass coverslip thinner than 0.17 mm. A combination of both was achieved by gluing cover slips underneath petri dishes with a hole drilled into the center of the petri dish. coverslips were glued using a 5 : 1 ratio of base and curing agent of PDMS (Sylgard Typ 184, Dow Corning, Wiesbaden, Germany). PDMS was used, because of its easy handling and excellent biocompatibility. The polymerization was achieved by drying the petri dish for at least 20 minutes in a 60°C drying chamber.

Since the fluorescence signal of the specimen is angle dependent, it was very important that the coverslip resided planar with respect to the objective's lens. For this purpose, a metal support for the coverslip was constructed. The support was built such that contact between sample holder and sample was only given by the coverslip. Metals are robust and can be very precisely planarized. On the other hand, metal should

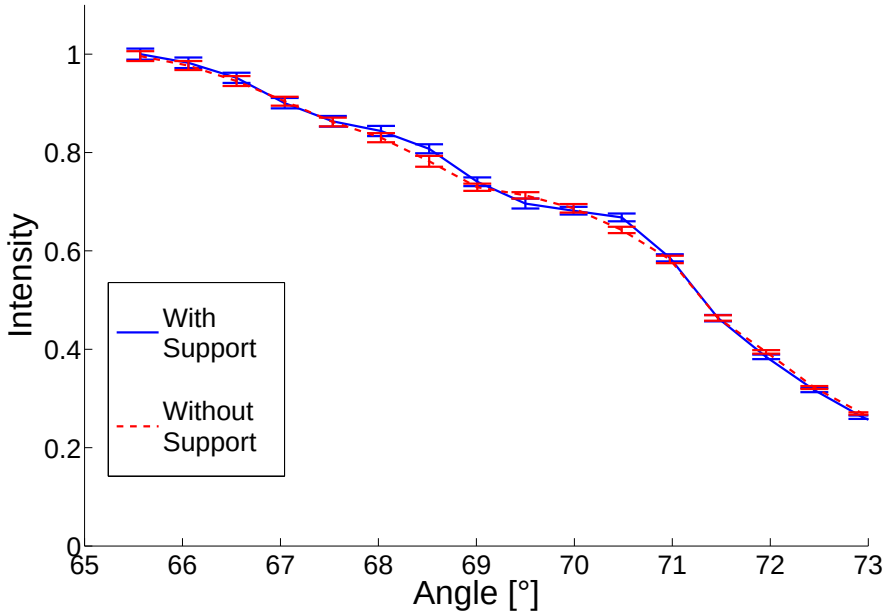

Figure 4.7: Mean integrated intensities for different angles of incidence. The values measured without the sample support (red) match the values obtained without the support (blue)

be avoided for sensitive microscopical purposes, because it is highly refractive for the range of wavelengths used in optical microscopy. For this reason, the effect of the metal support were evaluated by a comparison of fluorescent intensities with and without the sample holder. Optical effects that occurred due to scattering events with the sample support should have a bigger impact than effects created by a non planar sample, because scattering effects lead to excitation of the whole fluorescent liquid. Non-planar illumination on the other hand, changes the penetration depth of the evanescent field, thus creating stray light effects only for distances close to the glass-water interface. In order to measure the optical influence of the metal, images were generated using a fluorescent dye (Alexa Fluor 488 hydrazide, Invitrogen, Germany) in solution at different angles of incidence. The integrated fluorescence intensity of every image was measured and compared. As shown in figure 4.7, the difference between the measurements with and without the sample support were small, leading to the conclusion that the metal did not interfere significantly with measurements.

4.4 Angle Calibration of the System

The incident angle of the laser was set by the angle screw controlling the prism inside the TIRF-slider. Although the motor moved the screw in a reproducible way, the relationship between motor position and actual angle of incidence was not defined by the setup. To gain the necessary information two approaches were taken. One approach was to use a special objective (angle adjusting objective) distributed by ZEISS that images the back focal plane, whereas the second approach was to use liquids with different refractive indices.

The angle adjusting objective images the back focal plane without magnification. By this means, the radial position of the focused laser light can be directly measured with the camera. The drawback of this method was that the image contained no information about the center of the plane. Therefore, the microscope's condenser was used to measure this center. The phase ring with the biggest diameter and the objective were focused on the same plane, which consisted of a coverslip. While changing the angle of the laser, the change in laser position on the coverslip was observed at the aperture diaphragm (Fig. 3.1), which images the phase ring. The center point was reached, when the imaged phase ring was homogeneously illuminated.

Using the VA-TIRF setup, a series of 340 images was taken, starting from the center point up to a value where no illumination is normally measured in TIRF experiments. A MATLAB routine was used to calculate the xy-position of the intensity maximum in every image. The movement of the laser beam in the back focal plane can be seen in figure 4.8. Since the variation happened in x and y direction, the distance d between center position (x_m, y_m) and actual position (x, y) was calculated according to

$$d = \sqrt{(x - x_m)^2 + (y - y_m)^2} \; . \tag{4.2}$$

Since the objective does not magnify the image, d could be directly inserted into equation (4.1). Figure 4.9a shows the result of this calibration technique. This method

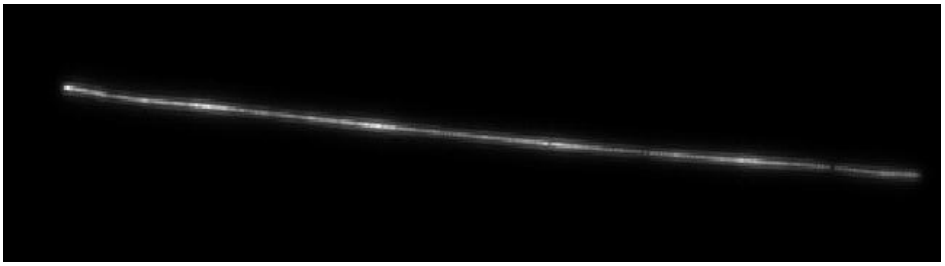

Figure 4.8: Image of the movement of the laser beam in the back focal plane. Images for 340 different motor positions were added, starting from the center position of the angle to positions where no fluorescent signal is normally detected in TIRF microscopy. The variation of the angle was not simply in one direction, but an overlap of x and y movement. The reoccuring brighter parts of the image represent areas, where the angle changed less rapidly, probably due to mechanical properties inside the TIRF-slider.

highly depended on the exact knowledge of the center point. A change of only 5 pixels of the y position of the center point lead to a change of approximately 5° in the resulting angles. In order to control these results, a second technique was necessary.

The second approach utilized to measure the incident angle of the laser was to use the effect of total internal reflection. The critical angle at which total reflection occurs is given by equation (3.7) and depends on the refractive index ratio of glass substrate and sample liquid. The refractive index of the liquid can be adjusted by using varying concentrations of several substances in solution. In this case, varying concentrations of glycerin were used to obtain refractive indices between 1.35 and 1.46. The refractive index for each concentration was measured, using an Abbe refractometer. The refractive index of the glass coverslip was taken as 1.518. The motor position corresponding to each critical angle was measured by observing the point, where the laser light was totally back-reflected into the objective. For this purpose, small amounts of fluorescent dye were added to the liquid, in order to make the laser beam observable. The results for this calibration method can be seen in figure 4.9b. Because of scattering effects inside the PDMS glue and the petri dishes design, the measurement of the motor position had an accuracy of 30000 steps, or approximately 0.1°.

For future experiments, the linear fit of the first calibration technique was taken, to calculate the angle of incidence. Before every measurement, the validity of the

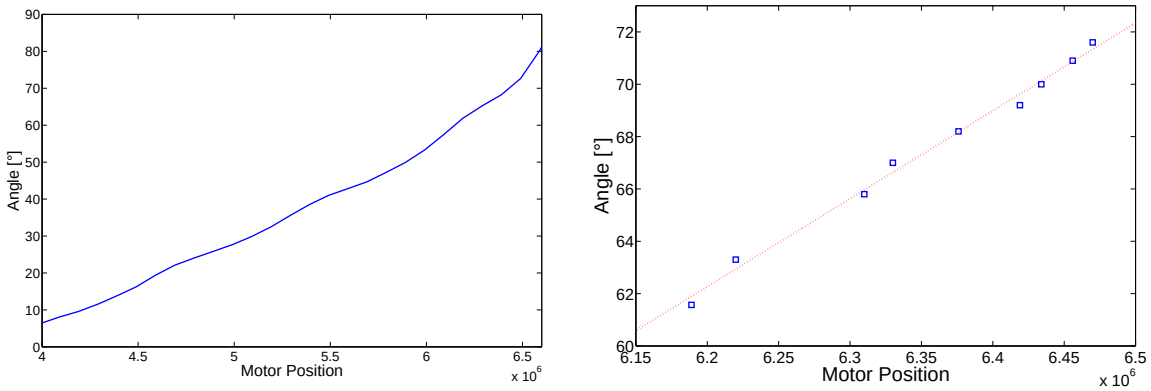

(a) (b)

Figure 4.9: (a) Measured incident angles for different motor positions using the ZEISS angle adjustment objective. Similar to figure 4.8, variation of the theoretical curve due to the prism in the TIRF-slider can be seen as periodically occuring fringes. (b) Measured motor positions for different critical angles created by refractive index variations of water/glycerin concentrations. The fit shows that the relationship is linear.

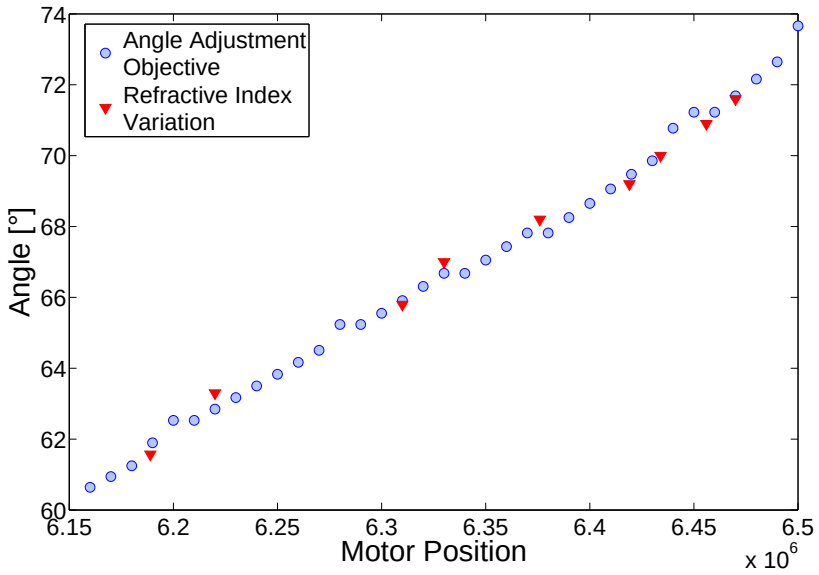

Figure 4.10: The two calibration approaches in one diagram. The values gained in the experiments overlap for angles smaller than 72°.

calibration was verified, by measuring the TIR angle in water. This precaution was necessary, because the TIRF-slider was very sensitive and the angle could be displaced by simply touching the optical fiber.

5 Methods

5.1 Microspheres as Model System

For the measurements silicate microspheres (PSi-10.0-OB, G.Kisker GbR, Germany) were put in a solution of glycerin (refractive index 1.37) and settled onto a glass coverslip. In order to keep sphere deformation due to drying low, the microspheres were readily introduced into the liquid. Approximately 10 minutes later the TIRF-measurements were performed to allow the spheres to sink down to the glass interface.

5.2 Protein Coating

One goal of this work was to determine the infuence of different proteins on cell adhesion. For the coating the glass coverslip of each petri dish was activated for 30 minutes by 20% sulfuric acid at 80° C. After activation the petri dishes were rinsed with destilled water (bidest) and sterilized by 20 minutes UV illumination. The protein solutions were prepared using the following concentrations Poly-L-Lysin, Concanavalin-A, Fibronectin, Laminin and PECM (all Sigma-Aldrich, Germany):

- Poly-L-Lysine (PLL), 0.05 mg/ml in aqua bidest
- Concanavalin-A (Con-A), 0.1 mg/ml in aqua bidest
- Fibronectin, 0.0125 mg/ml in PBS

- Laminin, 0.002 mg/ml in buffer solution (0.15 M NaCl, 0.05 M HCl, 0.05 M TRIS) at pH 7.5
- PECM: Extracellular Matrix (ECM), 10 μ l/ml in HBSS with Poly-D-Lysine (PDL), 10 μl/ml

The petri dishes were incubated with these solutions for one hour. After preparation the petri dishes were stored at 4° C prior usage (maximum storage time: 1 week).

5.3 Cell Culture

HEK cells were cultivated in a 25 ml T-flask (Greiner Bio-One GmbH, Frickenhausen, Germany), covered with M10-medium. M10 consisted of (all Invitrogen, Karlsruhe, Germany):

- Minimum essential medium (MEM) or MEM without phenolred and glutamax
- 2 mM L-Glutamin for MEM without glutamax
- 10% fetal calve serum
- 1% non essential amino acids
- 0.1 mg/ml antibioticum/antimycoticum
- 0.8 mg/ml Geneticin G418

In order to keep the cells in an exponential growth state, they were splitted every 3-4 days. Although HEK cells start to adhere after 30 minutes, cell spreading was not observed for several hours. Because the cell substratum interface should be analyzed in a state similar to that state present for electronically measurements, the cells were incubated for approximately 24 hours before observation. For the incubation, the cells were deattached from the T-flask using trypsin (Invitrogen, Karlsruhe, Germany) and put onto the protein covered petri dishes. A good compromise between high cell density and low clustering of cells were found at 40000 cells per petri dish. The cells were then incubated at 37°C with 5% CO_2 for 24 hours.

5.4 Fluorescence Staining of Cells

The fluorescence staining of the cells was an essential part of the experiment, because fluorescent signals were used to extract information about the cell adhesion area. As previously discussed, three different ways of staining can be used to gain the necessary information: extracellular staining, cell cytoplasm staining and cell membrane staining.

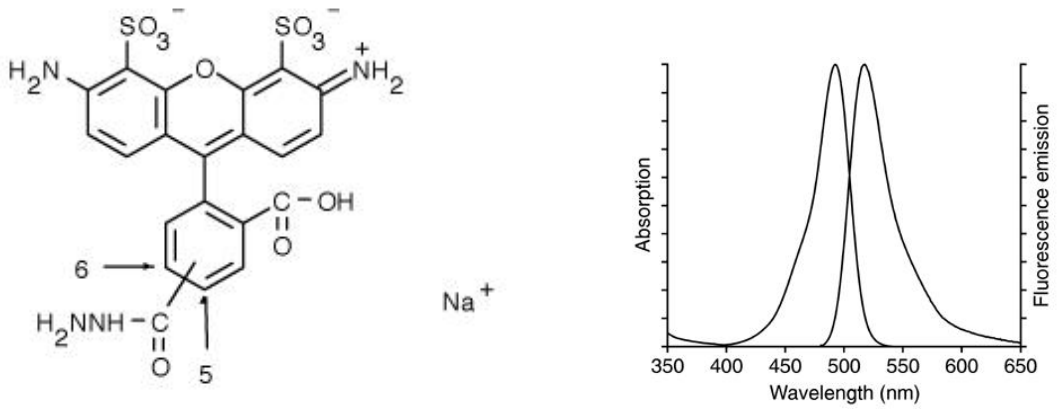

(a) (b)

Figure 5.1: Chemical structure (a) and fluorescence spectrum (b) of hydrazide conjugated Alexa Fluor 488.

Extracellular staining can be achieved by using cell membrane impermeable fluorescent dyes, like the hydrozide conjugated Alexa Fluor dyes. Alexa Fluor 488 hydrazide (Invitrogen, Karlsruhe, Germany) is a low molecular weight, polar molecule (Fig. 5.1a). Its polar nature makes the dye impermeable to the cell membrane and because of its low molecular weight, deposition of the dye at the glass substrate is kept low. The fluorescence spectrum (Fig 5.1b) is perfectly suited for the accessible wavelengths of our setup. Extracellular staining has the advantage that intracellular structures with higher refractive indices do not disturb the measurements. In a TIRF experiment, extracellular staining visualizes the contact region between glass and cell by the amount of fluorescent molecules present in the cleft. This approach is called Total Internal Reflection Aqueous Fluorescence Microscopy, or TIRAF-microscopy. In TIRAF, regions

close to the glass surface are darker than regions where the distance is bigger. The biggest observable distance is defined by the penetration depth of the evanescent field. Given an angle of incidence of 67.4°, 99% of the intensity given by an infinite distance is reached at 300 nm. So, structures observed with extracellular staining can be resolved far beyond the axial resolution limit of the microscope of 617 nm. Another advantage of extracellular staining is the possibilty to measure reference and sample images in the same experiment, minimizing effects occuring through small differences in experimental parameters, such as temperature or small air bubbles located in the immersion oil. In contrast to other staining methods, the process of photobleaching is not caused primarly by the decomposition of fluorescent molecules, but by photodamage induced to the cell. Laser illumination leads of damage to the cell membrane, through which the fluorescent dye can enter the cell and minimize the contrast of the image (Sect. 6.4.2). In order to keep the laser intensity low, the dye concentration in the liquid was chosen to be high (50μg/ml). Another reason for the use of a high concentrated low molecular weight fluorescent dye is the axial resolution of the measurements. The limit for axial resolution is partially determined by the mean distance between fluorophores, which should be small for high concentrations of low molecular weight fluorophores.

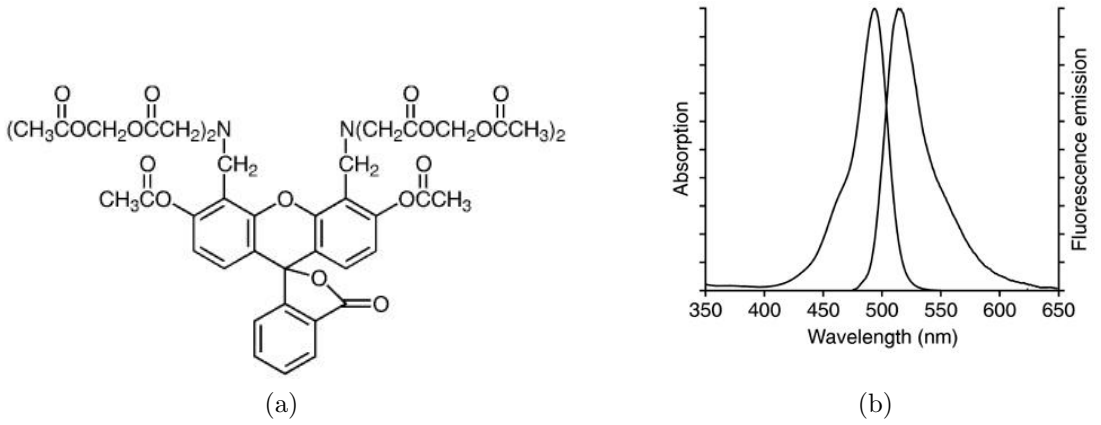

(a) (b)

Figure 5.2: Chemical structure (a) and fluorescence spectrum (b) of calcein-AM.

Intracellular staining can be done with several fluorescent dyes, one of them be-

ing calcein-AM (Sigma-Aldrich, München, Germany). Calcein-AM (Fig. 5.2a) is a commonly used cell marker that is cell membrane permeable. The non-fluorescent calcein-AM is activly converted to the negatively charged green-fluorescent calcein by removing the AM (acemethylesther) group through intracellular esterases. Only cells that are alive are able to maintain this hydrolizing process. Since the activated calcein is negatively charged, it cannot pass the cell membrane and remains inside the cell. Due to these properties calcein-AM can be also used for cell viability measurements. The fluorescent spectrum (Fig. 5.2b) is comparable to that of Alexa Fluor 488, which means that the same filter set can be used for fluorescence measurements with both fluorescent dyes. This feature is important for comparative TIRF microscopy, because the incident angle of the laser beam is different for different filter sets. If the laser beam is observed at some distance (e.g. ceiling of the room) the position shifts considerably for different filter sets. In this work calcein-AM was used to stain the cytoplasm, as well as for viability tests.

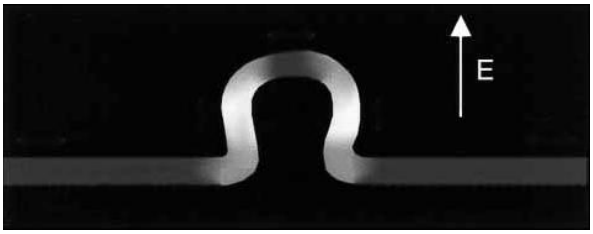

Figure 5.3: Schematic drawing of the fluorescent emission of carbocyanine fluorophores (e.g. DiO, DiI) embebbed in a cell membrane. Bright regions in the image represent areas of high levels of emission. These fluorophore are orientated parallel to the local plane of the membrane and exhibit different emission characteristics for different orientations of the membrane. The image shows the case of p-polarized laser light, but is similar for s-polarized light (source: Axelrod [2001]).

The third possibility, the staining of the cell membrane, was not proceeded in this work for two main reasons. Homogeneous staining of the cell membrane is sensitive to several factors, including dye incubation time and cell type. Furthermore, the presence of protein clusters inside the cell membrane leads to a clustering effect of the dye. In VA-TIRF, clustering of fluorescent molecules lead to different offsets in the analysis, which can be compensated by using different limits for the fitting of the data. This

results in a less accurate fit, as well as much longer calculation times. It has been shown before [Axelrod, 1979] that the intensity measured in TIRF microscopy of a fluorescent marker incorporated into the cell membrane varies with membrane orientation and laser polarization (Fig. 5.3). This effect arises, because of the anisotropic emission characteristic of the fluorescence molecule and adds a systematical error into the VA-TIRF measurements.

5.5 Cell Assays

5.5.1 Photobleaching

The effect of photobleaching was quantified for a typical experimental environment. For the measurement, HEK293 cells were plated onto glass coverslips and incubated overnight at 37° C and 5% CO_2. Before the measurement, the cells were stained intra-, and extracellularly according to section 5.4. The samples were mounted to the TIRF microscope and 250 images with exposure times of 200 ms were taken for each staining. Laser intensity and exposure time were chosen such as in the usual VA-TIRF measurements, but the overall exposure time was more than 10 fold the overall exposure time in VA-TIRF. Image processing was performed in MATLAB (MATLAB 7.0, The MathWorks, Natick, USA). For the analysis a region of interest was chosen and the intensity over exposure time to laser light was plotted.

5.5.2 TIRF Measurements

Before adding the fluorescence dye, the cells were rinsed two times with medium to wash away cell debris. For the extracellular staining of HEK293 cells, Alexa Fluor 488 was added to fresh M10-medium, which contained no red pH indicator to minimize light absorption for green and blue light. The petri dishes were then cleaned from underneath using 70% ethanol and dried with nitrogen gas, to guarantee low scattering effects. After this procedure, the sample was mounted inside the incubation chamber of the microscope for a duration of at least one hour, to allow the cells to recover from

the stress of rinsing and transport. For neuronal cells this procedure for extracellular staining was identical, but with the corresponding medium for neurons.

5.5.3 GFP-Vinculin Expression in HEK293

HEK293 cells were transfected with GFP (green fluorescent protein) labeled vinculin, which is a protein that connects integrin receptors to the cytoskeleton. For the transfection 1 μl of an escort transfection reagent (E9770, Sigma-Aldrich, Germany) was solved in 50 μl M10-medium. 1 μg of plasmid DNA (obtained from the group of Benjamin Geiger, Weizmann Institute of Science, Israel) was added to the solution, which was introduced to the HEK293 cells after 15 minutes incubation time. After two days, the cells were put onto a glass substrate. For this particular measurement, no protein coating was chosen in order to keep effects due to external factors low. The glass coverslips were put overnight in an incubation chamber and TIRF images were taken after one day incubation. For comparison, extracellular dye was added after these measurements and extracellular staining images complementary to the vinculin staining were taken.

5.5.4 Viability Test with Rat Cortical Neurons

For long term measurements with extracellular staining it had to be determined if cell viability suffered from the Alexa Fluor 488 hydrozide dye. The viability test was done with rat cortical neurons, because they are more sensitive to changes in their surroundings and do not proliferate. Neurons were cultured in neurobasal (NB) medium on PECM coated glass coverslips inside a 24 well dish. Alexa Fluor was added to half of the medium with a concentration of 50 μg/ml. Before every measurement, the coverslips were put into a petri dish filled with 2 ml NB medium. This way, the dye was removed without the necessity of rinsing. Calcein was added to the fresh medium with a concentration of 1 μg/ml. The sample were put in a incubation chamber for a duration of 15 minutes before measurement. Fluorescent images were taken using two samples cultivated with Alexa Fluor 488 and two sample cultivated in NB medium. Ten randomly chosen images were taken, using a 10$\times$ objective to capture a large amount

of cells in one image.

5.6 Computational Methods and Image Analysis

All data analysis were performed using MATLAB. For the image analysis files were read into MATLAB in the tif format with a color depth of 4096 gray values. MATLAB stores images as two dimensional matrices, where a value is assigned to every (x,y)-position in the image. In order to carry out all necessary mathematical calculations (e.g. image point transformations) with these values, the images were transformed to the double format.

5.6.1 Near Field Effects

Due to near field effects (see appendix B) the reconstruction of the fluorophore distribution $D_{xy}(z)$ using the VA-TIRF theory in section 3.4.3 contained a systematical error. The strategy to eliminate this error was to calculate correction coefficients for every reconstructed height with respect to simulations including the collection efficiency $Q(z)$. For this purpose the equations from section B were implemented into MATLAB. Three cases of staining (transmembrane, intracellular and extracellular) were considered. Transmembrane staining yields a fluorophore distribution in the form of a delta function (see section 3.4.1). Using this boundary condition, the fluorescence intensity $F_{x,y}$ for a membrane distance h_{xy} without collection efficiency is given by

$$\begin{aligned} F_{x,y}(\theta) &= I_{x,y}(0,\theta) \cdot \int_0^\infty D_{x,y}(z) e^{-z/d_p(\theta)} dz \\ &= I_{x,y}(0,\theta) \cdot \int_0^\infty c_{sample} \delta(z - h_{xy}) e^{-z/d_p(\theta)} dz \\ &= I_{x,y}(0,\theta) c_{sample} e^{-h_{xy}/d_p(\theta)} \ . \end{aligned} \tag{5.1}$$

The fluorescence intensity $F^Q_{x,y}$ including the collection efficiency Q is

$$F^Q_{x,y}(\theta) = I_{x,y}(0,\theta) \cdot \int_0^\infty D_{x,y}(z)Q(z)e^{-z/d_p(\theta)}dz$$

$$= I_{x,y}(0,\theta)Q(h_{xy})c_{sample}e^{-h_{xy}/d_p(\theta)} \ . \tag{5.2}$$

Intracellular staining leads to a fluorophore distribution described by a shifted step function. The fluorescence intensities $F_{x,y}$ and $F^Q_{x,y}$ are given by

$$F_{x,y}(\theta) = I_{x,y}(0,\theta) \cdot \int_{h_{xy}}^\infty c_{sample}e^{-z/d_p(\theta)}dz$$

$$= I_{x,y}(0,\theta)c_{sample}d_p e^{-\frac{h_{xy}}{d_p}} \tag{5.3}$$

and

$$F^Q_{x,y}(\theta) = I_{x,y}(0,\theta)c_{sample} \ \cdot \int_{h_{xy}}^\infty Q(z)e^{-z/d_p(\theta)}dz \ . \tag{5.4}$$

If the fluorescent dye resides in the extracellular space, the fluorescence intensities $F_{x,y}$ and $F^Q_{x,y}$ can be expressed as

$$F_{x,y}(\theta) = I_{x,y}(0,\theta) \cdot \int_0^{h_{xy}} c_{sample}e^{-z/d_p(\theta)}dz$$

$$= I_{x,y}(0,\theta)c_{sample} \ d_p \ (1 - e^{-\frac{h_{xy}}{d_p}}) \tag{5.5}$$

and

$$F^Q_{x,y}(\theta) = I_{x,y}(0,\theta)c_{sample} \cdot \int_0^{h_{xy}} Q(z) \left(1 - e^{-z/d_p(\theta)}\right) dz \ . \tag{5.6}$$

The values for cytoplasm and medium staining were calculated using numerical integration (trapezoidal rule). Since values for the collection efficiency were calculated by integration, the integration offered by MATLAB could not be used. The corresponding routine for numerical integration was implemented in MATLAB.

In order to account for near-field effects in our experimental setup, correction coefficients were derived from reconstructing the simulated data $F^{Q}_{y,x}$ with equations fit for $F_{x,y}$.

6 Results and Discussion

6.1 Calculating Correction Coefficients

Correction coefficients for near field effects were calculated using the theory of near-field physics. In figure 6.1, the difference in fluorescence with and without the consideration of the collection efficiency for the different cases of staining can be seen. Compared to the other staining methods, cell-membrane staining seemed to be more sensitive to near field effects. The integration over a range of distances for extra- and intracellular staining seemed to dampen the effect of the collection efficiency, compared to the delta distribution describing cell membrane staining. Since the height profile is gained by fitting the fluorescence intensity data for the ideal case without near-field effects, the different decay constants in figure 6.1 introduced a difference between real and recovered distance. The recovered values represented not only the physical effect in intensity change, but also the ability of the fitting routine to cope with the changed data. For this reason, boundaries for the fit were chosen in a manner that was equivalent for the latter 3-D reconstruction of adhered cells.

The differences for the three staining methods for distances 0 nm $< h_{xy} <$ 250 nm can be seen in figure 6.2. The distance variations were very small for the case of membrane staining. Here, the fitting routine incorporated most of the changes introduced by near-field effects into other fitting parameters. This good adaption was possible because of the delta function model of the cell membrane, which lead to an analytical solution of the fluorescence integral. Extracellular staining introduced the biggest differences between real value and recovered value, because in this case the integration is always done across the region where near-field effects have a great importance. The difference

was an almost constant offset to the real values. Near-field effects lead to an increase of observable intensity in the vicinity of the glass interface. Since for extracellular staining low intensities correspond to small distances, the increase in intensity elevates the recovered distance values with respect to the real distances. Compared to this case, intracellular staining showed a smaller variation in distances. For values under 50 nm, the recovered values were smaller than the real ones, and for values smaller than 15 nm the recovered values reached zero. This behavior is also due to the increase in intensity for small distances. High intensities mean small distances, and thus small recovered values. Since the integration for intracellular staining includes values from the real distance to infinity, the recovered values are closer to the real values for bigger distances, even exceeding the real values due to the normalization step with the extracellular stained solution.

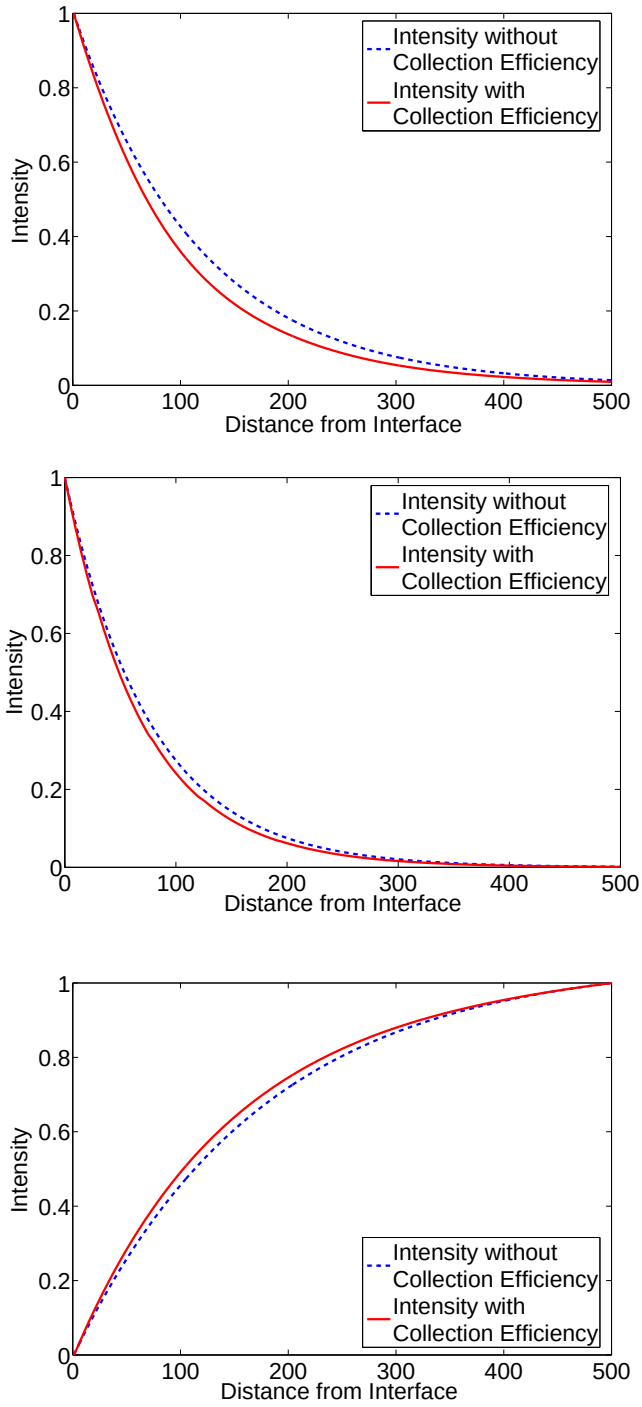

Figure 6.1: The intensities with or without including the collection efficiency differ for (a) membrane, (b) medium, and (c) cytoplasm staining. Values were calculated with the excitation wavelength $\lambda_{ex} = 488$ nm, emission wavelength $\lambda_{em} = 517$ nm, refractive indices $n1 = 1.33/n_3 = 1.518$, angle of incidence $\theta_{inc} = 65°$, and a numerical aperture of $NA = 1.45$.

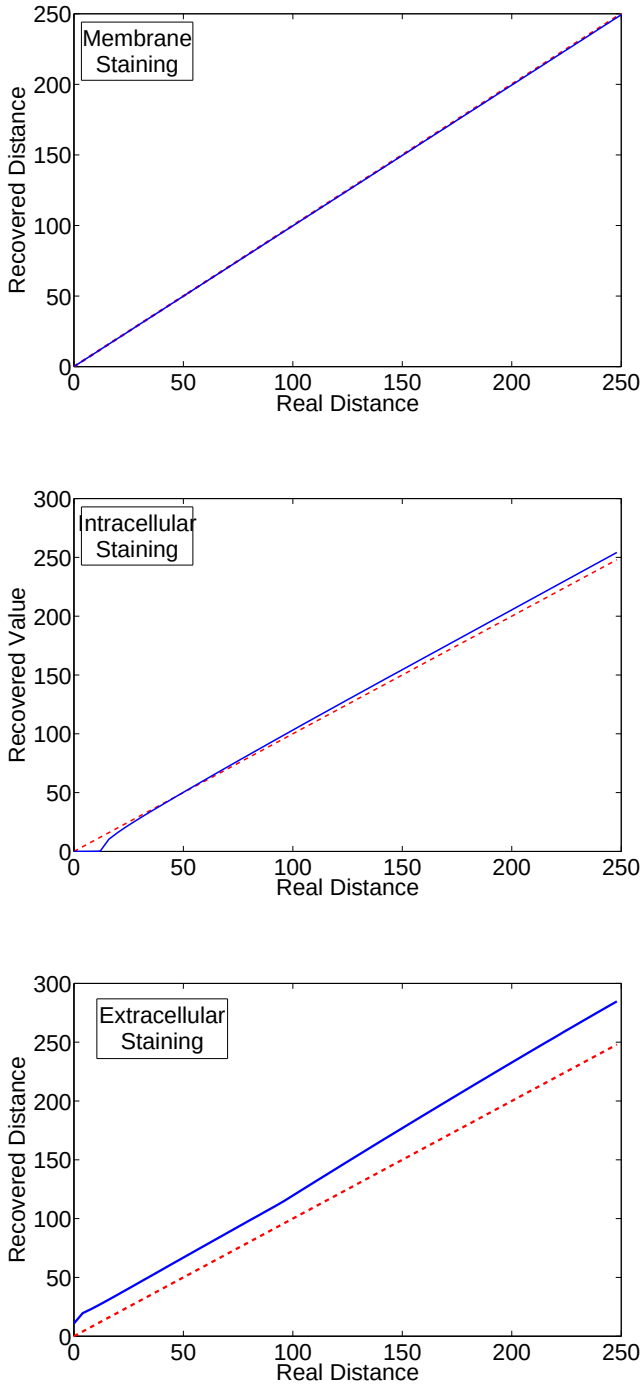

Figure 6.2: Values of recovered height versus the real height for simulated data including near-field effects. The three different cases of staining are shown, cell membrane (a), intracellular (b), and extracellular (c) staining.

6.2 Testing the Theory of VA-TIRF with Simulated Data

In order to characterize the possibility and the limits of the 3D reconstruction software, the reconstruction was tested using a simulated spherical fluorophore distribution. The data was fitted by using the equations established in section 3.4.3. Figure 6.3a shows the result of the simulation. It can be seen that the reconstruction worked well for distances not exceeding an upper limit of 1.7 μm (Fig. 6.3b). This limit was only given by restrictions of the software, because the data used for reconstruction was derived using the exact theory. In order to gain a more realistic insight into the reconstruction process, noise was added to the data. For this purpose high levels of white noise and gaussian blur were used (Fig. 6.4a) to simulate typical noise in microscopy. The reconstruction process was repeated as before. The results show (Fig 6.4b) that the upper limit for successful reconstruction decreased rapidly. But even though high levels of noise were used, the reconstruction was successful up to values of approximatly 380 nm. These results showed that the software used for VA-TIRF measurement suffices to resolve the region of interest of 0-250 nm, even with high levels of noise.

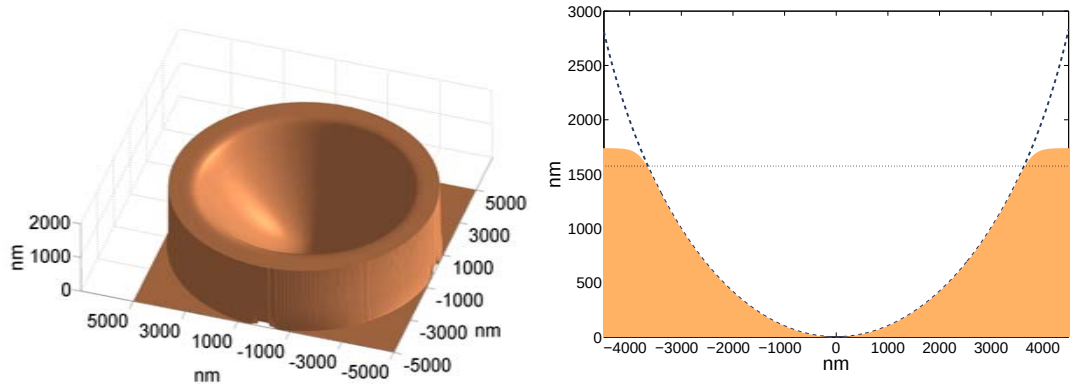

(a) (b)

Figure 6.3: (a) Three dimensional reconstruction of a height profile of a sphere with surface attached fluorescent molecules. (b) Reconstructed height profile as in 6.3a for a center line. A comparison with the sphere (blue dashed line) showed that reconstruction was successful for distance values smaller than approx. 1.7 μm.

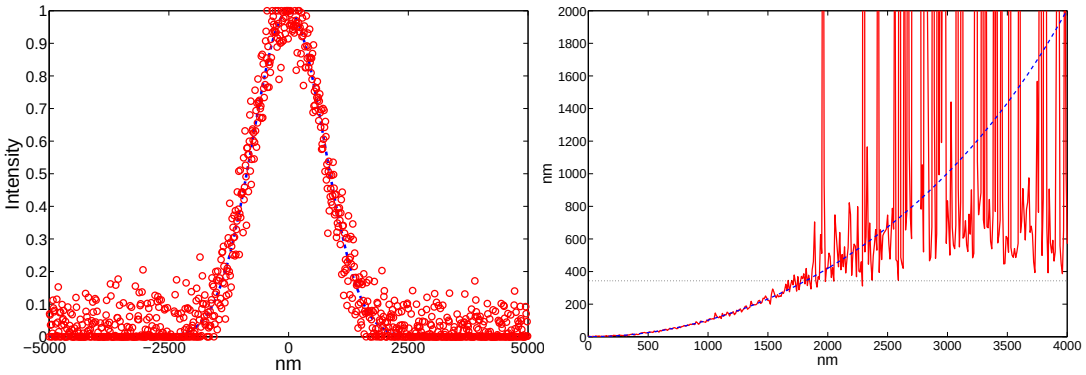

(a) (b)

Figure 6.4: (a) Simulated data with white noise and gaussian blur for a stained sphere surface with an angle of incidence of 65°. (b) Distance reconstruction of noisy data was successful for values smaller than approx. 380nm.

6.3 Model System

In order to evaluate the TIRF setup used in this thesis, basic properties of the setup had to be analyzed. In this section, the image homogeneity, the penetration depth, and the ability to resolve boundaries, given by a lipid bilayer, with TIRAF are discussed. In this work, inhomogeneities in the image intensity were addressed by normalization with a reference image of fluorescent dye in solution (Sec. 6.3.1). The penetration depth of the evanescent field was analyzed with fluorescent labeled microspheres (Sec. 6.3.2), and visualization of lipid bilayers with TIRAF was analyzed with lipid vesicles (Sec. 6.3.3).

6.3.1 Reference Images for VA-TIRF

The VA-TIRF setup used in this thesis, required normalization of the sample image with a reference image. Several approaches exist, which use parts of the sample image where no cell resides to gain the necessary information (e.g. Truskey et al. [1992]). The great amount of inhomogeneities in the image rendered this approach useless in our case. Instead, a reference image of a uniformly stained liquid was used. For this purpose, fluorescent molecules (Alexa Fluor 488 hydrazide) in solution were prepared in a manner that the final refractive index of the stained liquid matched the one of the sample medium. The extend of the inhomogeneities can be seen in Figure 6.5. These inhomogeneities form as a combination of field variations concerning the excitation and the image forming process. Variations in the evanescent field at the interface with intensity $I_{xy}(0, \theta)$ lead to non-uniform illumination. Most importantly, the variations in the evanescent field arise due to the beam profile of the laser and scattering effects inside the optical train of the microscope. Additionally, image formation introduces certain errors to the image. The use of laser light leads to interference patterns. These patterns were only visualized when the objective was focused on the glass-liquid interface, suggesting that the main reason for interference patterns are backscattering effects between the interface and other interfaces in the optical path, like the glass-oil

interface, oil-objective lens interface, or the surface of the dichroic mirror. All these effects should remain constant for different samples and can thus be eliminated by normalization with the reference image. Other effects like air bubbles inside the immersion oil layer, glass roughness of the coverslips used for measurement or small variations in the focus should lead to differences that can not be excluded by the reference image. In order to measure the severeness of these effects, reference images were taken under different incident angles. Ten images at different areas of three reference samples were taken under the same imaging conditions. The total collected intensities were compared for the different angles.

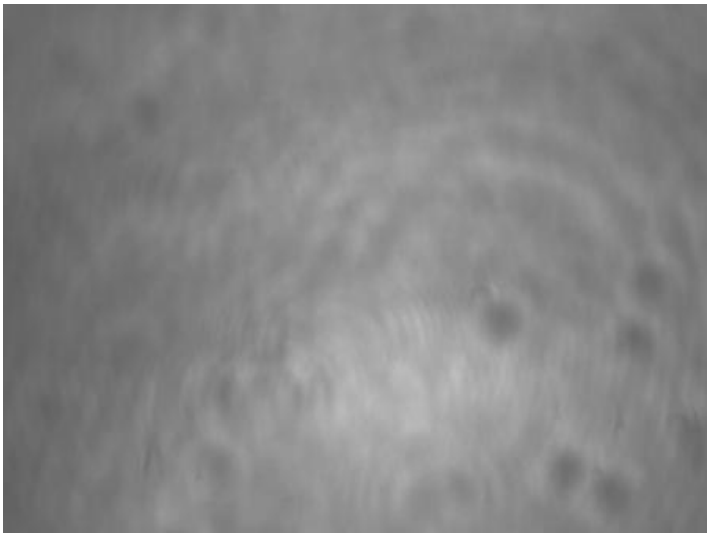

Figure 6.5: Typical reference image obtained using Alexa Fluor 488 in solution. Uneven illumination and interference patterns distort the image to a high degree.

As can be seen in figure 6.6, the decay of the intensity did not follow the exponential decay predicted by the theory. Standard errors for intensities at the same angle of incidence varied between 1% and 3%. Larger errors for big angles can be explained by a higher probability that the laser beam gets distorted by small air bubbles or other inhomogeneities in the immersion oil for bigger angles. The slightly increasing errors for smaller angles were due to growing errors of the penetration depth for smaller angles of incidence (Tab. 4.1). Thus, the best results for VA-TIRF measurements can be expected for angles between 66° and 71°, restricting the angle domain for analysis to a variation of 5°.

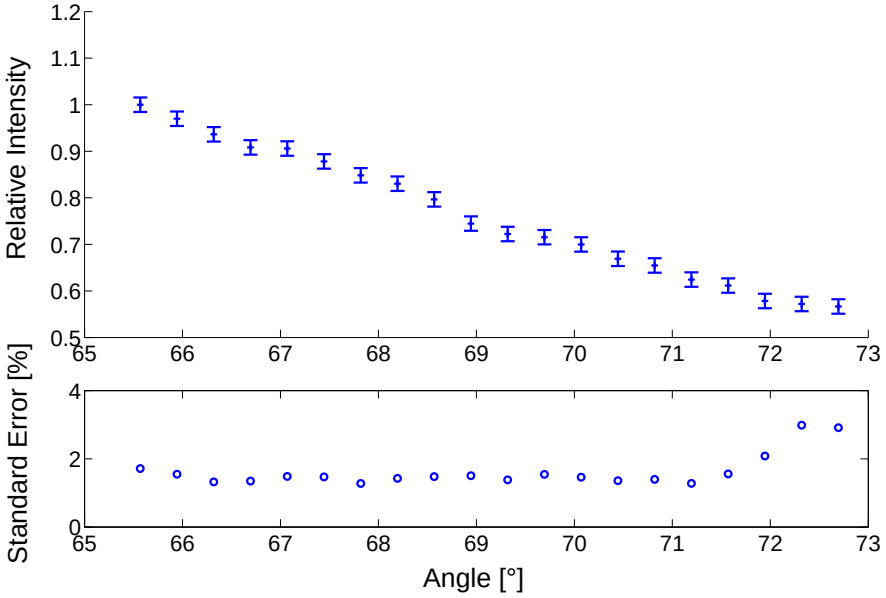

Figure 6.6: Evaluation of reference images at different angles of incidence.

6.3.2 Measuring the Penetration Depth with Microspheres

Microspheres (beads) can be used to measure the penetration depth of evanescent fields. For the measurement surface labeled silicate microspheres (Kisker, Germany) with a diameter of 10 μm and a low refractive index were used. Silicate microspheres have a refractive index of approximately 1.37, which can be matched by the help of the surrounding liquid in different ways. For this analysis, the matching was done using 30% DMSO in water, which showed good results in matching silicate substances before [Olveczky et al., 1997]. Refractive index matching is an essentiel part of this measurement, because differences in refractive index between bead and medium create an effect called whispering gallery modes [Matsko and Ilchenko, 2006]. Whispering gallery modes are strongly confined, sustained electromagnetic modes inside dielectric spheres, which are generated by total internal reflection. Although distributed by the supplier as silicate microspheres with a refractive index of 1.37, our beads showed diffraction under dark field illumination, suggesting that the refractive index was different from the advertized value. The refractive index was measured using equal concentrations of

smaller fluorescent beads (1 μm) in solutions with different refractive indices. For the regulation of the refractive index, glycerin dissolved in water was used and the refractive index was determined using an Abbe refractometer. To circumvent interference from the fluorescent dye (Ex/Em: 485/510), the light absorption was measured at 700nm using an absorption spectrometer. If the solution matches the inner refractive index of the beads, the absorption of the sample should be minimum. The results (Fig. 6.8) showed that the refractive index of the beads was 1.44. Unfortuneatly, this value was too high to use the spheres for acurate calibration purposes, because TIR only appears for incident angles exceeding 72°, which is too close to the limits of the microscope for VA-TIRF microscopy. Nevertheless, measurements using the assumption of a low refractive index of 1.37 showed promising results for future measurements using actual low refractive index beads.

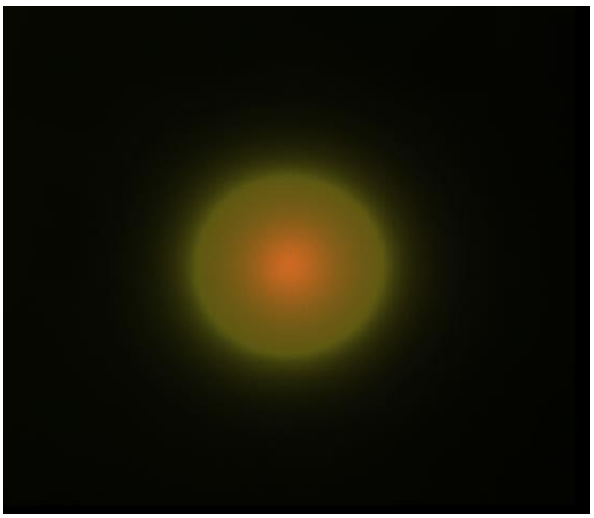

Figure 6.7: False-color image overlay of TIRF and Epi-fluorescence of a fluorescent microsphere. The TIRF image was focused on the coverslip interface, whereas Epi-fluorescence was focused near the sphere's equator.

The technique of directly visualizing the penetration depth with microspheres was first proposed by Mattheyses and Axelrod [2006]. Giant microspheres are settled onto a glass surface and the sphere's footprint is recorded. Because of the known geometry of the sphere (Fig. 6.9), a z-position can be assigned to every pixel in the xy-plane of

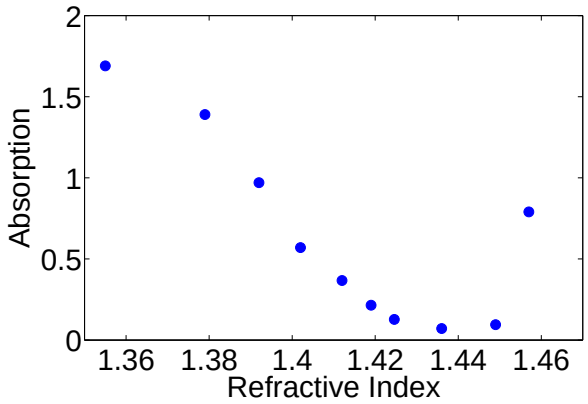

Figure 6.8: The absorption minimum of the silicate microspheres is at a refractive index of 1.44.

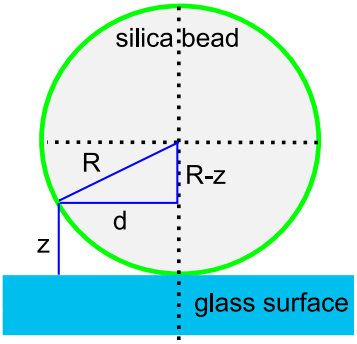

Figure 6.9: Schematical drawing of the geometrical relations for a microsphere onto a glass interface

the image. The z-position is given by the radius R and the lateral distance d from the center of the sphere

$$z = R - \sqrt{R^2 - d^2} \ . \tag{6.1}$$

Two corrections need to be done, concerning the pixel size of the image and the curvature of the bead. The pixel character of the image leads to a displacement of the intensity information. This effect can be corrected, by assigning a radial bin to every pixel position $(x-0.5, y-0.5)$, where x and y are the positions of the upper left corner of the pixel. Another implication of the pixel size is the effect it has on fluorescence emission from a curved surface. For pixels close to the center, the integrated intensity

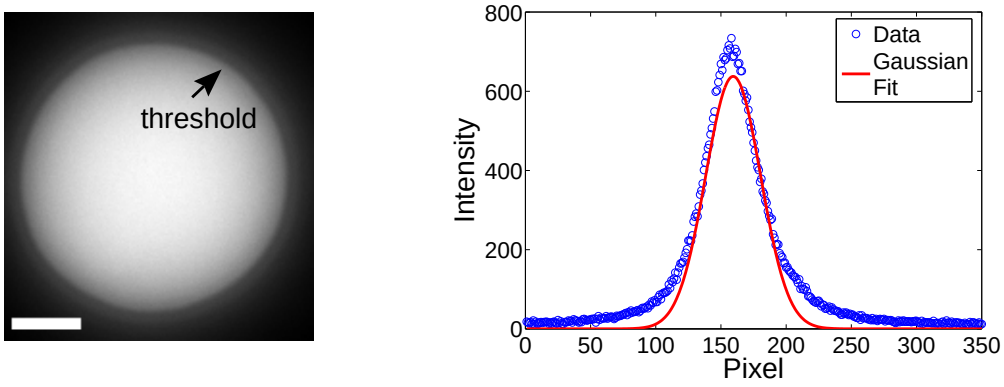

(a) (b)

Figure 6.10: (a) The radius of the sphere can be measured by counting the amount of pixels exceeding a threshold value in epi-illumination (The bar in the figure is 2 μm). (b) The center of the sphere can be determined with a gaussian fit

I' includes fewer z values than for pixels far away from the center. This effect can be accounted for by the formula

$$I = I' \cos(\arcsin(d/R)) \ . \tag{6.2}$$

The procedure can be used to assign a z-distance to every measured intensity. For the calculation, the radius R and the center of gravity M needed to be measured. The radius was measured using epi-fluorescence focused on the bead's equator. The number of pixels exceeding a threshold value were counted, by which means the radius was calculated (Fig. 6.10a). The center of gravity was determined applying a gaussian fit to the data acquired under TIRF-illumination. For this purpose, the center was first approximated using the highest intensity in the image. A series of 10 gaussian fits in x and y direction around this center was used to find the actual center of gravity with an accuracy of ± 1 pixel.

The intensity data was then plotted over the z-distance (Fig. 6.11a). According to equation (3.14), an exponential fit to this data yields the penetration depth. When using prism-based TIRF setup, the results with a single exponential fit suffice to gain the correct information [Loerke, 2004]. A through-the-objective TIRF however, makes

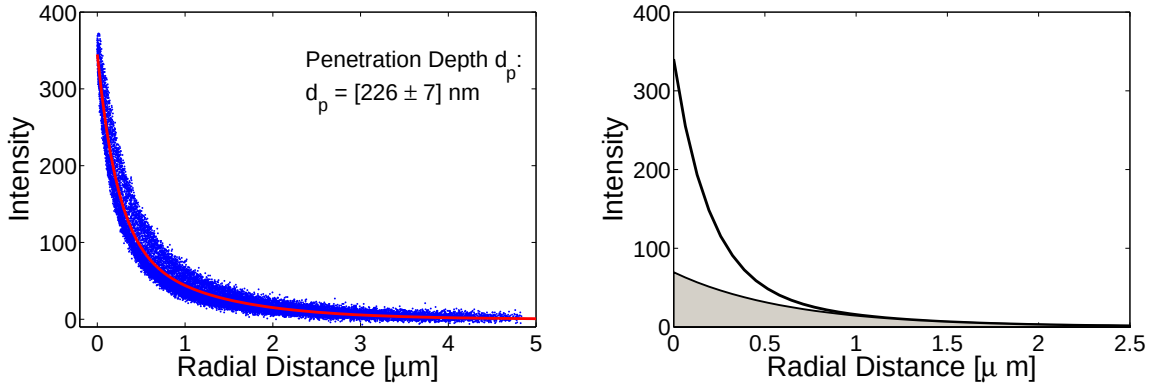

(a) (b)

Figure 6.11: (a) Intensity values plotted over the distance from the interface show the decay of the evanescent field. The values were obtained using an angle of incidence of 67.3° and are part of a series of 20 different angles. A double exponential fit yields a penetration depth d_p of 226 nm. Figure (b) shows the results of the double exponential fit plotted together with the slow decaying scatter portion of the fit (gray filled). It can be seen that for z-distances higher than approx. 1.5μm, the measured signal is only due to stray light.

it necessary to include a second exponential function to compensate scattering effects [Mattheyses and Axelrod, 2006]. The double exponential fit was done with 10 different spheres, each illuminated under 20 different angles of incidence. The obtained values show the decay of the penetration depth with increasing angles of incidence (Fig. 6.12). As expected, the measured values vary from the theoretical predicted values. The measured values for the penetration depth are higher than the values derived from the angle of incidence, which is due to additional stray light inside the spheres. This stray light is caused by the refractive index difference between sphere and surrounding liquid.

6.3.3 Vesicle Measurements

Vesicles, or liposomes are artificially produced, spherical lipid bilayers (Appendix C). Since vesicles are one of the simplest models of a cell membrane, they serve as a model system for several applications like for instance cell adhesion [Sackmann and Bruinsma, 2002]. The vesicles contained a sucrose solution (dimeric molecule) and were observed in a glucose solution (monomeric molecule). The dimer filled vesicles descent fast in the monomer solution. Since vesicle are destroyed by the contact with pure

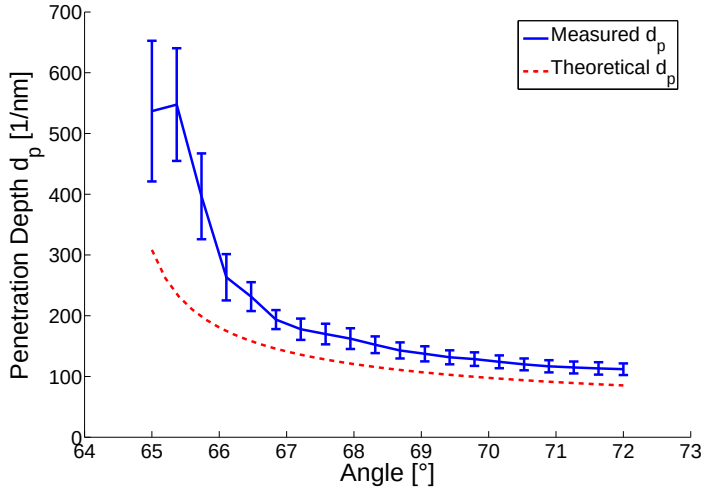

Figure 6.12: Different measured penetration depths over the angle of incidence. The values are bigger than the values calculated from the angle of incidence.

glass, the coverslips were coated for two minutes in Bovine Serum Albumin (BSA). For observation of the vesicles, 50 μg/ml Alexa Fluor 488 hydrozide (Section 5.4) was added to the glucose solution. Vesicles were observed under normal bright field illumination and under TIR illumination (incident angle 68°).

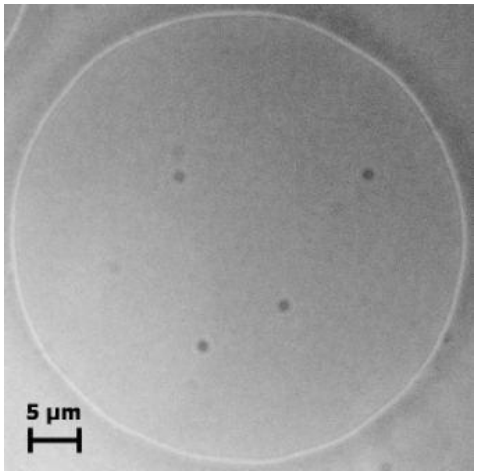

Figure 6.13: Bright field image of a giant vesicle with a diameter of 46μm. Brightness and contrast were adjusted to visualize the vesicle, because it was almost visible under brightfield illumination.

The TIRAF images of a vesicle with a diameter of 46 μm (Fig. 6.14) showed a contact area with an approximate diameter of 15 μm (Fig. 6.13). The contact region diameter was about one third of the diameter of the whole vesicle. Fluctuations of the vesicle's membrane could be resolved in the TIRAF images. These fluctuations were not visible under brightfield or phase contrast microscopy and have been reported before for comparable vesicles by FLIC microscopy [Zeck and Fromherz, 2003]. In this study a mean distances of the adhesive area of vesicles on a BSA coated surface of 50 nm was reported. If the measured vesicles are assumed to exhibit comparable distances, the measurements showed that extracellular staining can be used to visualize contact areas between a glass substrate and a lipid bilayer with a high axial resolution.

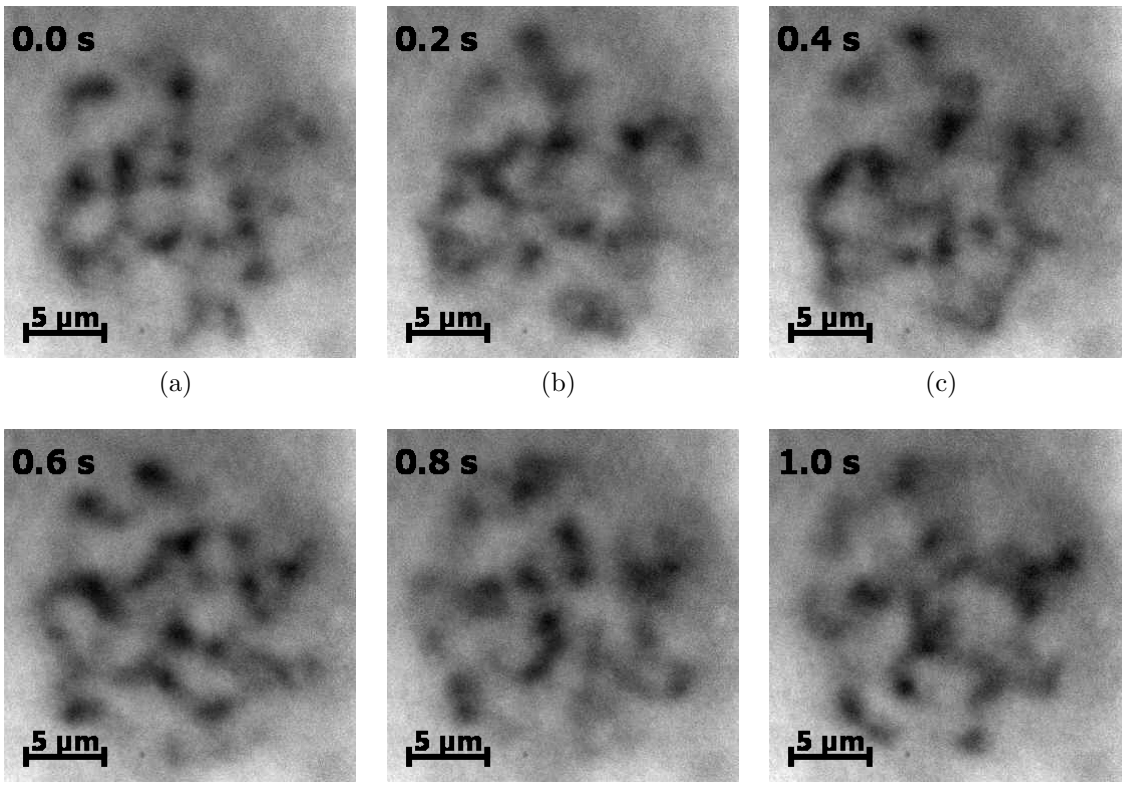

(a) (b) (c)

(d) (e) (f)

Figure 6.14: Adhesion areas (dark) of the same giant vesicle as in figure 6.13 under TIRAF. Only a small portion of the vesicle was visible. The morphological vibrations of the vesicle on the glass substrate are shown on the images (the images were taken with 200 ms intervals).

6.4 Characterization of Fluorescent Dyes

Since the fluorescent dyes used in fluorescence microscopy were an essential part of the measurement, two major possible problems related to the dyes were analyzed. Alexa Fluor 488 hydrazide, which stains the extracellular medium may harm the cells. Therefore, the viability of rat cortical neurons cultured in this fluorescent dye was determined (Sec. 6.4.1). Another problem is photobleaching of the fluorescence dyes. The effect of photobleaching was measured for the case of intra- and extracellular staining (Sec. 6.4.2).

6.4.1 Viability of neurons cultured with Alexa Fluor 488 hydrazide

Viability measurements were performed for 3 days, which is the typical period neurons survive without media exchange. In this period the cell viability did not decrease significantly (Fig. 6.15). This indicated that the influence of the extracellular staining using the Alexa Fluor 488 hydrazide dye to the cell viability was low. Furthermore it was shown that this dye is perfectly suited for longterm measurements concerning the adhesive area of cells. For the analysis, every fluorescent cell was counted. The effect of internalized Alexa Fluor 488 hydrazide (e.g. by endocythosis) was measured with fluorescent images before and after the addition of calcein. Approximatly 5% of the fluorescent cells internalized enough Alexa Fluor 488 hydrazide that they were visible without calcein. Since dead cells loose their cell membrane integrity, Alexa Fluor 488 hydrazide should diffuse out of these cells. Thus, the error introduced by just adding calcein to the medium includes only cells that died shortly before the measurement (e.g. caused by mechanical stress from moving the coverslip out of the medium). Therefore number of cells cultured with Alexa Fluor 488 hydrazide was expected to be slightly higher than for the cells cultured without it.

The variations in cell number can be caused by several mechanisms. One reason for the variation may be differences in the initial cell density, caused by differences in protein coating and the plating density of cells on the coverslips. Another reason

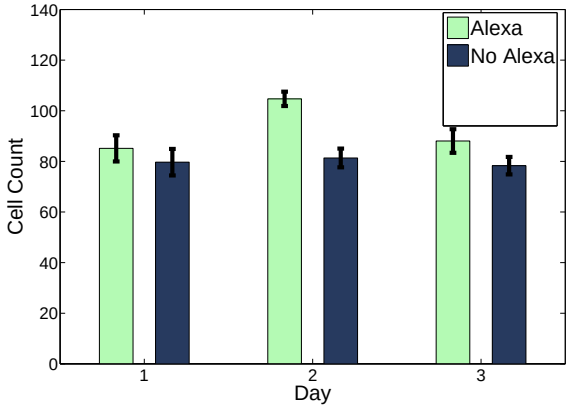

Figure 6.15: Cell counts for an area of 1.42 mm^2 for rat cortical neurons cultivated in NB medium with and without the addition of Alexa Fluor 488 hydrazide. Each cell count is the mean numbers of cells counted in 20 images and the error bars represent the standard error.

could be the movement of the coverslip across two tension barriers (medium-air and air-medium barrier), which may cause some cells to loosen or die. In contrast to rat cortical neurons glia cells, which are always present in our neuronal cell culture, are proliferating. Thus, there exists the possibility that a decrease in neuronal cell number is compensated by the reproduction of glia cells. The slightly increased number of cells cultivated in Alexa Fluor 488 hydrazide is due to internalized dye in cells that died shortly before the addition of calcein. The highest cell density was measured for the second day, which should be further investigated in future experiments. This measurement was supposed to give a qualitative estimate of the influence of Alexa Fluor 488 hydrazide on cells. In the future, the analysis can be enhanced by using higher amounts of cells analyzed by flow cytometry and an additional marker for cell death.

6.4.2 Photobleaching

The effect of photobleaching was measured according to section 5.5.1. Laser intensity was chosen in way that no visible photo damage to the cells occurred. The effect of high intensity laser light on cells can be seen in figure 6.16. In the experiment, TIRAF images were taken with high laser intensities. After 2 minutes of illumination, the adhesive structure was no longer visible, because photo induced damage to the cell membrane lead to bulging of the cell membrane (blebbing) [Weinstein et al., 1997] and to a flow of cytoplasma into the extracellular medium (dark regions). Laser intensity was set to a point where there was no blebbing visible after 2 minutes of exposure to the laser light. The measurements were done for a period of 50 seconds of continuous illumination of the cell.

For the extracellular staining technique, photo bleaching was measured for the mean values of the extracellular medium (100×100 pixel) and a close contact (3×3 pixel). A close contact was chosen, because it showed the highest rates in photobleaching due to its close proximity to the glass surface. For the extracellular medium, no drop in intensity was measured (Fig. 6.17a). On the other hand, the close contact showed an increase in intensity (Fig. 6.17b) of approximately 5%, indicating that after 50 seconds of continous illumination some photo damage was induced to the cell. In case of intracellular staining with calcein (Fig. 6.17c), the loss in measured intensity was approximately 15%. Thus, the effect of photobleaching was much more severe for this staining method. The results of these measurements showed that the effect of photobleaching was smaller for extracellular staining with Alexa Fluor 488 hydrazide than for intracellular staining with Calcein-AM. The Alexa Fluor 488 hydrazide dye in solution showed no sign of photobleaching due to diffusion of intact dye molecules from other parts of the sample. Although small, photobleaching due to photo damage to the cell membrane was visible for areas of close contact. The otherwise cell membrane impermeable fluorescent molecule was entering the cytoplasm through the damaged areas and generated a signal inside the cell, which disturbed the dark footprint measured with TIRAF. This effect should also play a role in intracellular staining, where the

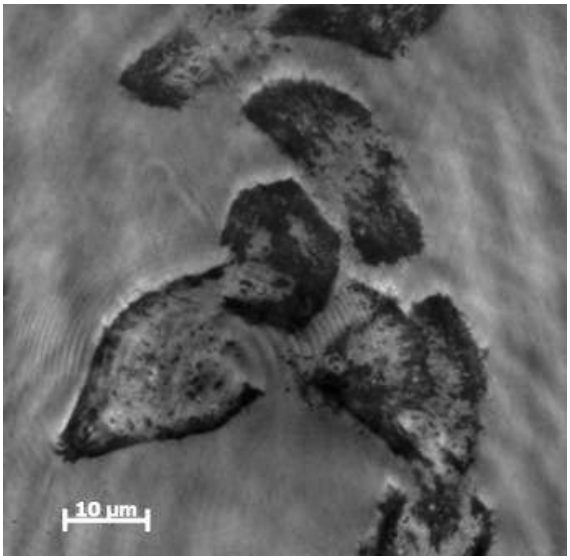

(a)

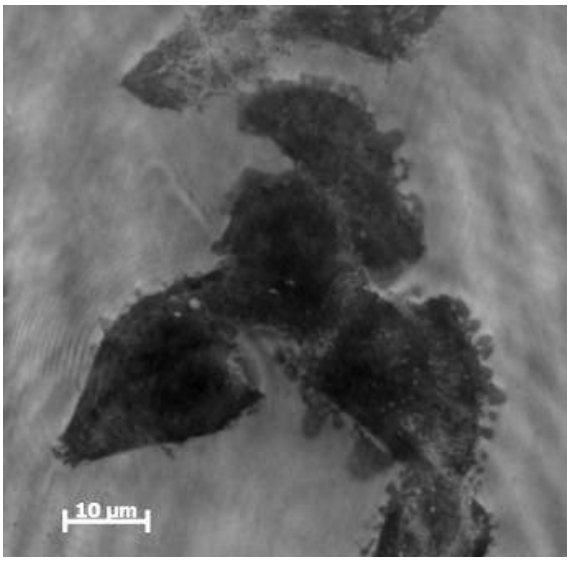

(b)

Figure 6.16: Light induced cell membrane damage leads to an irregular bulging of cell membrane and secretion of cytoplasma. The images were taken with the technique of extracellular staining. Figure (b) shows the cells in figure (a) after 2 minutes of high intensity laser illumination.

cell membrane impermeable fluorescent calcein could eventually exit the cytoplasma through the damaged areas. Additionally, the limited amount of fluorescent molecules should lead to observable conventional photo bleaching.

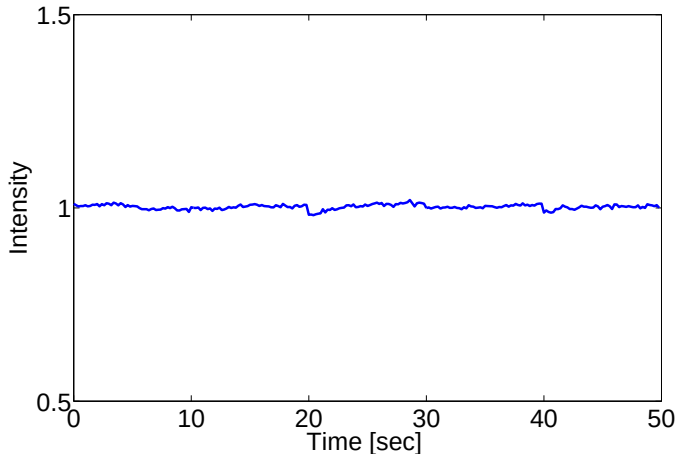

(a)

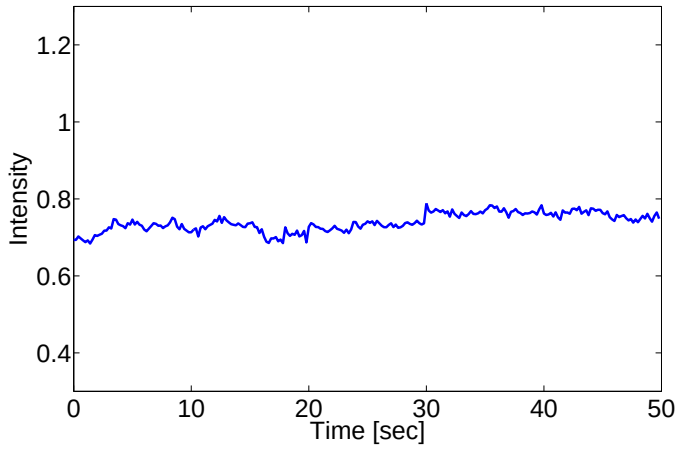

(b)

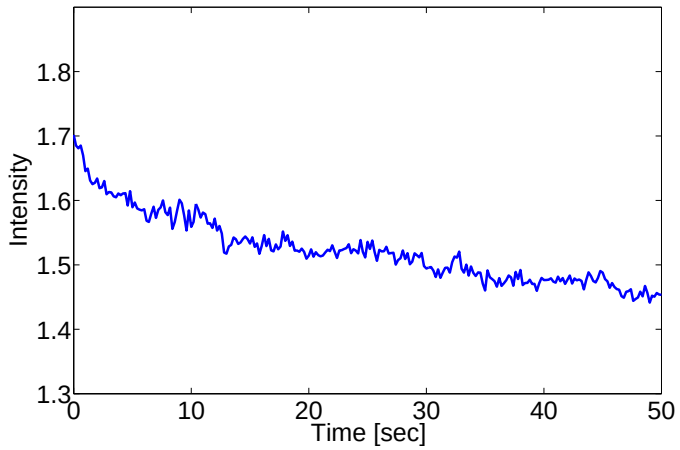

(c)

Figure 6.17: The effect of photobleaching for extracellular staining with Alexa Fluor 488 hydrazide and intracellular staining with Calcein-AM. The effect of photobleaching was stronger for intracellular staining (c) than for extracellular staining (b). For the extracellular dye, no photobleaching in areas without any cell (a) was observed.

6.5 TIRF Measurements of Adhesion Profile of Living Cells

In the following section different types of TIRF measurements were used to optimize information gained about the cell substratum interface. First, the TIRAF technique was verified by analyzing focal adhesions (Sec. 6.5.1), after which TIRAF and TIRF was used to describe the interface qualitatively (Sec. 6.5.2). In order to address the influence of different errors, a quantitative analysis with image histograms was established (Sec. 6.5.3). This analytical method was then used to characterize the cell substratum interface on different protein coated surfaces 6.5.4. However, this techniques lacks the ability to assign absolute distance values. Therefore, VA-TIRF was used in section 6.5.5 for more accurate measurements.

6.5.1 Analyzing Focal Adhesions

Stray light effects lead to a distortion of the TIRF image. Furthermore, the cell itself perturbs the evanescent field through refractive index variations inside its subcellular components. For this reason a validation of the TIRF measurements on living cells was necessary. Focal adhesions are strengthened connections between cell receptors and ECM ligands. The distance of the cell membrane to glass in focal adhesion depends on the thickness and conformation of the protein coating and on the length of integrin receptors. Reported distances between glass substrate and cell membrane in the vicinity of focal adhesions can vary from 10 nm [Alberts et al., 2004] to 90 nm [Iwanaga et al., 2001]. Since focal adhesion sites indicate a closer contact of the cell to the substrate than average, these structures were used to evaluate the results for extracellular staining.

6.5.1.1 TIRF Measurements of Vinculin Distributions

A comparison of GFP-vinculin transfected cells for bright field, epi-fluorescence and TIRF illumination is shown in figure 6.19. Since TIRF microscopy only excites fluo-

rescent molecules close to the substrate surface, it is perfectly suited to enhance image contrast by reducing background fluorescence.

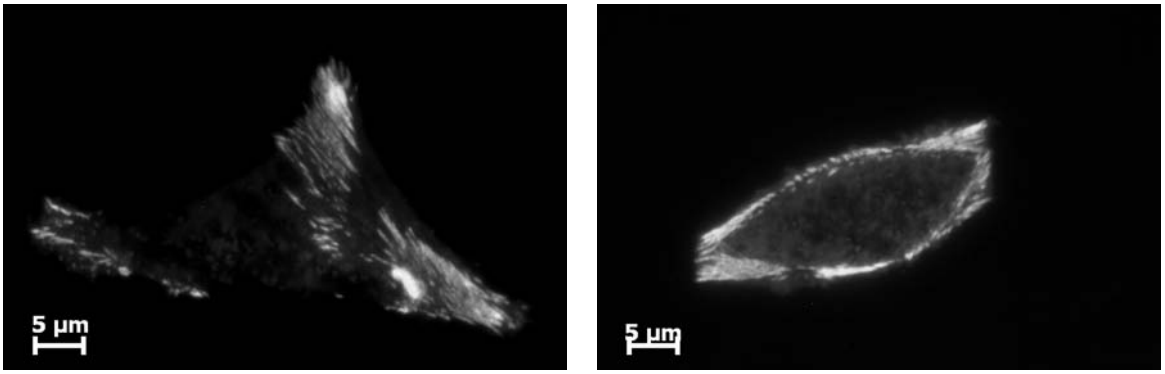

(a) (b)

Figure 6.18: Examples for focal adhesion structures of HEK293 cells cultured on glass. Areas of focal adhesion were concentrated at the edges of the cells. Typical diameters of focal adhesion strands varied between $200 - 300$ nm, whereas the length could reach several micrometers.

TIRF images of the vinculin distributions revealed that focal adhesions are normally concentrated at the outer boundaries of HEK293 cells adhered on a glass substrate. This result is expected, because focal adhesions are known to be generated at regions exhibiting higher tension. Two main structures are visible for focal adhesions: a strand like and a point like structure. The structures showed diameters between $200 - 300$ nm, but the length of the strands could be several micrometers. Since the lateral resolution of our microscope was only 205 nm, small focal adhesions could still show smaller diameters than observed by our setup.

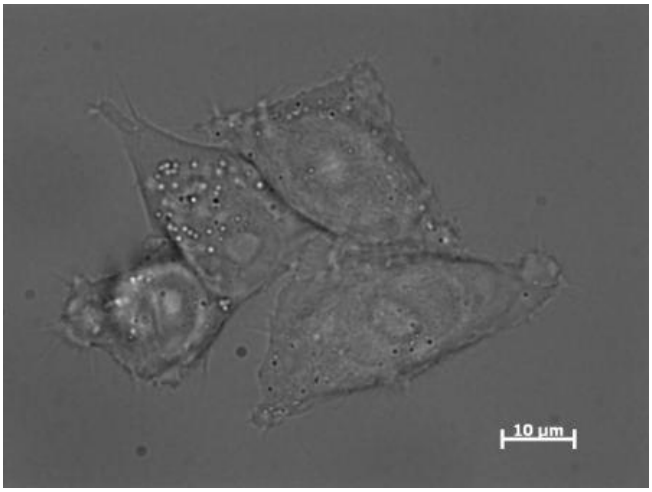

(a)

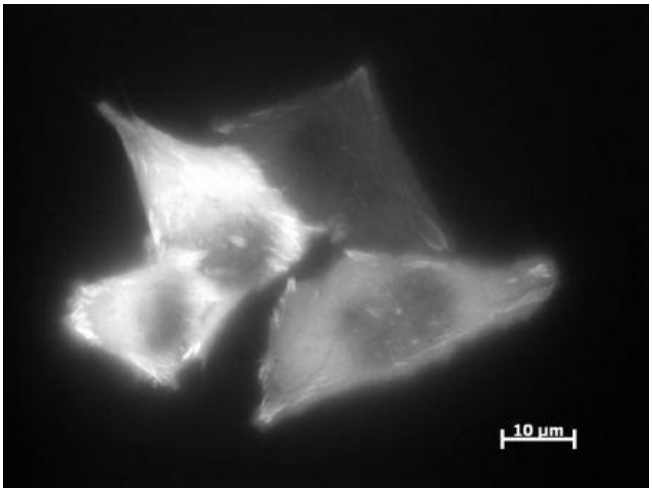

(b)

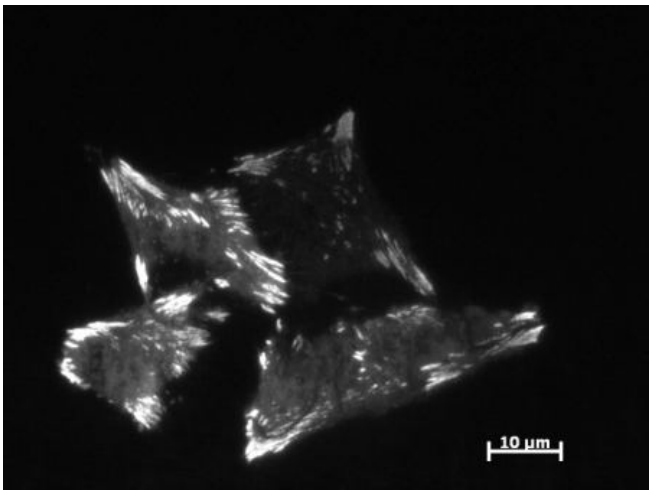

(c)

Figure 6.19: Bright field image (a) of HEK293 cells transfected with GFP-labeled vinculin. The fluorescence image (b) lacked the contrast to distinguish focal adhesions in detail. On the TIRF microscopy image (c) focal adhesion was clearly visible. The residual fluorescence signal was due to overexpression of vinculin in the cell.

6.5.1.2 Evaluation of TIRAF Measurements with Vinculin Distributions

For the evaluation of the TIRAF technique, Alexa Fluor 488 hydrazide was added to the medium of the cells after measuring focal adhesions. In order to keep cell damage and change in cell morphology low, images were taken right after adding the dye. Since the fluorescent signal of the GFP labeled vinculin was very low (weak signal with 2 seconds exposure time) compared to the extracellular staining (strong signal with 150 ms exposure time), the error from not considering the fluorescent signal of the GFP was negligible in the TIRAF image.

TIRAF images could reproduce structures of close contact indicated by the presence of vinculin (Fig. 6.20). This means that the sensitivity of the TIRAF microscopy was high enough to measure differences between close contacts and cell membrane parts that were not directly adhered to the surface. Since typical cell/substrate separation distances range from 10 to 100 nm (see Tab. 6.3), this result suggests an axial resolution in the order of several nanometers for our system. This high axial resolution is only a few percent of the 607 nm given by the Abbe limit. Although close contacts can be visualized, the contrast differed for some regions of focal adhesion. One advantage of the TIRAF measurement is that focal contacts, which were not strongly connected to the cytoskeleton by vinculin, were also detectable.
In order to quantify the reproducibility of focal adhesions with TIRAF, it was necessary to see if there was a general intensity drop in the TIRAF image at areas indicated as focal adhesions by the presence of vinculin. This analysis was done by using image histograms which give statistical data about the distribution of image intensities. For this purpose, vinculin images were taken as a template to define a region of interest for the histogram of the normalized cell image. The normalization was done with a reference image, setting the intensity value for infinite distances (I_{inf}) to the glass interface to 1. This histogram was compared with a histogram of the whole cell.

The histograms (Fig. 6.21) showed that the intensity peaks were shifted for regions defined as focal adhesions by vinculin (Fig. 6.21a) with respect to the whole cell (Fig. 6.21b). The lowest value obtained in the image was an intensity drop to 0.57. Both

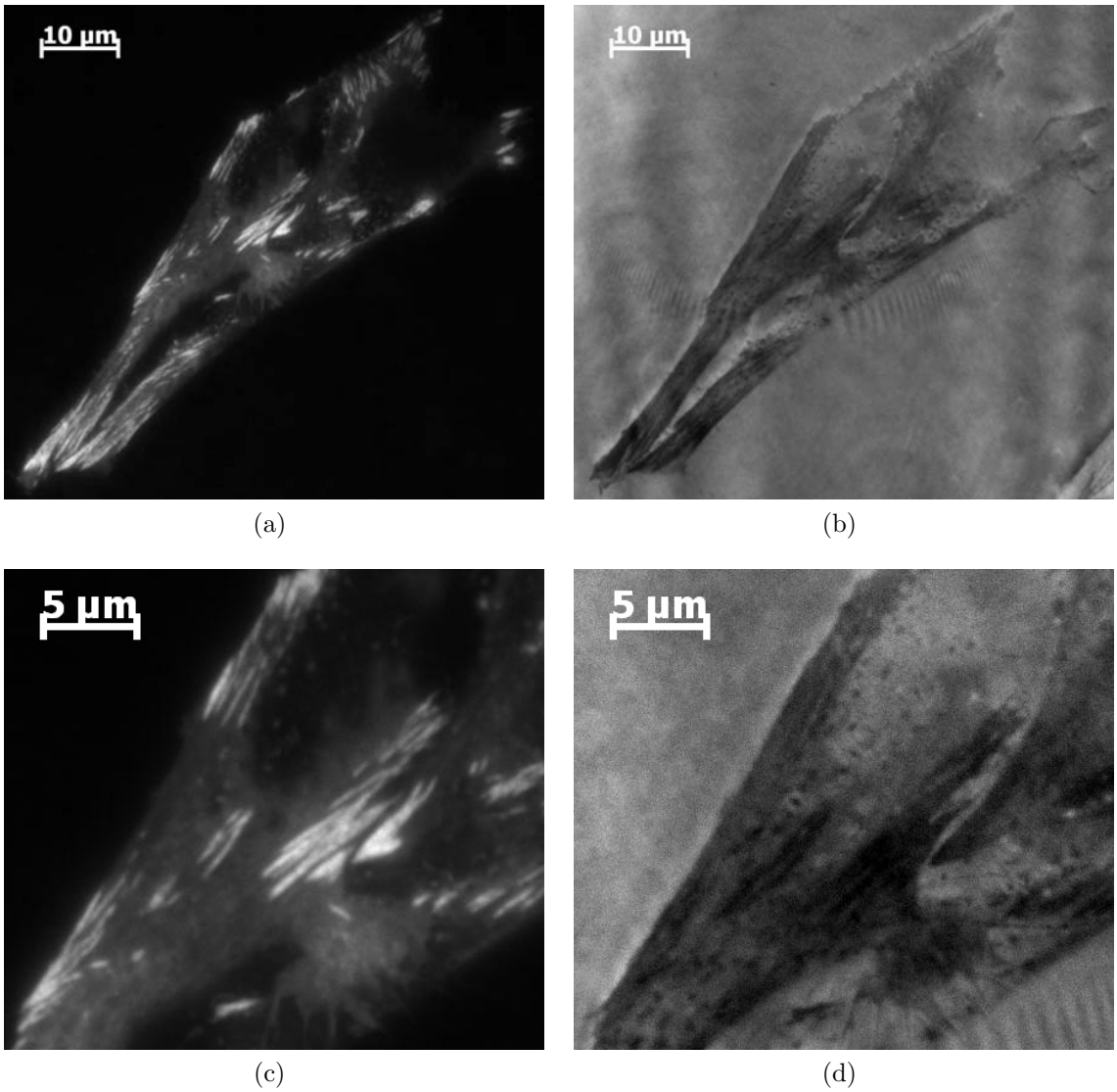

Figure 6.20: TIRF microscopy images of cells with GFP-labeled vinculin (a, c) and TIRAF images of the same cells with extracellular Alexa Fluor 488 hydrazide staining normalized by a reference image (b, d). The fringing in figure 6.20b was typical for images taken with small air bubbles present in the immersion oil. Figures (c) and (d) show a magnification of the center regions. Focal adhesions indicated by the presence of vinculin can be seen in the TIRAF images.

histograms were fitted using a double gaussian distribution, which revealed peaks at 0.69 and 0.77 for the focal adhesions, and 0.76 and 0.83 for the whole cell. According to section 3.4.2, approximate distances can be assigned to these values. If an offset of 15 nm is set to a value of 0.57, which is the lowest obtained value, distances can be assigned to the fitted values (Tab. 6.1).

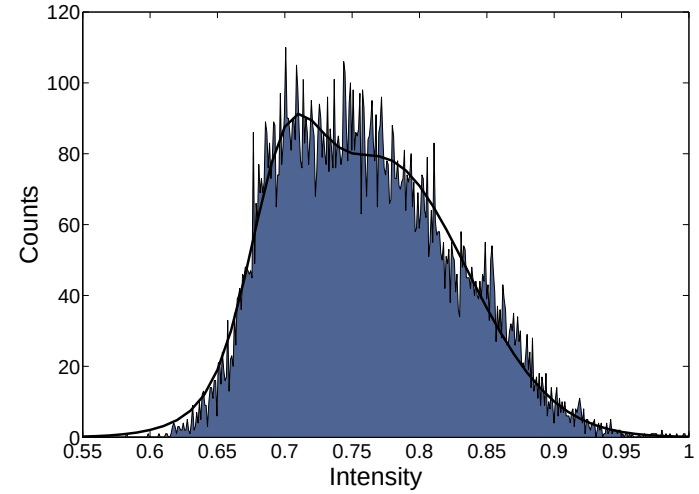

(a)

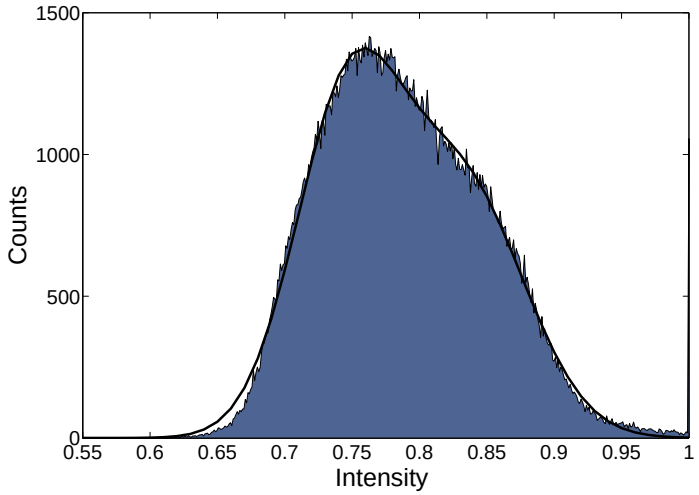

(b)

Figure 6.21: Histogram of a normalized image of a HEK293 cell for regions of focal adhesion indicated by the presence of vinculin (a) and for the whole cell (b). The image was taken with an angle of incidence of 67.4°. The data was fitted using a double gaussian distribution.

The four peaks in the histogram represent three different distances exhibited by the cell. The closest distance of 32 nm represented the mean distance of focal adhesions. The second distance of approx. 54 nm, which was found in both histograms, described regions of the cell close to focal adhesions or close contacts and the third distance of 76 nm showed the value for membrane at some distance to focal adhesions. These values are comparable to values previously reported in literature. Chen and Singer [1982] classified the adhesion of cells into (i) focal adhesions with 10–20 nm separation

	Peak	Relative Intensity drop [%]	Distance from Interface [nm]
FA	0.69	69	32
All	0.76	55	53
FA	0.77	54	54
All	0.83	42	76

Table 6.1: Results of two histograms of the same HEK293 cell adhered to glass for areas of focal adhesion (FA) and the whole cell (All). The drop in intensity for the area between the offset 0.57 and the outside intensity revealed three mean positions of the cell membrane. Close contacts (32 nm), well adhered (approx. 54 nm) and poorly (76 nm) adhered parts of the membrane can be distinguished.

distance, (ii) close contacts with 30–50 nm distance, and (iii) ECM contacts with distances exceeding 50 nm. It can be seen from these values that an TIRAF image histogram over a whole cell does not show an accumulation of distance values for focal adhesions but for close contacts and ECM contacts. Because of the limited elasticity of the cell membrane, areas close to focal adhesions are close contacts. Therefore, the peak for the close contacts was seen in both histograms.

6.5.2 Qualitative Characterization of the Adhesion Region by TIRF Microscopy

6.5.2.1 Extracellular Staining (TIRAF)

The ability to visualize the adhesive region of cells can be used to get a first impression about the cell substratum profile. For this purpose, HEK293 cells were cultured on PLL, Fibronectin, Con-A and Laminin, rat cortical neurons on PECM, and cricket neurons on Con-A. Some examples of the adhesive profile of HEK293 cells are shown in figure 6.22. HEK293 cells showed a vast variety of differences in cell adhesion. The differences cover the whole range from poorly adhered cells with huge unadhered regions to tight adherence over the whole cell body. The differences from cell to cell observed for one protein coating, even on the same petri dish, seemed to be bigger than the differences between the differently coated surfaces. This result suggests that any kind of quantitative analysis of the protein coatings, has to include statistical data over a variety of different cells. The tendency of HEK293 cells to show close adherence at the edges of the cell observed by the vinculin measurements was also confirmed by the TIRAF measurements (Fig 6.22). Rat cortical neurons on the other hand showed a much more homogeneous adhesion (Fig. 6.23). The cells adhered tightly with areas of huge distance to the glass interface and looked very different from the HEK293 cells. The tendency to show tight adherence on the boundaries of the cells was not observed. Small separation distances could be seen over the whole cell body with circular regions of upwards bulging of the cell membrane. For cricket neurons, an adhesion behavior similar to that of rat cortical neurons was observed, when adhered to the surface, however the average cell substratum distances seemed to be larger (Fig 6.24a). Additionally, for a large amount of neurons, no attachment of the cell body itself was measured with TIRAF (Fig. 6.24b). The results of this study showed that the cell body of the non-adhered cells was separated from the glass surface by at least 300 nm. Bright field images suggested that this floating character of the neuron might be typical for large, ball-shaped cricket neurons.

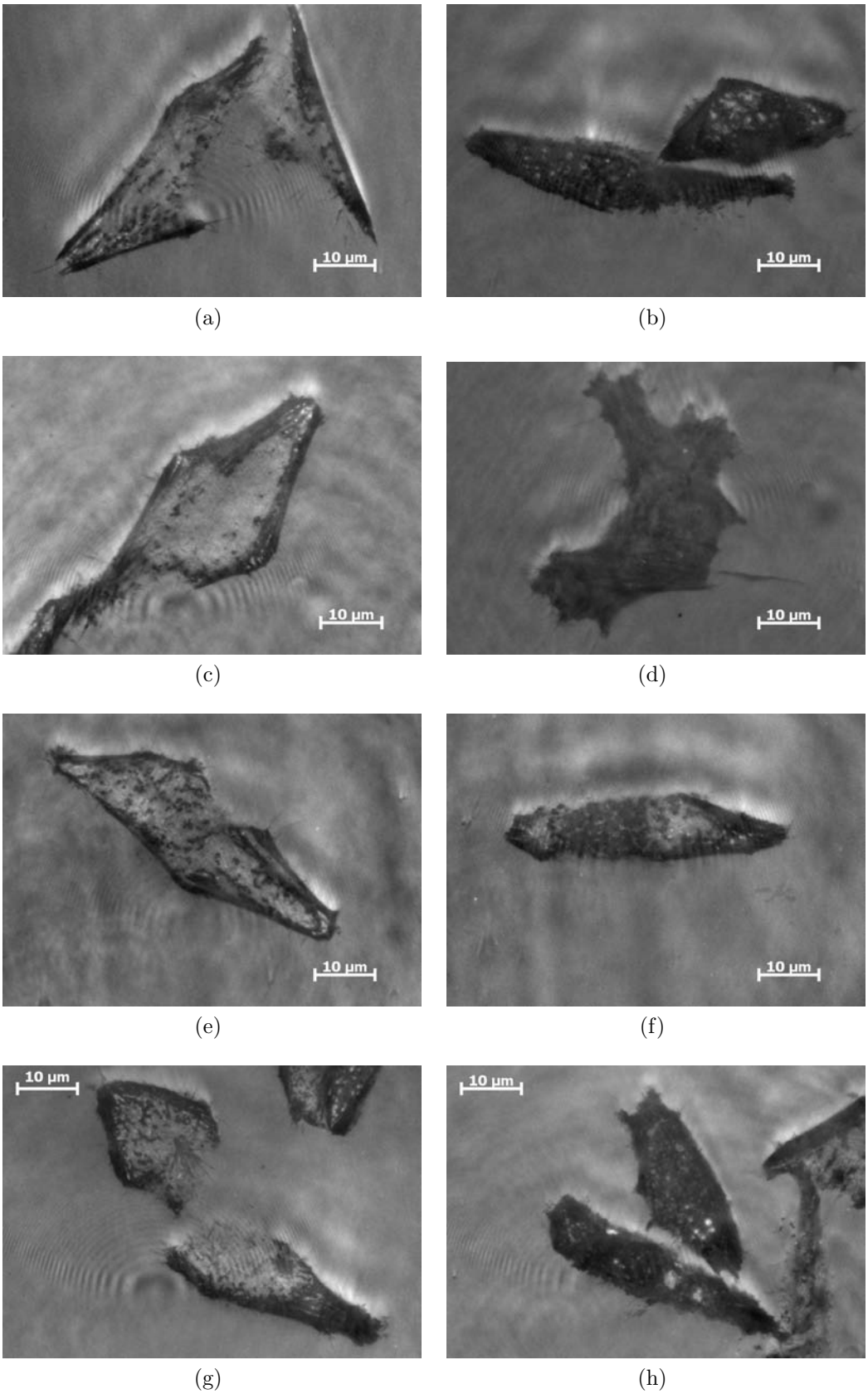

(a) (b)

(c) (d)

(e) (f)

(g) (h)

Figure 6.22: TIRAF measurements of HEK293 cells on different protein coatings. Figures (a), (c), (e), and (g) give an example of a poorly adhered HEK cells on Con-A, PLL, Laminin, and Fibronectin, whereas figures (b), (d), (f), (h) represent the well adhered case, respectively.

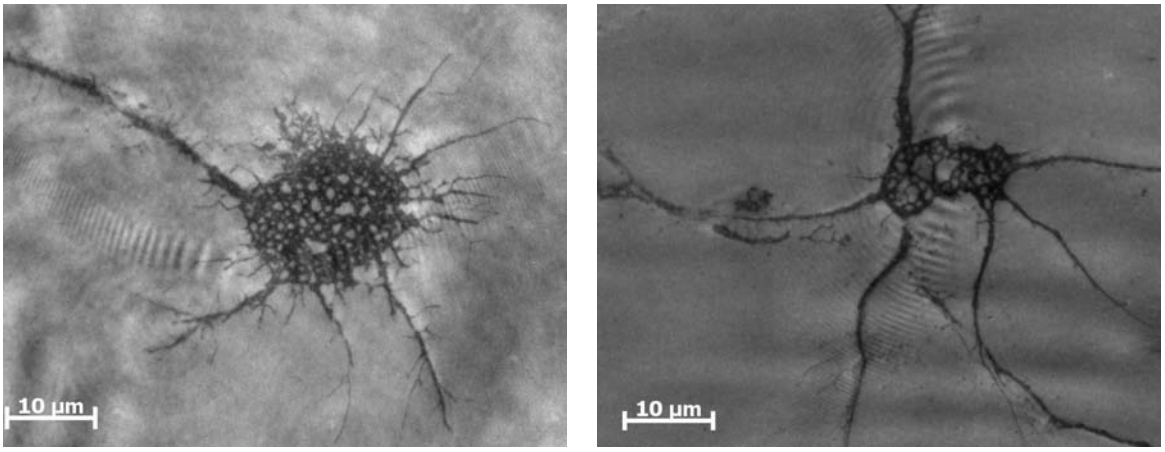

(a) (b)

Figure 6.23: Rat cortical neurons observed with TIRAF and normalized by a reference image. The adhesive profiles were much more homogeneous than the profile of a HEK293 cell. Neurons showed small separation distances with circular areas of large glass-membrane distances.

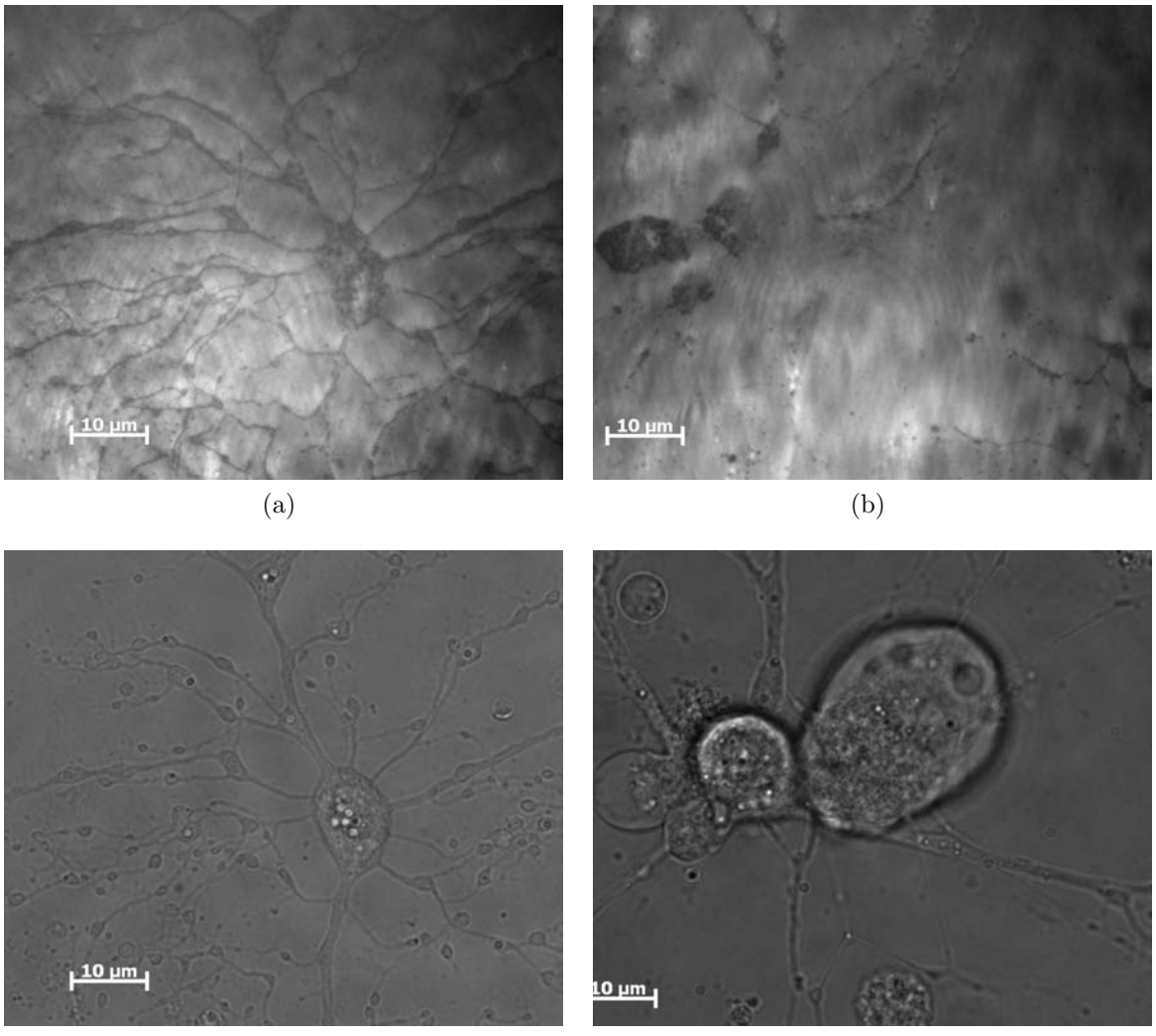

(a) (b)

(c) (d)

Figure 6.24: TIRAF images of cricket neurons grown on Con-A (a, b) with the corresponding bright field images (c, d). The neurons adhered rather poorly (a) to the substrate. For a great number of neurons, no attachment of the cell body to the surface was observed (b).

6.5.2.2 Intracellular Staining

Although intracellular staining introduces more errors to the measurement than extracellular staining, it may be advantageous to use in future applications. For this reason HEK293 cells were stained with calcein-AM. TIRF images of the adhesive region can be seen in figure 6.26. Small separation distances appear bright on a dark background. The images obtained showed a higher homogeneity compared to the TIRAF images, even without normalization by a reference image. One disadvantage of intracellular staining is the existence of background fluorescence signals. A HEK293 cell with a cell body that was almost entirely bound to the surface by long extended point contacts is shown in figure 6.25. Although the cell body seemed to be far away from the glass interface, a background signal was visible in the center region of the image 6.25. This behavior suggests that background fluorescence played an important role in image formation. Although not visible in closely adhered cells (Fig. 6.26), this effect might distort the results obtained from TIRF measurements with intracellular staining.

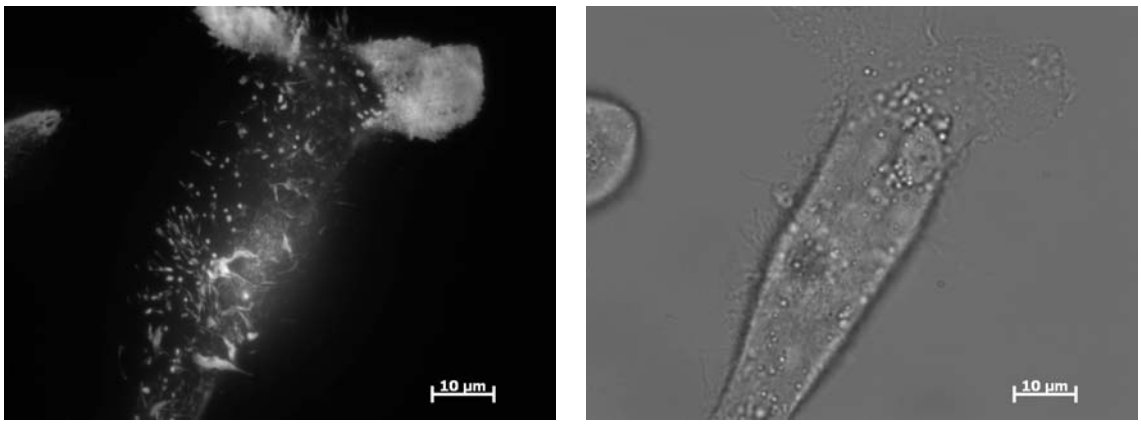

(a) (b)

Figure 6.25: A HEK293 cell that can be seen in the brightfield image (b) showed almost exclusively contact to the glass substrate by point contacts (a). Although the cell body was too far away from the glass interface to be imaged by TIRF, a great amount of background fluorescence was visible in the center region of the cell.

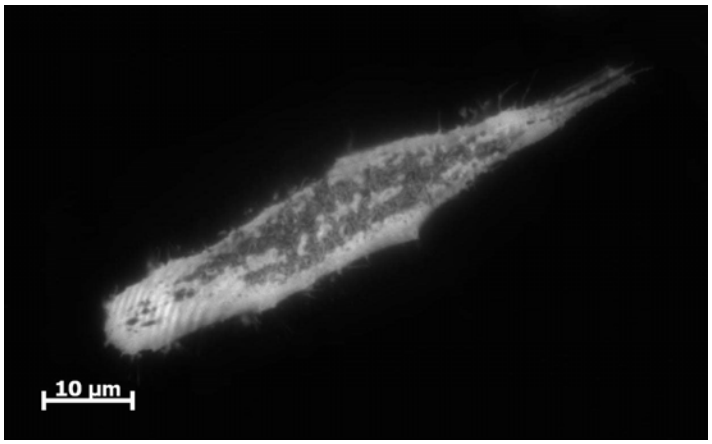

(a)

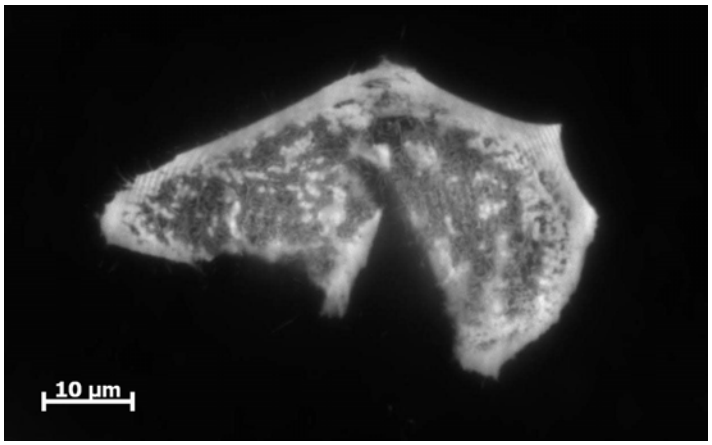

(b)

Figure 6.26: TIRF images obtained with intracellular staining using Calcein-AM. The adhesive region of two cells in close proximity (b) and of a single cell (a) can be seen.

6.5.3 Analysis of Image Intensities

Histograms of TIRAF measurements can give an insight to the morphology of adhesive regions of cells as well as an approximate value of the mean cell substratum distance. In TIRAF measurements, small cell substratum distances showed smaller intensity values than bigger separation distances. This behavior was distorted by protein clusters and stray light, which increased the intensity. Protein clusters also created stray light in their vicinity. However the clusters themself, appeared darker in the image, because proteins have a higher refractive index than the extracellular medium. This optically denser medium dampens the electromagnetic field, yielding a lower intensity value in the image. Histograms can be used to gain statistical values for the whole cellular adhesion area, which correct for these effects to some extend.

In general, for all the histograms in this thesis normalized images were taken. Extracellular areas showed the mean intensity value one after normalization. Values exceeding the intensity one in the histogram are due to two reasons. First, small variations between sample and reference image could cause higher values. Secondly, stray light due to cell membrane and protein clusters also lead to higher values. Since the color values for areas of the adhesive region and the extracellular medium were very close to each other, a template image was created in Corel Draw (CorelDRAW Graphics Suite 12, Corel Corporation, Unterschleißheim, Germany) with two color values for the adhesive region of the cell and the extracellular liquid. This template was used to determine the pixels used for the histograms. In Figure 6.27 are shown two examples of histograms of HEK293 cells cultured on PLL coated glass surfaces. The smallest intensity value in histogram 6.27a is about 0.55 and the peak is located at 0.71 whereas histogram 6.27b exhibits a smallest value of 0.61 and two intensity peaks at 0.85 and 1. The first image represents the case of a homogeneously adhered cell, whereas the second image contains a second peak, describing areas of upwards bulging of the cell membrane. If offsets are defined as before, these peaks can be used to calculate corresponding approximate cell/substratum distances. For the first cell, this resulted in a mean distance of 59 nm, whereas the second cell showed peaks at 90 nm and at a value

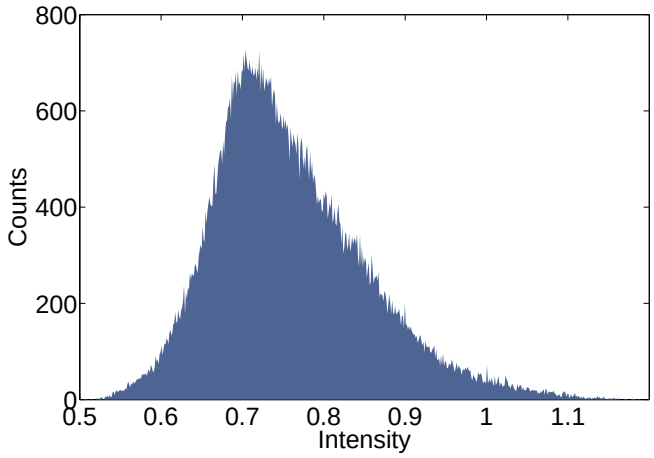

(a)

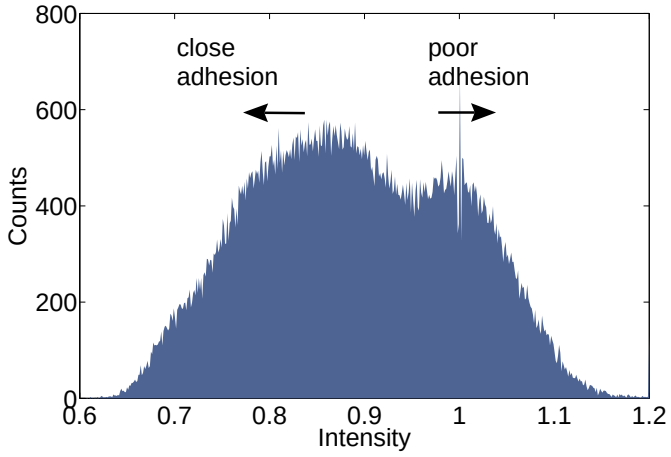

(b)

Figure 6.27: Histograms for two HEK293 cells grown on a PLL coated surface. Figure (a) represents a well adhered and (b) a poorly adhered cell. Close adhesion regions are located on the left side of the histograms, while poorly adhered areas are on the right side.

no longer resolvable by the TIRF setup (higher than 300 nm).

In order to determine the optimum value for the angle of incidence, histograms were done from images of a closely adhered cell at different incident angles. As can be seen in figure 6.28, the sensitivity of the measurement decreased with increasing angles of incidence. In order to obtain a detailed insight to the morphology of the adhesive region, angles close to the critical angle are best suited. Since stray light effects, originating from protein clusters and the cell membrane, decreased with increasing incident angles,

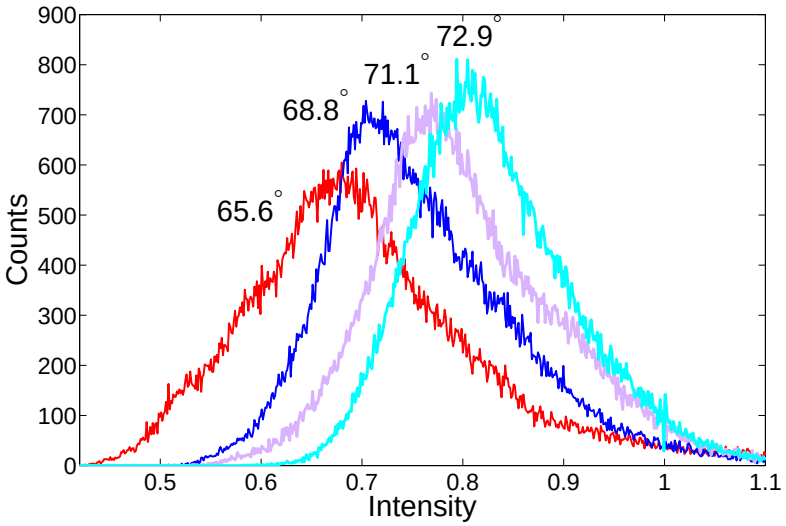

Figure 6.28: Histograms of a closely adhered HEK293 cell on PLL coating for different angles of incidence. It can be seen that sensitivity decreased with increasing angles, because the range of intensity values decreased.

an angle of 68.5° was chosen for the analysis. At this angle, the effect of stray light already decreased drastically, while the intensity distribution was still detailed enough.

In the next section, this histogram technique were used to characterize cell adhesive profiles of HEK293 cells on different protein coatings.

6.5.4 Characterization through Histograms

HEK293 cells were cultured on four different protein coatings. Samples were prepared on 4 different days and measured using TIRAF microscopy. For the histograms, a total of 10 cells for each protein was used, where the maximum amount of cells taken each dish was three. The images were normalized by a reference image in a way that the mean value of an area in the vicinity of the cells was one. Thus, histograms were referenced to this value, which allowed a direct comparison of the images. Two different gaussian fits were performed on each histogram, one single gaussian and one double gaussian fit. The fits revealed peaks for closely (peak 1) and poorly (peak 2) adhered regions, as well as a mean value for the whole adhesive area of the cell. The pixel with the smallest intensity was chosen as an offset value for the histogram. Since offset values and total number of pixels for each cell varied, these fitted values were taken for future analysis.

As can be seen in table 6.2, the mean value of the offset differed for the different

Protein	Peak 1	Peak 2	Mean	Offset
PLL	0.711 ± 0.018	0.877 ± 0.028	0.785 ± 0.019	0.532 ± 0.021
Fibronectin	0.752 ± 0.022	0.874 ± 0.031	0.795 ± 0.016	0.572 ± 0.021
Con-A	0.79 ± 0.016	0.9 ± 0.024	0.831 ± 0.025	0.586 ± 0.024
Laminin	0.772 ± 0.011	0.935 ± 0.023	0.842 ± 0.013	0.591 ± 0.013

Table 6.2: Mean values with standard errors for the results of a single gaussian (mean) and a double gaussian fit (peak 1 and peak 2) for ten HEK cells on each protein coatings.

proteins. This result suggests that the TIRAF images contained values for the absolute height of the cells. For the given proteins, PLL showed the smallest offset value, followed by Fibronectin, Con-A and Laminin. The mean value and the values for the high intensity peaks showed the same tendency. The intensity peak for closely adhered regions on the other hand showed a smaller value for Laminin as for Con-A. The offset values represent the mean closest distance of the cell membrane to the glass interface. Thus, PLL yielded the closest contact for the used proteins. If this offset is defined as areas of focal contact with a 15 nm separation distance [Chen and Singer, 1982; Truskey et al., 1992], the smallest separation distances were [21 ± 2] nm for

Fibronectin, $[24 \pm 2]$ nm for Con-A and $[25 \pm 2]$ nm for Laminin. Mean separation distances were $[79 \pm 4]$ nm for PLL, $[83 \pm 3]$ nm for Fibronectin, $[99 \pm 6]$ nm for Con-A and $[105 \pm 3]$ nm for Laminin. Because of the logarithmic character of equation (3.21) the sensitivity of the height calculations for small intensities was higher than for intensity values of approximately one.

This approach to analyze the adhesive area of cells with histograms revealed information about relative differences between the selected coatings. Absolute height values on the other hand depend strongly on the definition of the offset. In order to circumvent this problem, the next section will provide results of VA-TIRF measurements.

6.5.5 3-D Reconstruction

The HEK293 cells selected for 3-D reconstruction were prepared according to section 5.5.2. In order to keep photo damage to the cell low, the process of searching and focusing on the cell was done by using high angles of incidence. After focusing, a series of images for different angles of incidence was taken. The motor positions were recorded and the corresponding penetration depths were calculated with the assumption of a refractive index of glass $n_G = 1.513$ and a refractive index of the extracellular solution of $n_S = 1.335$. The refractive index of the extracellular solution was measured on 10 different samples with an Abbe refractometer. After calculating the Laplace transformed of the cell images, a fit with the inverse Laplace transformed for every position was performed.

For the cell (cultured on Con-A) in figure 6.30, the reconstruction was done for two lines through the cell. The first line (Fig. 6.32a) represented a closely attached part of the cell. The cleft height reconstruction showed distances of the cell membrane to the glass interface of 40-60 nm. However, when compared to the Laplace transformed (at 69°) of the image, the reconstructed height showed huge distances up to 500 nm for a well adhered region at the edges of the cell. The second line (Fig. 6.32b) was chosen to span the whole cell body. The Laplace transformed of the image showed that for this line and an angle of incidence of 66°, stray light effects were quite huge. A similar behavior could be observed for all other analyzed cells. The reconstructed height profile showed distances from 40 to 500 nm. The height tendency followed the amount of stray light in the original image. The reconstruction contained areas with strong variations in height. This behavior seemed to be equivalent to the reconstruction of simulated noisy data (Sect. 6.2), which suggested that the main reason for this erratic behavior were high levels of noise. In an attempt to reduce the noise level, a gaussian filter was applied to the image data, which smoothened the reconstructed height profile.

The cell in figure 6.31 (cultured on pure glass) showed a huge influence of stray light in the upper parts. The reconstruction was done on the filtered data of the image. Although the reconstructed height profile showed a much smoother appearance due

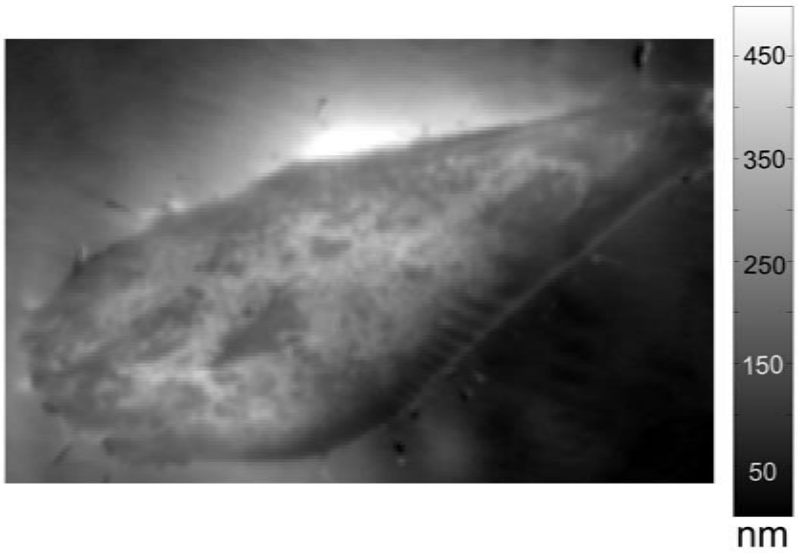

Figure 6.29: Reconstructed height profile of a HEK293 cell cultured on Con-A. The shape of the cell could be recovered, with distances ranging from 40 to 400 nm.

to the gaussian filter, the cell showed still strong variations in the distance between glass substrate and cell membrane. For the first line (Fig. 6.33a), which represents an example of a closely adhered region, distances vary between approx. 150 to 300 nm. The second line (Fig. 6.33b), spanning the whole cell body, showed much higher differences in cell substratum distances. Especially in regions with high amounts of stray light, large distance variations were present.

The reconstruction showed different heights for HEK293 cells cultured on glass and on Con-A. In order to evaluate the reconstruction process over the whole attached area of the cell body, a 3-D reconstruction of a whole cell (cultured on Con-A) was done. Again, the image data was filtered using a gaussian filter. In figure 6.29 the result of the reconstruction process can be seen. The shape of the cell, including small extensions of the cell (filopodia) was successfully reconstructed. However, the cell substratum distances varied from approximately 40 to 400 nm and were higher for the upper region than for the lower region.

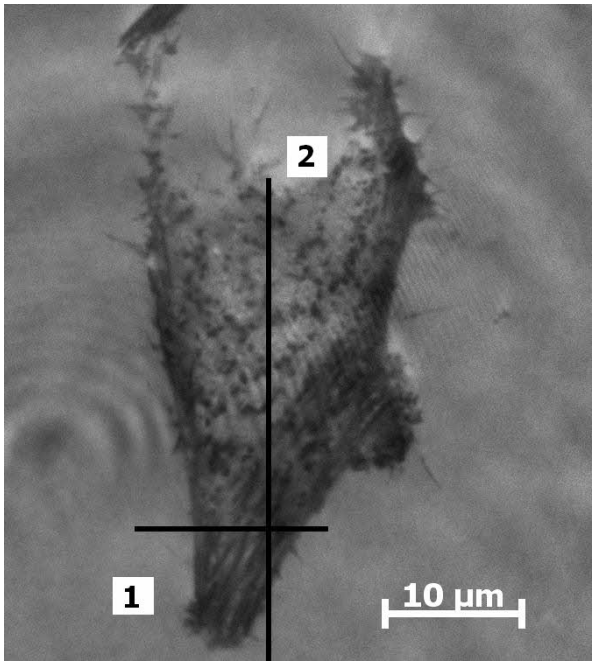

Figure 6.30: Normalized image of a HEK cell cultured on Con-A. Reconstruction was performed on two lines through the cell. Line 1 represents an area of closely attached membrane, whereas line 2 incorporates poorly and well attached regions of the cell.

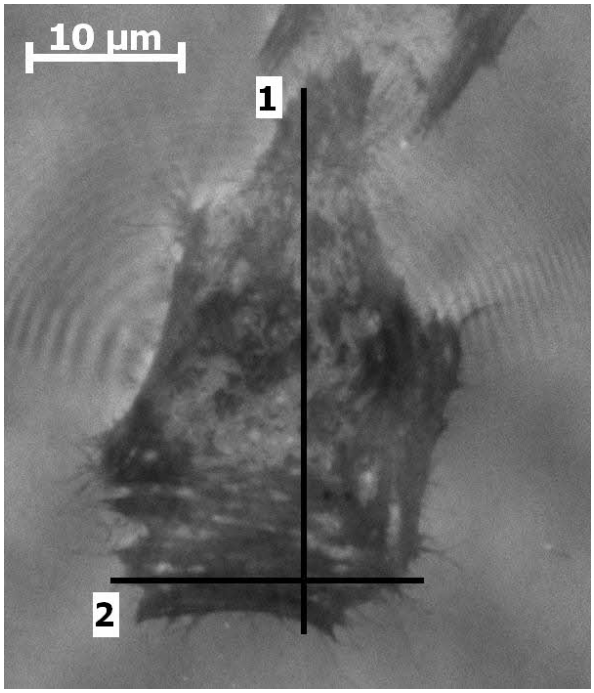

Figure 6.31: Normalized image of a HEK cell cultured on pure glass. Reconstruction was performed on two lines through the cell. Line 1 represents an area of closley attached membrane, whereas line 2 incorporates poorly and well attached regions of the cell.

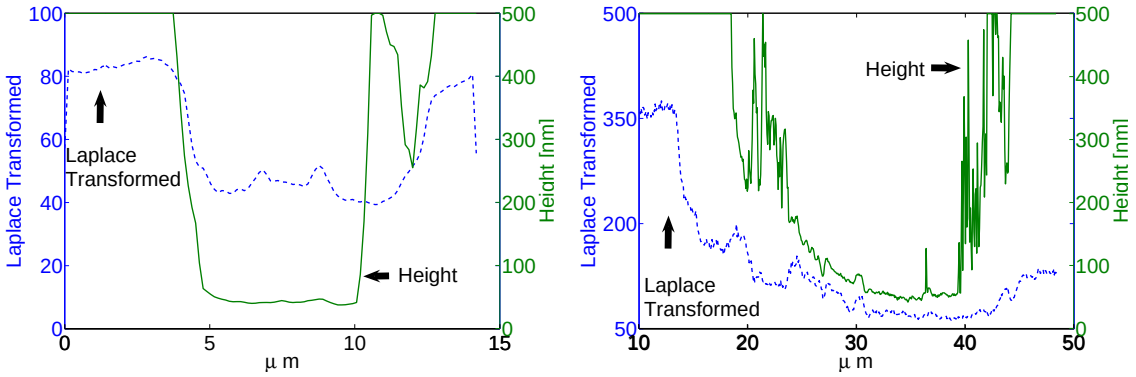

(a) (b)

Figure 6.32: Reconstructed height profile and the intensity of the Laplace transformed plotted over the position for the two lines in figure 6.30. Figure (a) shows the height profile for line 1 and figure (b) for line 2.

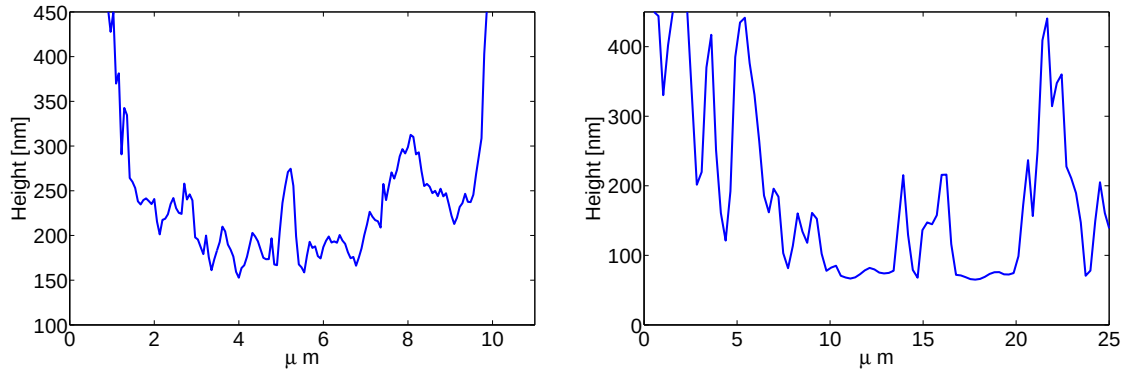

(a) (b)

Figure 6.33: Reconstructed height profile for line 1 (a) and line 2 (b) in figure 6.31.

6.6 Final Opinion about the TIRF Microscopy for Evaluation of the Cell Substratum Interface

6.6.1 Evaluation of the Quality of TIRAF Images using Vinculin Distributions

Although TIRF microscopy can be used to visualize focal adhesion sites, it does not always fully reconstruct focal adhesions due to several reasons. Refractive index variations in the vicinity of the membrane, induced by protein clusters (such as focal adhesions itself) lead to a higher refractive index, which generated stray light effects. As a consequence, regions close to focal adhesions appear brighter. Another reason is the poor lateral resolution of the microscope of 205 nm. This means that the fluorescence intensity measured with the camera (image pixel size of approx. 64.5 nm) is blurred for structures smaller than 205 nm. Given a certain membrane roughness, this effect leads also to a brighter image because of fluorescent signals from neighboring structures. Figure 6.18 showed that the measured diameter of focal adhesive structures was approximately 200 nm. Nevertheless these structures can be even smaller in reality. If the focal adhesion was 100 nm, it would still have shown a diameter of 200 nm in the image of the GFP-labeled vinculin. Thus, the lateral resolution of the setup limits the axial resolution obtainable with TIRAF. The third reason is not based on the experimental setup, but on the cell morphology. Some of the observed variations may be due to the fact that focal adhesions do not always have the same distance between cell membrane and glass substrate. The cells were cultivated on glass and adhered to the ECM produced by themselves. The thickness of this protein layer can vary to some degree. But even if the cells are cultivated on a protein coated substrate, this problem can not be avoided. Since the cells also produce ECM while cultivated on a protein coating, an additional effect due to uneven coating arises.

The values obtained for the histograms showed that the distance of focal adhesions measured with TIRAF is smaller than the distance for other parts of the cell. The

values were obtained by defining the darkest value as 15 nm, which is a value generally accepted for focal adhesions and already used in distance mapping by TIRF [Truskey et al., 1992]. With this assumption, an average distance of 32 nm for the focal adhesion areas and an average value of 76 nm for the distant cell membrane was obtained. For the already mentioned reasons, the mean distance of 32 nm does not represent the distance of focal adhesion. The intensity signal for small focal adhesions is influenced by nearby fluorophores and by generated stray light effects. Furthermore, an image of GFP-labeled vinculin was used as a template to determine the position of the focal adhesions in the TIRAF image. The fluorescence signal from the focal adhesion areas of this image was spatially larger than the actual focal adhesive complexes it marked. Consequently, a two dimensional histogram should show a peak for the intensity generated by a fluorophore layer in the vicinity of focal adhesions rather than a peak for focal adhesions themselves.

6.6.2 Imaging the Cell Adhesive Profile with TIRF-Microscopy

Extracellular staining with TIR illumination can be used to characterize the adhesive region of the cell. In order to get a clear image, the normalization with a reference image was absolutely necessary. Even though most inhomogeneities were successfully extinguished by normalization, for some irregularities remained. Stripe-like patterns were probably due to small air bubbles inside the immersion oil. For all images taken, the setup showed a ring shaped interference pattern in the center of the imaged area, suggesting interferences of the laser with reflected laser light. Although not that apparent, the same patterns were observed for the intracellular staining. This observation suggests that the inhomogeneities had their origin in the microscope setup and not from density variations of the fluorescent dye.

The results showed that the cell adhesive region for different cell types on different protein coatings can be visualized using TIRAF. The images showed in addition that HEK293 cells tend to build close contacts at the outer edges of the cell. This result is in agreement with studies using protein patterning of different shapes [Chen et al.,

2003]. In this study, focal adhesion clustering was observed at the boundaries of the patterns. Areas of upward bulging of the cell membrane, was also previously observed for Fibroblasts which were more than 3 hours in culture [Iwanaga, 2000].

The adhesive structure of rat cortical neurons showed homogeneous close attachment to the substrate with areas of circular upwards bulging of the cell membrane. Similar structures were observed with TIRAF by Geggier and Fuhr [1999] for the cell periphery of L929 Fibroblast cells. Furthermore, neurons seemed to react more even to ECM molecules than HEK293 cells. Although images were taken for a PECM coated surface, which is generally used in our research group, neurons showed the same behavior when cultured on PLL, suggesting that the observed differences were cell type specific and not due to different reactions to the ECM proteins.

Cell bodies of cricket neurons were often not attached to the substrate. This confirmed observations from standard phase contrast microscopy, where the cell body seemed to move when the petri dish is moved.

The results for the intracellular staining showed that the cell adhesive regions can be visualized using this method, too. Compared to TIRAF measurements, this method was superior for quick and qualitative imaging of the adhesive regions. Because of the high levels of signal intensity combined with the dark background, a normalization by a reference image was not necessary to generate clear images. Nevertheless, a normalization yielded smoother images and was necessary if a quantification of the image was performed. Intracellular staining introduced two main errors to the image formation. Firstly, cell organelles change the fluorescent molecule density inside the cell, which altered the measured fluorescence intensity. Secondly, the cell membrane and the membrane of organelles led to a transformation of the evanescent field to a propagating field, generating background fluorescence inside the cell. Previous studies on VA-TIRAF used intracellular staining to generate a three-dimensional adhesion profile of cells [Olveczky et al., 1997]. For this work, VA-TIRF was only used with extracellular staining, because of the lower levels of disturbance of the obtained images, compared to the other labeling methods.

6.6.3 Characterization of the Adhesion Profile with Histograms

TIRAF image histograms for the cell adhesive region can be utilized to distinguish different types of adherence and to generate approximate values for the mean cell substratum distance, by assuming a minimum separation distance of 15 nm [Truskey et al., 1992]. Earlier studies in our research group have shown that HEK293 cells cultured on PLL coatings have the best adhesive characteristics, followed by Fibronectin, Con-A and Laminin [Höller, 2005; Rauf, 2007; Wrobel et al., 2007]. This tendency was also confirmed with the histograms in this work. Compared to the previous studies, TIRF measurements have several advantageous. Höller used TEM measurements of randomly chosen ultramicrotome cuts through fixated HEK293 cells. This method, although having an excellent lateral resolution (2.2 nm), was very time consuming, limited to a single cut and absolute distance values were barely preserved by the complicates preparation procedure. Furthermore, cells were dead and fixated prior to the measurements and artefacts due to the specimen preparation were not totally excluded. The TIRF measurements in this study however, revealed the adhesive structure of the whole living cell. As shown in section 6.5.2, the adhesive profile of HEK cells is quite complex. For this reason, a histogram of TIRAF images clearly contains much more information about the adhesive region of the cell than a single cut through the cell. Therefore, a more exact statistic can be much easier accessed using the TIRF method. Furthermore, the offset difference for the different proteins suggested that the information about the absolute distance between cell membrane and glass was contained in the TIRAF images. Rauf [Rauf, 2007] gained knowledge about the morphology of adhered HEk293 cells by comparing the amount of attached versus non attached cell surface with a confocal microscope. Here, the information about cell attachment is gained without any knowledge about the adhesive region, apart from its area. Therefore, this study could be seen complementary to the previous studies [Höller, 2005; Rauf, 2007; Wrobel et al., 2007].

The values for the mean separation distance of the cells, estimated in the TIRAF measurements, were comparable to previously published results. However, they were

Cell Type	Protein Coating	Mean Distance
Snail Neurons	PLL/growth factor	$[51 \pm 2]$ nm [Zeck and Fromherz, 2003]
Erythrocyte Ghosts	PLL	11-12 nm [Lambacher and Fromherz, 2002]
Vesicles	PLL	$[6.6 \pm 5]$ nm [Zeck and Fromherz, 2003]
HEK 293	PLL	50 nm [Braun and Fromherz, 2004]
HEK 293	Fibronectin	$[70 \pm 10]$ nm [Brittinger and Fromherz, 2005]
Fibroblasts	Fibronectin	$[50 \pm 10]$ nm [Iwanaga et al., 2001]
Rat Neurons	Fibronectin	$[60 \pm 5]$ nm [Braun and Fromherz, 1998]
Rat Neurons	Laminin	$[105 \pm 5]$ nm [Braun and Fromherz, 1998]
Snail Neurons	Laminin	$[87.5 \pm 1.5]$ nm [Zeck and Fromherz, 2003]
Vesicles	Laminin	$[160 \pm 12]$ nm [Zeck and Fromherz, 2003]

Table 6.3: Separation distances for different proteins on a variety of samples measured with FLIC microscopy.

calculated with the somewhat arbitrary assumption of a minimum separation distance of 15 nm. This procedure was previously used in TIRF measurements to assign distances to intensity values [Truskey et al., 1992]. It can be seen from table 6.3 that the mean distances showed a broad range of variations. These variations depend largely on the type of the measured sample and on the experimental protocol used. For PLL and Fibronectin the estimated mean distances by TIRAF were higher than reported before. This difference may be due to different incubation times of the cells before measurements. Distance studies were often performed after a short incubation period, because a large degree of upwards bulging of the cell membrane can be observed for cells plated on the substrate for a few hours Iwanaga [2000]. The measurements for the histograms in this thesis were performed for cells approximately 24 h after plating and also here the bulging was observed for a large amount of cells. This difference in protocol may be responsible for the higher mean separation distances.

Apart from that, TIRAF measurements exhibit several possible sources of errors. The visualized image was composed of information about the separation distance and the refractive index present in the cleft. In order to gain knowledge about the separation distance, assumptions about the refractive index had to be made. In this thesis the refractive index in the cleft was taken as homogeneous and equal to the refractive

index of the surrounding medium. Of course, this assumption introduced an error to the calculations, since the protein coating had a different refractive index, as well as the focal adhesion complexes. Another assumption was that no fluorescent signal was observed from areas of the upper part of the cell. The error introduced by this assumption is small, because the exciting field had an evanescent wave character. Consequently, because the other side of the cell had a distance of typically several micrometers this error can be neglected. However, the different refractive indices of the cell membrane and the cytoplasm led to conversion of the evanescent field into normal propagating light. Gingell et al. [1987] analyzed all possible cases for this source of error for TIRAF measurements and derived correcting equations to compensate for this effect. In this thesis, these equations were not used, since the effect was relatively small for extracellular staining and the inverted position of the objective. Furthermore, the equations depend on the angle of incidence from the extracellular solution to the cell membrane and were thus only correct for the case of a smooth cell membrane parallel to the glass interface. Since the HEK293 cells showed strong variations in the inclination angle of the cell membrane, the usefulness of the equations was questioned. In order to derive these equations, assumption regarding the refractive index of the cell membrane and the cytoplasm have to be made, which would in turn also introduce further uncertainties. For these reasons, the correcting factors derived by Gingell et al. [1987] were not useful for the purposes in this thesis.

6.6.4 Height Profile Reconstruction

The 3-D reconstruction process showed the same sources of errors as discussed in the previous section. The recovered height profile showed smooth areas with erratic height changes. These strong changes indicate that the reconstruction process was not successful for at least a certain part of the cell. The main reason for these errors when reconstructing the height profile, apart from the already discussed errors,were noise levels in the same order of magnitude as the intensity decay of the Laplace transformed. This noise was mainly introduced to the image by unsuccessful normalization

with the reference image. Small changes in the reference image as well as changing interference fringes introduced errors to the Laplace transformed. Compared to the analysis with image histograms, interference fringes have a much larger impact on the 3-D reconstruction. Another limitation was the relatively small angle range. The intensity decay of the Laplace transformed for a fluorphore layer thickness of 50 nm was 38% for an angle variaton between 66° to 73° and only 20% for angles between 68° and 73°. For angles bigger than 68° most of the effects of stray light due to the cell membrane vanished, since the cell membrane has a refractive index of typically 1.4. However, the 3-D reconstructions including only angles bigger than 68° showed even poorer results, than the ones for angles exceeding 66° (data not shown). Consequently, the 3-D reconstruction was not done for a large extent in this thesis.

7 Conclusion and Outlook

7.1 Conclusion

In this thesis, the possibilities of a commercially available TIRF microscope was evaluated to characterize the interface region between cell and substrate. Different staining methods can be used to obtain the information about the cleft. Extracellular staining with the low molecular weight, cell membrane impermeable Alexa Fluor 488 hydrazide showed better results than the intracellular staining using the cell membrane permeable Calcein-AM dye. TIRF measurements with extracellular staining (TIRAF) showed smaller amounts of background fluorescence and errors resulting optical multilayer problem appeared to be smaller. TIRAF revealed the adhesive region of different cell types for a range of different proteins with high contrast and an axial resolution that was in the range of several nanometers. The validity of the results was confirmed by TIRF measurements of cells transfected with GFP-labeled vinculin. These measurements showed the excellent contrast enhancement of TIRF microscopy compared to standard epi-fluorescent illumination for fluorescence microscopy of proteins involved in the process of cell adhesion. Image histograms of TIRAF images can be used to minimize the effect of interference fringes, typically for through-the-objective TIRF setups, which use a laser as illumination source [Axelrod, 2001]. Using such histograms, the effect of different ECM proteins on cell adhesion was successfully analyzed. First distance estimations from the TIRAF measurements revealed mean distances, which are comparable to distances obtained by different techniques published in literature.
One goal of this thesis was to establish a VA-TIRF setup in our setup, using a commercial TIRF microscope and normal glass cover slips. Although the angle variation of the

incoming laser beam was achieved in a precise, reproducible and fully automated way, optical limitations of the setup restricted the accuracy of the 3-D reconstructions. The angles that were usable for VA-TIRF were restricted to values exceeding approximately 66°, which limited the variable angle range to only a few angles. Furthermore, stray light effects and interference fringes originating from the sample and internal components of the microscope introduced errors to the data that were unacceptable high for angles of incidence larger than 70°.

For our research group the information about the cell substratum separation distance with respect to electrophysiological measurements using electrical devices is of great importance. The mean height of the cleft between cell membrane and sensor interface is directly connected to the junction resistance R_J, which is important for the measured signal. It was shown in this thesis that the mean separation distance of HEK293 cells on PLL and Fibronectin coated surfaces was smaller than for the surfaces coated with Con-A and Laminin. Additionally, TIRAF measurements revealed detailed information about the geometry of the adhesion areas for different cell types. HEK293 cells had the tendency to adhere tightly at their edges. This adhesion structure indicates the complex physical, chemical, and electrical nature of the processes involved during electrophysiological measurements with electrical devices. Furthermore, this structure could explain the relatively high signals recorded for HEK293 cells compared to rat cortical neurons. Rat cortical neurons showed smooth adherence with areas of circular upwards bulging of the cell membrane. This knowledge may be used to generate theoretical predictions of the electrical signal and to explain why these cells show a small signal although tightly adhered to the surface. TIRAF measurements revealed that the cricket neuron cell bodies were often not adhered to the surface, which explains why electrical measurements of cricket neurons have profen difficult to be achieved in the past. The methods presented in this thesis are the tools necessary for future studies regarding cell adhesion on different protein coated surfaces, to further optimize the extracellular electrophysiological measurements of different electrical active cells.

7.2 Outlook

7.2.1 Improvement of the Experimental Setup

The experimental setup used in this thesis could be improved in future, by reducing the amount of stray light and interference effects. The stray light could be reduced by using specialized cover slips, with an extra flat surface. Furthermore, the use of an objective with a higher numerical aperture (plan-apochromat objective with $NA = 1.46$ (ZEISS) or $NA = 1.65$ (Olympus)), which allows a larger range of accessible angles, may yield better results. Additionally to the normalization with a reference image, interference fringes can be effectively eliminated by oblique, rapid azimuthal rotation of the plane of incidence of the laser light [Mattheyses et al., 2006]. For example, this can be achieved with a commercially available optical fiber mode scrambler attached between optical fiber and TIRF-slider. Higher sensitivity for low intensity fluorescent signals can achieved by using a 63× objective with the same NA as the 100× objective used in this thesis, because the collected light intensity is inverse proportional to the magnification of the objective.

7.2.2 Possible future Experiments with the Setup

The results for the analysis through image histograms showed promising results in the evaluation of the cell substratum cleft. It may be interesting to conduct further studies using this method, including different cell types and more ECM proteins. The biggest downside of the method is the missing information about the absolute distance values. This may be addressed by Förster Resonance Energy Transfer (FRET) measurements. FRET describes a radiationless energy transfer between two fluorescent molecules in close proximity. The intensity of the FRET depends on the distance between the two fluorophores and can be used to measure distances (typically < 10 nm). If the fluorophores are attached to the cell membrane and to the substrate by spacer molecules with known size, it could be possible to assign very precise offset values to adhesion structures like focal adhesions.

Apart from that, the excellent contrast enhancement of the TIRF microscope could be used to characterize the adhesive region of the cell by means of labeling different proteins involved in cell adhesion.

In a future study, a characterization of the adhesive profile starting from the first attachment of the cell, should reveal the point of time where the upwards bulging of the cell membrane starts. By this means, the time for electrophysiological measurements and cell-sensor measurements could be tuned to the time of optimum device coverage of the cell.

Another possible experiment could reveal details about the curvature of the cell membrane. A cell membrane that is homogeneously adhered to the substrate should show smaller angles of inclination with respect to the substrate than a cell membrane containing large areas of upwards bulging. Here, the effect of fluorescent dyes incorporated into the cell membrane (e.g. DiI, DiO) could be used to obtain information about the angle of inclination. These dyes, incorporated parallel to the cell membrane plane, show different fluorescent emission characteristics for different inclination angles of the cell membrane and for different polarizations of the laser light. If the polarization of the laser light is switched from p- to s-polarization, a difference in fluorescent emission intensity should be observable that is directly connected to the curvature of the cell membrane.

A List of Abbreviations

ADP: Adenosine diphosphate

ATP: Adenosine triphosphate

BFP: Back focal plane

Con-A: Concanavalin-A

ECM: Extracellular matrix

FET: Field effect transistor

FLIC: Fluorescence-interference-contrast microscopy

GFP: Green fluorescent protein

ISFET: Ion sensitive field-effect transistors

MOSFET: Metal oxide semiconductor field-effect transistor

NA: Numerical aperture

PBS: Phosphate buffered solution

PECM: Extracellular matrix with poly-D-lysine

PDL: Poly-D-lysine

PLL: Poly-L-lysine

RICM: Reflection-interference-contrast microscopy

STED: Stimulated emission depletion

TEM: Transmission electron microscopy

TIRF: Total-internal-reflection-fluorescence microscopy

TIRAF: Total-internal-reflection-aqueous-fluorescence microscopy

VA-TIRF: Variable-angle-total-internal-reflection-fluorescence-microscopy

B Near-field effects

For the given application, the region of interest is between 0 nm and 250 nm. Thus, the effects arising from considering near field physics have to be analyzed. The theory of near field physics in the case of TIRF was described and rigorously derived by Hellen and Axelrod [Hellen and Axelrod, 1987]. The cases of a simple glass-liquid interface and a three layer problem with a dielectric layer in-between will be considered.

B.1 Two Layer Problem

Near field effects at a simple glass-liquid interface can be described by a system with two infinite areas of water ($n_1 = 1.33$) and glass ($n_3 = 1.518$). The interface is positioned at $z = 0$ and parallel to the xy-plane. Entering the glass with an incidence angle θ bigger than θ_C, the light creates an evanescent wave, with properties described in (3.17) and (3.16). An observer is positioned at $\vec{r}(r, \theta, \phi)$ with radius r, polar angle θ and azimuthal angle ϕ (Fig. B.1)

The evanescent wave excites a fluorophore positioned at $\vec{r}'(z', \theta', \phi')$, with polar angle θ' azimuthal angle ϕ' and interface distance z' as defined in Fig. B.1 (a). The general model for a fluorescent molecule is a dipole with an emission of constant amplitude. In this case however, the fluorophore has to be described by a dipole driven by a constant power source. This is because the amount of power the dipole emits is directly proportional to the amount of absorbed power. In contrary, a constant amplitude dipole dissipates power over a brought spectrum, depending on the dipole's position and environment. Thus the assumption of a constant amplitude dipole would lead to wrong predictions. The model of the constant power dipole is calculated by normalizing

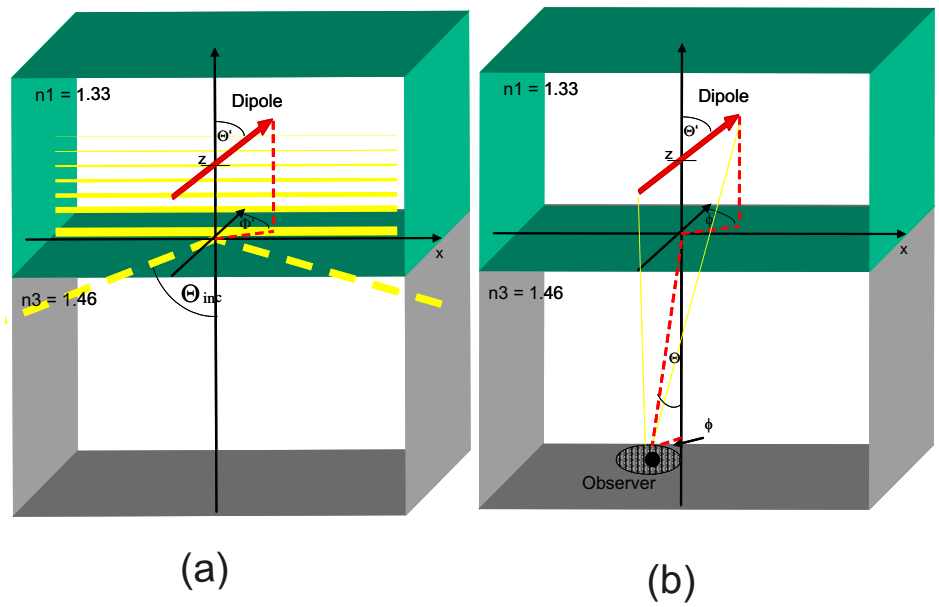

Figure B.1: (a) The evanescent wave, evoked by an incident electromagnetic wave, excites a dipole positioned at $\vec{r}'(z', \theta', \phi')$. (b) The dipole's emitted intensity is collected by an observer positioned at $\vec{r}(r, \theta, \phi)$.

the radiated intensity $S(\vec{r}, \vec{r}')$ of a fixed amplitude dipole at position $\vec{r}'$, observed at $\vec{r}$ with the total dissipated Power $P_T(\vec{r}')$. This image is equivalent to the constant power dipole model. Considering a quantum efficiency of 1, where the emitted and absorbed power of the dipole are equal, the total emitted power is equal to the total absorbed power of the dipole. The radiated intensity S is then given by the squared Poynting vector

$$S(\vec{r}, \vec{r}') = \frac{c\sqrt{\epsilon}}{8\pi} |\vec{E}|^2 \ , \tag{B.1}$$

with the speed of light c and the dielectric constant of the dipole containing medium ϵ. The normalized intensity $\widehat{S}(\vec{r}, \vec{r}')$ of the constant power dipole is

$$\widehat{S}(\vec{r}, \vec{r}') = \frac{S(\vec{r}, \vec{r}')}{P_T(\vec{r}')} \ . \tag{B.2}$$

If $\widehat{S}$ is multiplied with the input power to the dipole, the result is the intensity I, which is radiated by a constant power dipole. The input power is given by the absorption dipole moment $\vec{\mu}^{ab}$ and the external exciting electrical field $\vec{E}^{ex}$, which in this case is given by equation (3.16) or equation (3.17).

$$I(\vec{r},\vec{r}') = \widehat{S}(\vec{r},\vec{r}')|\vec{\mu}^{ab}\cdot\vec{E}^{ex}|^2 \tag{B.3}$$

To get the complete radiated intensity by a distribution of dipoles $D(z',\theta',\phi')$, the single dipole intensities need to be integrated over the whole area $z>0$. In order to calculate the intensity collected by the observer, this intensity needs to be integrated again over the whole range of possible angles for the observer. The maximum angle θ_{max} is given by the numerical aperture of the objective (3.3)

$$\theta_{max} = \arcsin(NA/n_3)\ . \tag{B.4}$$

The resulting expression is similar to equation (3.18):

$$F_{x,y}(\theta) = I_{x,y}(0,\theta)\cdot\int_0^\infty D_{x,y}(z)Q(z)e^{-z/d_p(\theta)}dz\ . \tag{B.5}$$

The collection efficiency $Q(z)$ is the ratio of the total energy dissipated by a fluorophore to that energy, collected by a microscope objective. In order to calculate Q, we need to express the equations in integration variables. Ford and Weber [Ford and Weber, 1984] show that the total dissipated power of a constant power dipole P_T can be divided into the power emitted by dipoles orientated parallel P_T^p and perpendicular P_T^s to the interface

$$P_T(z,\theta') = \cos^2(\theta')P_T^s(z) + \sin^2(\theta')P_T^p\ . \tag{B.6}$$

P_T^p and P_T^s are given by:

$$P_T^s(z) = \frac{c\mu^{ab}k_1^4}{4n_1^3}\Re\Big[\int_0^\infty \nu(1-\nu^2)^{-1/2}\big((1+r^s e^{i2k_1 z\sqrt{1-\nu^2}}) + ((1-\nu^2)(1-r^p e^{i2k_1 z\sqrt{1-\nu^2}}))\big)d\nu\Big] \; ; \tag{B.7}$$

$$P_T^p(z) = \frac{c\mu^{ab}k_1^4}{2n_1^3}\Re\left[\int_0^\infty \nu^3(1-\nu^2)^{-1/2}(1+r^p e^{i2k_1 z\sqrt{1-\nu^2}})d\nu\right] \; . \tag{B.8}$$

The integration constant ν is the sine of the polar angle θ' of the emitted light with values from zero to infinity, to account for imaginary values due to TIR illumination. $k_1 = 2\pi n_1/\lambda$ is the wave number in medium 1, while r^s and r^p are the reflection coefficients for s- and p-polarized light. The reflection and transmission coefficients [Wachter and Hoeber, 1998] can be expressed as functions of $\nu = \sin(\theta')$ by exchanging the variable θ' by ν in the Fresnel equations with $\epsilon_{i,j} = \sqrt{n_i/n_j}$:

$$r^p = \frac{\sqrt{1-\nu^2} - \epsilon_{1,3}\sqrt{\epsilon_{3,1}-\nu^2}}{\sqrt{1-\nu^2} + \epsilon_{1,3}\sqrt{\epsilon_{3,1}-\nu^2}} \; ; \tag{B.9}$$

$$r^s = \frac{\sqrt{1-\nu^2} - \sqrt{\epsilon_{3,1}-\nu^2}}{\sqrt{1-\nu^2} + \sqrt{\epsilon_{3,1}-\nu^2}} \; ; \tag{B.10}$$

$$t^p = \frac{2\sqrt{1-\nu^2}}{\sqrt{\epsilon_{3,1}}\sqrt{1-\nu^2} + \sqrt{\epsilon_{1,3}}\sqrt{\epsilon_{3,1}-\nu^2}} \; ; \tag{B.11}$$

$$t^s = \frac{2}{1+\sqrt{\frac{\epsilon_{3,1}-\nu^2}{1-\nu^2}}} \; . \tag{B.12}$$

Figure B.2a shows the results for the corresponding total dissipated powers. The vicinity of the optically denser medium to the dipole turns near fields of the dipole into far fields, leading to an elevated level of radiation. Therefore, the dissipated power up to a distance of about 100 nm is elevated. In order to use the reflection and transmission

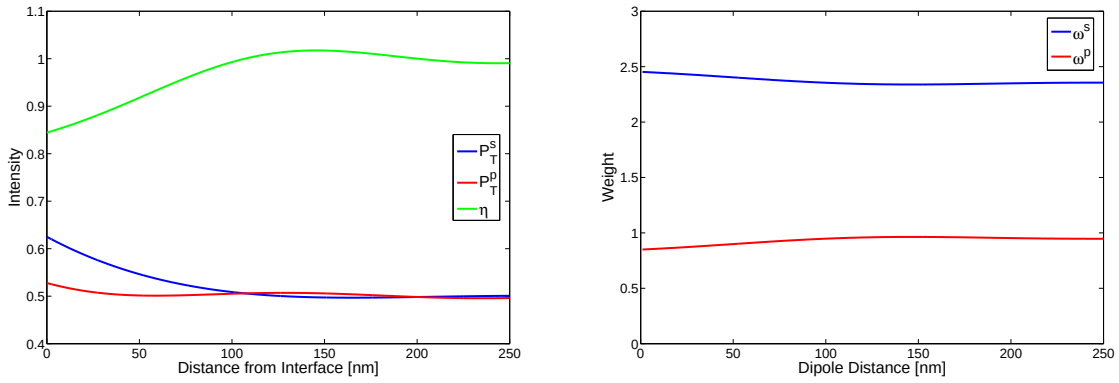

(a) (b)

Figure B.2: (a) Total dissipated power for $n_1 = 1.33$, $n_3 = 1.518$ and $\lambda_{em} = 520$ nm. P_T^p is generally smaller than P_T^s and η reaches one after approximately 100 nm. (b) Weightings for s-polarized light in dependence of the dipole distance to the interface. The values were calculated using the equations for the exciting electrical field. The weighting for perpendicular orientated dipole ω^s is approximately twice as large as the weighting for parallel dipoles ω^p.

coefficients ((B.9) to equation (B.12)) to calculate the electrical field produced by a constant power dipole, the emission dipole moment μ of the dipole has to be divided into three orientations. The plane of observation shall be defined by the observation point $\vec{r}$ and the z-axis. Then, μ^p is the component of μ lying in the plane of observation and parallel to the interface, μ^s is the component lying perpendicular to the plane of observation and parallel to the interface and μ^z is orientated along the z-axis and perpendicular to the interface. For these orientations we can find the corresponding squared electrical fields in [Hellen and Axelrod, 1987]

$$|\vec{E}_3^{\mu_p}|^2 = \frac{\mu^2 k_3^4 \cos^2(\theta)}{n_1^2 n_3^2 r^2} |t^p e^{ik_1 \alpha z}|^2 \ ; \tag{B.13}$$

$$|\vec{E}_3^{\mu_s}|^2 = \frac{\mu^2 k_3^4 \cos^2(\theta)}{n_1^2 n_3^2 r^2 |\alpha|^2} |t^s e^{ik_1 \alpha z}|^2 \ ; \tag{B.14}$$

$$|\vec{E}_3^{\mu_z}|^2 = \frac{\mu^2 k_3^4 \cos(\theta) \sin^2(\theta)}{n_1^2 r^2 |\alpha|^2} |t^p e^{ik_1 \alpha z}|^2 \ , \tag{B.15}$$

where α is defined as $\alpha = \sqrt{1 - \frac{\sin^2(\theta_{inc})}{\sin^2(\theta_C)}}$ (compare equation (3.9)). For a random orientation of dipoles, the radiated intensity $\widehat{S}$ can be integrated over all azimuthal angles ϕ. After division by 2π, this yields the averaged normalized value $< \widehat{S} >_\phi$

$$< \widehat{S} >_\phi = \frac{< \widehat{S} >_\phi^s (z, \theta)}{1 + \eta(z) \tan^2(\theta')} + \frac{< \widehat{S} >_\phi^p (z, \theta)}{1 + (\eta(z) \tan^2(\theta'))^{-1}} \ . \tag{B.16}$$

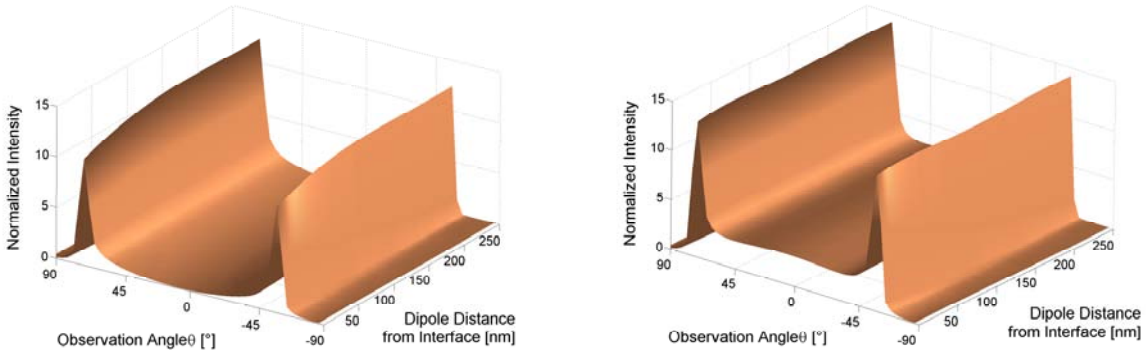

(a) (b)

Figure B.3: The ϕ-averaged normalized Intensity $< \widehat{S} >_\phi$ as a function of dipole distance z and observation angle θ for (a) perpendicular orientation and (b) parallel orientation of the dipole with respect to the interface.

The normalized intensity can be also divided in one part for a parallel (Fig. B.3b) and another part for perpendicular (Fig. B.3a) orientated dipoles with respect to the interface:

$$< \widehat{S} >_\phi^s = \frac{c n_1}{8\pi} \frac{|\vec{E}_3^{\mu_z}|^2}{P_T^s(z)} \ ; \tag{B.17}$$

$$< \widehat{S} >_\phi^p = \frac{c n_1}{16\pi} \frac{|\vec{E}_3^{\mu_p}|^2}{P_T^p(z)} + \frac{c n_1}{16\pi} \frac{|\vec{E}_3^{\mu_s}|^2}{P_T^p(z)} \ . \tag{B.18}$$

The emitted intensity of fluorophores near a glass water interface is highly anisotropic and depends on the dipole orientation. In contrast to fluorophores far away from the

interface, much of the intensity is emitted for angles greater than the critical angle, with a sharp peak right at the critical angle (Figure B.1). This accounts for an energy flow toward the optically denser medium. If near field effects are supposed to be observed, it is important to have an objective with a high aperture angle that can capture this peak. The integration of $< \widehat{S} >_\phi$ over the polar observation angle θ gives the fraction of the total energy dissipated by a dipole, which is collected by an observer. This fraction is the above mentioned collection efficiency Q

$$Q(z) = \frac{\text{Collected Power}}{\text{Total Dissipated Power}}$$

$$= \frac{[\omega^s Q^s(z) + \omega^p Q^p(p)]}{\omega^s + \omega^p} \ , \tag{B.19}$$

where $Q^s(z)$ and $Q^p(z)$

$$Q^{s,p} = 2\pi r^2 \int_0^{\theta_{max}} < \widehat{S} >_\phi^{s,p} (z,\theta) \sin(\theta) d\theta \ , \tag{B.20}$$

are the fractions for parallel and perpendicular orientated dipoles and ω^s and ω^p are weighting factors derived by the exciting field. For an arbitrarily orientated dipole distribution, where the absorption dipole moment $\vec{\mu}^{ab}$ is parallel to the emission dipole moment $\vec{\mu}$, the weighting factors are given by an integration of the exciting components $|\vec{\mu}^{ab} \cdot \vec{E}^{ex}|^2$ over the possible dipole angles (Fig. B.2b)

$$\omega^p = \int_0^\pi \frac{\sin^5(\theta')}{\sin^2(\theta') + \eta(z)^{-1} \cos^2(\theta')} \ ; \tag{B.21}$$

$$\omega^s = \int_0^\pi \frac{\sin^3(\theta') \cos^2(\theta')}{\cos^2(\theta') + \eta(z) \sin^2(\theta')} \ . \tag{B.22}$$

η (Fig. B.2a) is defined as :

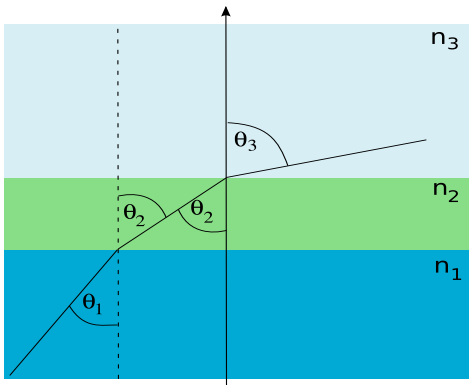

Figure B.4: The relation between the three different angles can be expressed as a function of θ_1

$$\eta(z) = \frac{P_T^p(z)}{P_T^s(z)} \ . \tag{B.23}$$

B.2 Three Layer Problem

The equations for the two layer problem need to be changed, if a third intermediate layer is introduced. In this work, the third layer consists of a protein coating, which can be considered as a dielectric. The refractive index of proteins forming a layer on top of a substrate can vary between 1.34 and 1.5, depending on the substrate, the shape of the protein, the grade of denaturation and the solution surrounding the protein [Guemouri et al., 1998; Voros, 2004]. The equations that have to be altered are equations that depend on light passing through the layers and use the refraction and transmission coefficients given by the Fresnel equations. In order to include the third layer into the equations, altered coefficients have to be used, instead of the coefficients given in equations (B.9) to (B.12). These coefficients can be deducted by the Fresnel equations describing the interface between glass and protein ($t_{1,2}^s$, $t_{1,2}^p$, $r_{1,2}^s$, $r_{1,2}^p$) and the interface between protein and liquid ($t_{2,3}^s$, $t_{2,3}^p$, $r_{2,3}^s$, $r_{2,3}^p$).

The Fresnel equations are a function of the sine of the incident electromagnetic wave vector and the normal vector of the interface. The relationship between the three angles in the three layers (Fig. B.4) is given by Snell's law as $n_1 \sin(\theta_1) = n_2 \sin(\theta_2) = n_3 \sin(\theta_3)$. For the interface between medium 2 and medium 3, the Fresnel equations

can be expressed as a function of ν:

$$n_2 \sin(\theta_2) = n_1 \sin(\theta_1)$$

$$\Leftrightarrow \quad \sin(\theta_2) = \frac{n1}{n2} \sin(\theta_1) = \sqrt{\epsilon_{1,2}}\ \nu \ .$$

The resulting Fresnel equation are

$$r^p_{1,2} = \frac{\sqrt{1-\nu^2} - \epsilon_{1,2}\sqrt{\epsilon_{2,1}-\nu^2}}{\sqrt{1-\nu^2} + \epsilon_{1,2}\sqrt{\epsilon_{2,1}-\nu^2}} \ ; \tag{B.24a}$$

$$r^p_{2,3} = \frac{\sqrt{1-\epsilon_{1,2}\nu^2} - \epsilon_{2,3}\sqrt{\epsilon_{3,2}-\epsilon_{1,2}\nu^2}}{\sqrt{1-\epsilon_{1,2}\nu^2} + \epsilon_{3,2}\sqrt{\epsilon_{2,3}-\epsilon_{1,2}\nu^2}} \ ; \tag{B.24b}$$

$$r^s_{1,2} = \frac{\sqrt{1-\nu^2} - \sqrt{\epsilon_{2,1}-\nu^2}}{\sqrt{1-\nu^2} + \sqrt{\epsilon_{2,1}-\nu^2}} \ ; \tag{B.24c}$$

$$r^s_{2,3} = \frac{\sqrt{1-\epsilon_{1,2}\nu^2} - \sqrt{\epsilon_{3,2}-\epsilon_{1,2}\nu^2}}{\sqrt{1-\epsilon_{1,2}\nu^2} + \sqrt{\epsilon_{3,2}-\epsilon_{1,2}\nu^2}} \ ; \tag{B.24d}$$

$$t^p_{1,2} = \frac{2\sqrt{1-\nu^2}}{\sqrt{\epsilon_{21}}\sqrt{1-\nu^2} + \sqrt{\epsilon_{1,2}}\sqrt{\epsilon_{2,1}-\nu^2}} \ ; \tag{B.24e}$$

$$t^p_{2,3} = \frac{2\sqrt{1-\epsilon_{1,2}\nu^2}}{\sqrt{\epsilon_{32}}\sqrt{1-\epsilon_{1,2}\nu^2} + \sqrt{\epsilon_{2,3}}\sqrt{\epsilon_{3,2}-\epsilon_{1,2}\nu^2}} \ ; \tag{B.24f}$$

$$t^s_{1,2} = \frac{2}{1+\sqrt{\frac{\epsilon_{2,1}-\nu^2}{1-\nu^2}}} \ ; \tag{B.24g}$$

$$t^s_{2,3} = \frac{2}{1+\sqrt{\frac{\epsilon_{3,2}-\epsilon_{1,2}\nu^2}{1-\epsilon_{1,2}\nu^2}}} \ . \tag{B.24h}$$

With these Fresnel equations the effective refraction and transmission coefficients $r^{p,s}$ and $t^{p,s}$ [Hellen and Axelrod, 1987] can now be introduced:

$$r^{p,s} = \frac{r_{1,2}^{p,s} + r_{2,3}^{p,s} \mathrm{e}^{i2k_1 t\sqrt{\epsilon_2/\epsilon_1 - \nu^2}}}{1 + r_{1,2}^{p,s} r_{2,3}^{p,s} \mathrm{e}^{i2k_1 t\sqrt{\epsilon_2/\epsilon_1 - \nu^2}}} \tag{B.25a}$$

$$t^{p,s} = \frac{t_{1,2}^{p,s} t_{2,3}^{p,s} \mathrm{e}^{i2k_1 t\sqrt{\epsilon_2/\epsilon_1 - \nu^2}}}{1 + r_{1,2}^{p,s} r_{2,3}^{p,s} \mathrm{e}^{i2k_1 t\sqrt{\epsilon_2/\epsilon_1 - \nu^2}}} \tag{B.25b}$$

For the analysis of a three layer problem all the equations described for the two layer problem can be used, if the effective refractive and transmission coefficient are used.

C Vesicles

Vesicles are formed through electrostatic forces on lipid molecules in solution. Commercially available lipid molecules (SOPD-Avanti Polar Lipids) in a sucrose solution were put on indium tin oxide coated glass surfaces. The glass plates were put into a capacitor and a voltage of approximately 1 V was applied for 1 hour, during which vesicles spontaneously formed from the lipid molecules.

Bibliography

B. Alberts, A. Johnson, J. Lewis, M. Raff, K. Roberts, and P. Walter. *Molekularbiologie der Zelle*. Wiley-VCH, Weinheim, 2004.

A. S. Andersson, F. Backhed, A. von Euler, A. Richter-Dahlfors, D. Sutherland, and B. Kasemo. Nanoscale features influence epithelial cell morphology and cytokine production. *Biomaterials*, 24(20):3427–3436, 2003.

D. Axelrod. Carbocyanine dye orientation in red cell membrane studied by microscopic fluorescence polarization. *Biophysical Journal*, 26(3):557–573, 1979.

D. Axelrod. Cell-substrate contacts illuminated by total internal reflection fluorescence. *Journal of Cell Biology*, 89(1):141–145, 1981.

D. Axelrod. Total internal reflection fluorescence microscopy in cell biology. *Traffic*, 2 (11):764–774, 2001.

D. Axelrod, D. E. Koppel, J. Schlessinger, E. Elson, and W. W. Webb. Mobility measurement by analysis of fluorescence photobleaching recovery kinetics. *Biophysical Journal*, 16(9):1055–1069, 1976.

P. Bergveld, J. Wiersma, and H. Meertens. Extracellular potential recordings by means of a field-effect transistor without gate metal, called OSFET. *IEEE Transactions on Biomedical Engineering*, 23(2):136–144, 1976.

D. Braun and P. Fromherz. Fluorescence interferometry of neuronal cell adhesion on microstructured silicon. *Physical Review Letters*, 81(23):5241–5244, 1998.

D. Braun and P Fromherz. Imaging neuronal seal resistance on silicon chip using fluorescent voltage-sensitive dye. *Biophysical Journal*, 87(2):1351–1359, 2004.

M. Brittinger and P. Fromherz. Field-effect transistor with recombinant potassium channels: fast and slow response by electrical and chemical interactions. *Applied Physics A-Materials Science and Processing*, 81(3):439–447, 2005.

J. S. Burmeister, G. A. Truskey, and W. M. Reichert. Quantitative analysis of variable-angle total internal reflection fluorescence microscopy (VA-TIRFM) of cell/substrate contacts. *Journal of Microscopy*, 173(Pt 1):39–51, 1994a.

J. S. Burmeister, G. A. Truskey, J. L. Yarbrough, and W. M. Reichert. Imaging of cell/substrate contacts on polymers by total internal reflection fluorescence microscopy. *Biotechnology Progress*, 10(1):26–31, 1994b.

C. S. Chen, J. L. Alonso, E. Ostuni, G. M. Whitesides, and D. E. Ingber. Cell shape provides global control of focal adhesion assembly. *Biochemical and Biophysical Research Communications*, 307(2):355–361, 2003.

W. T. Chen and S. J. Singer. Immunoelectron microscopic studies of the sites of cell-substratum and cell-cell contacts in cultured fibroblasts. *Journal of Cell Biology*, 95 (1):205–222, 1982.

F. de Fornel. *Evanescent waves: from newtonian optics to atomic optics*. Springer, Berlin, Heidelberg, New York, 2001.

M. J. Farabee. On-line biology book. URL `http://www.estrellamountain.edu/faculty/farabee/biobk/biobooktoc.html`. 21.07.2007.

G. W. Ford and W. H. Weber. Electromagnetic-interactions of molecules with metal-surfaces. *Physics Reports-Review Sectiono of Physics Letters*, 113(4):195–287, 1984.

S. Frings, N. Brüll, C. Dzeja, A. Angele, V. Hagen, U. B. Kaupp, and A. Baumann. Characterization of ether-à-go-go channels present in photoreceptors reveals similarity to IKx, a K+ current in rod inner segments. *Journal of General Physiology*, 111 (4):583–599, 1998.

P. Fromherz, A. Offenhausser, T. Vetter, and J. Weis. A neuron-silicon junction: a retzius cell of the leech on an insulated-gate field-effect transistor. *Science*, 252(5010): 1290–1293, 1991.

P. Geggier and G. Fuhr. A time-resolved total internal reflection aqueous fluorescence (TIRAF) microscope for the investigation of cell adhesion dynamics. *Applied Physics A-Materials Science and Processing*, 68(5):505–513, 1999.

D. Gingell, O. S. Heavens, and J. S. Mellor. General electromagnetic theory of total internal reflection fluorescence: the quantitative basis for mapping cell-substratum topography. *Journal of Cell Science*, 87 (Pt 5):677–693, 1987.

F. L. Graham, J. Smiley, W. C. Russell, and R. Nairn. Characteristics of a human cell line transformed by dna from human adenovirus type 5. *Journal of General Virology*, 36(1):59–74, 1977.

G. W. Gross, W. Y. Wen, and J. W. Lin. Transparent indium tin oxide electrode patterns for extracellular, multisite recording in neuronal cultures. *Journal of Neuroscience Methods*, 15(3):243–252, 1985.

L. Guemouri, J. Ogier, and J. J. Ramsden. Optical properties of protein monolayers during assembly. *Journal of Chemical Physics*, 109(8):3265–3268, 1998.

O. P. Hamill, A. Marty, E. Neher, B. Sakmann, and F. J. Sigworth. Improved patch-clamp techniques for high-resolution current recording from cells and cell-free membrane patches. *European Journal of Physiology*, 391(2):85–100, 1981.

S. Hell and E. H. K. Stelzer. Fundamental improvement of resolution with a 4pi-confocal fluorescence microscope using 2-photon excitation. *Optics Communications*, 93(5-6): 277–282, 1992.

S. W. Hell and J. Wichmann. Breaking the diffraction resolution limit by stimulated-emission-depletion fluorescence microscopy. *Optics Letters*, 19(11):780–782, 1994.

H. E. Hellen and D. Axelrod. Fluorescence emission at dielectric and metal-film interfaces. *Journal of the Optical Society of America B-Optical Physics*, 4:337–350, 1987.

M. Höller. Biophysikalische Charakterisierung des Zell-Transistor-Kontaktes. Diplomarbeit, Rheinisch-Westfälische Technische Hochschule Aachen, 2005.

R. O. Hynes. Integrins: bidirectional, allosteric signaling machines. *Cell*, 110(6):673–687, 2002.

H Ibach and H Lüth. *Festkörperphysik*. Springer, Berlin, Heidelberg, New York, 2002.

T. Ide and T. Yanagida. An artificial lipid bilayer formed on an agarose-coated glass for simultaneous electrical and optical measurement of single ion channels. *Biochemical and Biophysical Research Communications*, 265(2):595–599, 1999.

S. Ingebrandt. *Charakterisierung der Zell-Transistor Kopplung*. Dissertation, Johannes Gutenberg-Universität Mainz, May 2001.

D. J. Irvine, Hue K. A., A. M. Mayes, and L. G. Griffith. Simulations of cell-surface integrin binding to nanoscale-clustered adhesion ligands. *Biophysical Journal*, 82(1 Pt 1):120–132, 2002.

Y. Iwanaga. *Cell-substrate distance measurement in correlation with distribution of adhesion molecules by fluorescence microscopy*. Dissertation, Technische Universität München, 2000.

Y. Iwanaga, D. Braun, and P. Fromherz. No correlation of focal contacts and close adhesion by comparing GFP-vinculin and fluorescence interference of DiI. *European Biophysics Journal with Biophysics Letters*, 30(1):17–26, 2001.

J. Jahanmir, B. G. Haggar, and J. B. Hayes. The scanning probe microscope. *Scanning Microscopy*, 6(3):625–660, 1992.

Y. Jimbo, H. P. C. Robinson, and A. Kawana. Simultaneous measurement of intracellular calcium and electrical-activity from patterned neural networks in culture. *IEEE Transactions on Biomedical Engineering*, 40(8):804–810, 1993.

A. Lambacher and P. Fromherz. Fluorescence interference-contrast microscopy on oxidized silicon using a monomolecular dye layer. *Applied Physics A-Materials Science and Processing*, 63(3):207–216, 1996.

A. Lambacher and P. Fromherz. Luminescence of dye molecules on oxidized silicon and fluorescence interference contrast microscopy of biomembranes. *Journal of the Optical Society of America B-Optical Physics*, 19(6):1435–1453, 2002.

D. Lauffenberger and J. Linderman. *Receptors*. Oxford University Press, Oxford, 1993.

F. Linke. *Development of Ellipsometric microscopy as a quantitative High-Resolution Technique for the Investigation of Thin Films at Glass-Water and Silicon-Air Interfaces*. Dissertation, Technische Universität München, 2004.

Z. W. Liu, S. Durant, H. Lee, Y. Pikus, N. Fang, Y. Xiong, C. Sun, and X. Zhang. Far-field optical superlens. *Nano Letters*, 7(2):403–408, 2007.

D. Loerke. *Molecular dynamics of clathrin proteins at endocytic sites studied with evanescent-wave microscopy*. Dissertation, Georg-August-Universität zu Göttingen, 2004.

D. Loerke, B. Preitz, W. Stühmer, and M. Oheim. Super-resolution measurements with evanescent-wave fluorescence excitation using variable beam incidence. *Journal of Biomedical Optics*, 5(1):23–30, 2000.

D. Loerke, W. Stühmer, and M. Oheim. Quantifying axial secretory-granule motion with variable-angle evanescent-field excitation. *Journal of Neuroscience Methods*, 119(1):65–73, 2002.

A. B. Matsko and V. S. Ilchenko. Optical resonators with whispering-gallery modes -

part i: Basics. *IEEE Journal of Selected Topics in Quantum Electronics*, 12(1):3–14, 2006.

A. L. Mattheyses and D. Axelrod. Direct measurement of the evanescent field profile produced by objective-based total internal reflection fluorescence. *Journal of Biomedical Optics*, 11(1):014006, 2006.

A. L. Mattheyses, K. Shaw, and D. Axelrod. Effective elimination of laser interference fringing in fluorescence microscopy by spinning azimuthal incidence angle. *Microscopy Research and Technique*, 69(8):642–647, 2006.

S. Meyburg. *Transistor Arrays for the Direct Interfacing with Electrogenic Cells*. Dissertation, Rheinisch-Westfälische Technische Hochschule Aachen, 2005.

K. E. Michael. *FAK modulates cell adhesion strengthening via two distinct mechanisms: integrin binding and vinculin localization*. PhD thesis, Georgia Institute of Technology, 2006.

D.B. Murphy. *Fundamentals of Light Microscopy and Electronic Imaging*. Wiley-Liss, New York, 2001.

E. Neher and B. Sakmann. Single-channel currents recorded from membrane of denervated frog muscle fibres. *Nature*, 260(5554):799–802, 1976.

Nikon. MicroscopyU. URL `www.microscopyu.com`. 01.08.2007.

H. Nyquist. Certain topics in telegraph transmission theory. *Transactions of the American Institute of Electrical Engineers*, 47(2):617–644, 1928.

A. Offenhäusser, J. Ruhe, and W. Knoll. Neuronal cells cultured on modified microelectronic device surfaces. *Journal Of Vacuum Science and Technology A-Vacuum Surfaces And Films*, 13(5):2606–2612, 1995.

B. P. Olveczky, N. Periasamy, and A. S. Verkman. Mapping fluorophore distributions in three dimensions by quantitative multiple angle-total internal reflection fluorescence microscopy. *Biophysical Journal*, 73(5):2836–2847, 1997.

J. J. Pancrazio, P. P. Bey, A. Loloee, S. R. Manne, H. C. Chao, L. L. Howard, W. M. Gosney, D. A. Borkholder, G. T. A. Kovacs, P. Manos, D. S. Cuttino, and D. A. Stenger. Description and demonstration of a CMOS amplifier-based-system with measurement and stimulation capability for bioelectrical signal transduction. *Biosensors and Bioelectronics*, 13(9):971–979, 1998.

J. Pine. Recording action-potentials from cultured neurons with extracellular microcircuit electrodes. *Journal of Neuroscience Methods*, 2(1):19–31, 1980.

J. Radler and E. Sackmann. Imaging optical thicknesses and separation distances of phospholipid-vesicles at solid-surfaces. *Journal De Physique II*, 3(5):727–748, 1993.

A. Rauf. Analysis of cell morphology in dependence of selected surface coatings by means of confocal laser scanning microscopy. Master's thesis, Fachhochschule Aachen, 2007.

W. G. Regehr, J. Pine, C. S. Cohan, M. D. Mischke, and D. W. Tank. Sealing cultured invertebrate neurons to embedded dish electrodes facilitates long-term stimulation and recording. *Journal of Neuroscience Methods*, 30(2):91–106, 1989.

W. M. Reichert and G. A. Truskey. Total internal reflection fluorescence (TIRF) microscopy. I. Modelling cell contact region fluorescence. *Journal of Cell Science*, 96 (Pt 2):219–230, 1990.

E Sackmann and R. F. Bruinsma. Cell adhesion as wetting transition? *ChemPhysChem*, 3(3):262–269, 2002.

E. Sackmann and S. Goennenwein. Cell adhesion as dynamic interplay of lock-and-key, generic and elastic forces. *Progress of Theoretical Physics Supplement*, 1(165):78–99, 2006.

R. Schönherr, L. M. Mannuzzu, E. Y. Isacoff, and S. H. Heinemann. Conformational switch between slow and fast gating modes: allosteric regulation of voltage sensor mobility in the EAG K+ channel. *Neuron*, 35(5):935–949, 2002.

O. Shimomura, F. H. Johnson, and Y. Saiga. Extraction, purification and properties of aequorin, a bioluminescent protein from luminous hydromedusan, aequorea. *Journal of Cellular and Comparative Physiology*, 59(3):223–231, 1962.

I. I. Smolyaninov, Y. J. Hung, and C. C. Davis. Magnifying superlens in the visible frequency range. *Science*, 315(5819):1699–1701, 2007.

A. Stett, W. Barth, S. Weiss, H. Haemmerle, and E. Zrenner. Electrical multisite stimulation of the isolated chicken retina. *Vision Research*, 40(13):1785–1795, 2000.

A. L. Stout and D. Axelrod. Evanescent field excitation of fluorescence by epi-illumination microscopy. *Applied Optics*, 28(24):5237–5242, 1989.

C. A. Thomas, P. A. Springer, L. M. Okun, Berwaldn.Y, and G. E. Loeb. Miniature microelectrode array to monitor bioelectric activity of cultured cells. *Experimental Cell Research*, 74(1):61–67, 1972.

G. A. Truskey, J. S. Burmeister, E. Grapa, and W. M. Reichert. Total internal reflection fluorescence microscopy (TIRFM). ii. Topographical mapping of relative cell/substratum separation distances. *Journal of Cell Science*, 103 (Pt 2):491–499, 1992.

J. Voros. The density and refractive index of adsorbing protein layers. *Biophysical Journal*, 87(1):553–561, 2004.

A. Wachter and H. Hoeber. *Repetitorium Theoretische Physik*. Springer, Berlin, Heidelberg, New York, 1998.

J. E. Weinstein, J. T. Oris, and D. H. Taylor. An ultrastructural examination of the mode of uv-induced toxic action of fluoranthene in the fathead minnow, pimephales promelas. *Aquatic Toxicology*, 39(1):1–22, July 1997.

R. Weis, B. Muller, and P. Fromherz. Neuron adhesion on a silicon chip probed by an array of field-effect transistors. *Physical Review Letters*, 76(2):327–330, 1996.

G. Wrobel, M. Höller, S. Ingebrandt, S. Dieluweit, F. Sommerhage, H. P. Bochem, and A. Offenhäusser. Transmission electron microscopy study of the cell-sensor interface. *Journal of the Royal Society Interface*, to be published, Jul 2007. doi: 10.1098/rsif.2007.1094.

E. Zamir. Molecular complexity and dynamics of cell-matrix adhesions. *Journal of Cell Science*, 114(20):3583–3590, 2001.

G. Zeck and P. Fromherz. Repulsion and attraction by extracellular matrix protein in cell adhesion studied with nerve cells and lipid vesicles on silicon chips. *Langmuir*, 19(5):1580–1585, 2003.

ZEISS. Carl Zeiss MicroImaging. URL `http://www.zeiss.de/mikro`. 25.07.2007.

Danke. . .

An dieser Stelle möchte ich mich bei all denen Bedanken, die mich auf den Höhen und Tiefen dieser Diplomarbeit begleitet haben. . .

Danke Herr Prof. Dr. Andreas Offenhäusser, für das Ermöglichen dieser Diplomarbeit und die Aufnahme in Ihr tolles, interdisziplinäres Institut.

Danke Herr Prof. Dr. Gero von Plessen, für die Bereitschaft Zweitgutachter dieser Arbeit zu sein.

Danke Dr. Sven Ingebrandt, für die gute Betreuung und für deine immer offene Tür für die "Frage zwischendurch".

Danke Stefan Eick, für die viele Zeit in der du mit deiner ruhigen, gründlichen Art Probleme mit mir besprochen hast, und mich in schwierigen Zeiten wieder aufgebaut hast.

Danke Boris Hofmann, weil auf dich in fachlichen und privaten Dingen immer Verlaß war.

Danke Dr. Kristin Michael, my institute "roommate". You gave me moral support, perspective and introduced me to cell adhesion.

Danke Rita Helpenstein, Esther Breuer, Sabrina Buller und Torsten Wilms für Rat und Tat in allen Aspekten der Zellkultur, sowie eurer grenzenlosen Geduld gegenüber einem Physiker im Biolabor. Insbesondere danke ich dir Rita, für die Neuronenkultur und dir Esther für die Hilfe mit den Proteinbeschichtungen als es gegen Ende eng wurde.

Danke Anna Reska, für die Präparation sowie der Kultur der Grillenneuronen.

Danke Christoph Möhl (IBN-4), für die Transfizierung der HEK293 mit GFP gekoppeltem Vinkulin.

Danke Agnes Csiszar (IBN-4), für die Herstellung der Lipidvesikel.

Danke Mathias Schindler, du hast mir immer wieder wertvolle Tips gegeben.

Danke Frank Sommerhage, für deine Hilfe bei meinen ersten Schritten in MATLAB.

Danke Dr. Michael Pabst, für Ihre Hilfe in Fragen der Mathematik und die langen Diskussionen zur Nahfeldphysik.

Danke Dr. Bodo Borm (ZEISS), für viel Zeit und Mühe in allen Fragen der Mikroskopie.

Danke Susanne Schäfer, meine Mit–Diplomandin, für unterhaltsame Pausen und viele Gespräche.

Danke Dr. Petra Schulte, für die viele Zeit, die du dir bei der Beantwortung vieler meiner Fragen genommen hast.

Danke Herr Prof. Dr. R. Merkel, für die wertvollen Tips und die Zeit, die Sie sich immer genommen haben, wenn ich mich mit einer Frage an Sie gewendet habe.

Danke Dr. Günter Wrobel, für deine Hilfe in der leider kurzen Zeit in der du noch am Institut warst.

Danke Dr. Simone Meffert, für deine Hilfe in Fragen der Biologie.

Danke allen anderen Kollegen des IBN-2, die hier nicht namentlich erwähnt wurden.

Danke meiner Familie, die mich während meines Studiums unterstützt hat.

Danke meiner Verlobten Agnes. Du hast mir Kraft gegeben, wenn ich sie brauchte und hattest besonders in der Endphase dieser Arbeit viel Geduld mit mir.

Danke meinem Sohn Ferdinand. Du hast mich immer mit einem Lachen und manchmal einem Tränchen begrüßt, wenn ich nach Hause kam. So hast du mich selbst streßigste Momente vergessen lassen.

Forschungszentrum Jülich
in der Helmholtz-Gemeinschaft

Jül-4255
September 2007
ISSN 0944-2952